CHARGE TRANSPORT AND PHOTOCONDUCTIVITY IN THE LEAD DI-IODIDE LAYER STRUCTURE.

A thesis submitted to the
University of Leicester

by

Thomas Dark, B.Sc.

for the degree of Doctor of Philosophy
in the Faculty of Science,
1969.

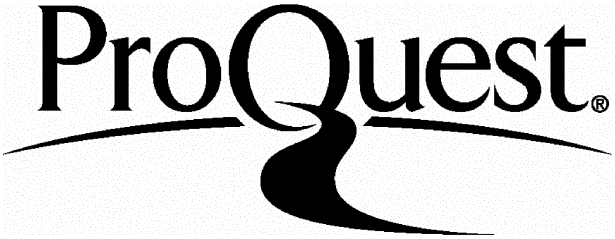

CONTENTS

Abstract.

This thesis presents the results of an investigation into the hole mobility and its temperature dependence in single crystal specimens of the layer compound PbI_2 in a direction parallel to the c-axis. Thin specimens, between 20 and 70 μms thick, were cleaved from a larger boule crystal and fitted with evaporated metal electrodes. The temperature dependence of the electrical conductivity along this axis has also been studied, as well as the photoconductive response at 290°K.

The hole drift mobility was investigated by the use of fast electron beam techniques. A 30keV excitation pulse of 10nsec duration was focussed on to the specimen and generated free carriers near the top electrode. A measurement of the transit time in a pulsed applied field led to a value for the hole drift mobility μ.

At room temperature μ was found to lie between 1.8 and 5$cm^2 volt^{-1} sec^{-1}$. For most specimens the temperature dependence of mobility above about 250°K can be represented by an equation of the form $\mu \propto \exp \epsilon/kT$, where ϵ represents an energy that varies between 0.025 to 0.150eV for the crystals investigated. At a particular temperature, it is found that the low mobility specimens

correspond to the highest values of ϵ . On the basis of the results it is concluded that the hole transport takes place in a narrow band and that the mobility is determined by optical mode scattering. At temperatures below 250°K, however, specimens with high ϵ show the presence of another transport mechanism in which μ becomes essentially temperature independent.

Attempts have been made to fit the mobility results to two transport theories: Holstein's small polaron theory and the model developed by Fivaz and Mooser for transport in layer structures. Possible reasons for the range of observed optical phonon energies are discussed.

Measurements of the temperature dependence of the dark conductivity revealed a trapping level 0.55eV below the bottom of the conduction band, which hitherto had not been detected. In addition a defect trapping level 0.26eV above the valence band was found in agreement with previous workers. At temperatures greater than 400°K to 450°K, the electrical properties are determined by an ionic conduction mechanism with an activation energy of 1.3eV. This appears to be connected with the creation and movement of Pb^{2+} interstitials.

The room temperature photoconductive response shows the absorption edge to be located at about 2.4eV. On the basis of the present results and

those of other workers, an energy level scheme for PbI_2 is proposed which can account for the majority of the observed features.

ACKNOWLEDGEMENTS

The author would like to thank Professor E.A. Stewardsom for the opportunity to work in his department. He is greatly indebted to Professor W.E. Spear for initially suggesting the problem and also for the generous help and guidance given throughout the investigation.

Finally, the author wishes to express his gratitude to his wife for the willing assistance she has given throughout the preparation of this thesis.

The financial support of the S.R.C. is also gratefully acknowledged.

CHAPTER 1

Introduction.

The intentions at the outset of the present investigation were to compare and contrast the charge transport in a number of layer compounds in a direction perpendicular to the layers. To this end, Cadmium Iodide, Lead Di-iodide, a mixed crystal of Cadmium Lead Iodide and three types of Gallium Selenide samples (transport reacted, vapour phase and melt grown) have been investigated. All crystals, with the exception of PbI_2, showed such limited lifetime signals that drift mobility measurements were not possible. In fact, of the two PbI_2 boules available, only one was useful for such measurements and eventually even platelets cleaved from this boule showed only lifetime limited hole transits. Consequently, it was not possible to pursue this particular aspect of the investigation as far as it had originally been hoped.

This thesis will present the charge transport results, together with dark conductivity measurements as a function of temperature and the photoconductive response at room temperature. However, these results will be preceeded by a number of chapters which are intended to familiarize the reader with the PbI_2 structure and the known properties of layer compounds and also to provide a basis for the

interpretation of the results.

Chapter 2 will deal with the structure of the layer compounds, that of PbI_2 being given in greater detail together with the methods by which PbI_2 may be prepared. The properties of the gallium monochalcogenides i.e. GaS, GaSe and GaTe, will be described in the opening sections of Chapter 3. This has been included because these are the layer compounds which have received most experimental and theoretical attention. The remainder of that chapter will be devoted to PbI_2.

Chapter 4 will give, in qualitative fashion, the theories which would be expected to describe charge transport in a layer compound perpendicular to the layers, and for the most part will be occupied with the small polaron theory due to Holstein. The experimental apparatus and procedure is described in Chapter 5, whilst the following chapter will present the experimental results. These will be discussed and interpreted in the final chapter and on this basis an amended energy level diagram (at k=0) will be suggested.

CHAPTER 2

General Properties and the Preparation of Layer Compounds.

Introduction.

There appear to be no review articles concerned solely with layer compounds. Because one such compound is the subject of the present investigation, it would seem desirable to present in this chapter a brief survey of the properties of these materials and of important work in this field. The gallium monochalcogenides (i.e. GaSe, GaS and GaTe) together with PbI_2 will then be treated more fully in Chapter 3.

2.1 The Structure of Layer Compounds.

Many types of layer compound have been described in the literature. Their common feature is the van der Waals forces which bind the layers together, although this is sometimes reinforced by a small ionic contribution.

The prototype of all layer structures is graphite, consisting of sheets of carbon atoms. The atoms within each sheet are held together by covalent bonds; the same applies to boron nitride, a layer compound closely resembling the graphite structure. The layer structure of Bi_2Te_3 is shared by Bi_2Te_2S, Bi_2Se_3, Bi_2Te_2Se and Sb_2Te_3.

The structure of Bi_2Te_2S, for example, is best visualised as a series of atomic layers along the c-axis following one another in the succession characteristic of cubic close-packing. The order is: S-Bi-Te-Te-Bi-S-Bi-Te-Te-Bi-.

MoS_2 and WSe_2 are examples of hexagonal layer compounds with elongated bimolecular units. In MoS_2, for example, the S-S distance between double layers, 3.66Å, is approximately the radial sum for ionic sulphur, in contrast to the other S-S separations, which are much less than this. The unusual compound calcium monochloride, CaCl, is tetragonal and composed of double Ca layers alternating with double layers of Cl. Another layered tetragonal structure is lead fluorochloride, PbFCl, the structure of which is shared by about fifty other substances.

The simplest and most familiar of all layer structures, excepting graphite, is the original CdI_2 or $Cd(OH)_2$ grouping, with the C6 structure. It is hexagonal with a single molecule per unit cell. A typical atomic arrangement, in the case of CdI_2, consists of layers of Cd- or I- atoms perpendicular to the c-axis. The sequence is illustrated in fig. 2.1. At least seventy representatives of this structure have been identified, and include di-chalcogenides, di-halides, some hydroxides and halo-hydroxides of many metals. Lead di-iodide, PbI_2, is one of the crystals showing this arrangement.

In the typical example of CdI_2, the Cd-I and I-I separations are about equal to the sums of the ionic radii. Thus, it is permissible to view the structure as a hexagonal close-packing of iodine ions with the smaller cadmium ions nesting between alternate layers of iodine. In some crystals with this stucture, however, the anion-anion separations are not all alike and some are greater than the sums of the ionic radii.

Both PbI_2 and CdI_2 have been shown to be polytypic i.e. the basic anion and cation layers may differ in the way they are repeated along the c-axis. More than forty polytypes of CdI_2 have so far been identified, whilst at least four polytypes of PbI_2 are known. The simplest form of PbI_2, the C6 structure, has a monomolecular unit of dimensions, a_0=4.557Å and c_0=6.979Å, whilst the polytypes have the same value of a_0 but simple integer values of c_0.

Another class of layer compounds is formed by the gallium and indium monochalcogenides, with the exception of InTe. The atomic arrangement within each layer for the gallium monochalcogenides is the same, and is shown in fig. 2.2. It is seen to consist of four sub-layers, containing two close-packed gallium layers and two close-packed anion layers in the sequence anion-gallium-gallium-anion. Within each of these multiple layers, the

atoms are covalently bonded, so that each cation is tetrahedrally surrounded by three anions and one other cation. The arrangement of the layers in respect of one another varies between compounds, but in each one, the bonding between adjacent, multiple layers is of the van der Waals type with possibly a small ionic contribution. GaSe and GaS crystals show extremely easy cleavage characteristics along the layers. This is a consequence of the nature of the bonds and also of the large separation between the layers, which is similar in magnitude to the thickness of a layer. However, the layer separations in GaTe have been shown to be much smaller. In conclusion, GaSe, like CdI_2 and PbI_2 also exists in polytypes.

2.2 General properties of Layer Compounds.

Hulliger (1960) has concluded from theoretical bonding arguments that those layer compounds having the CdI_2 structure may occur as insulators, semiconductors, semimetallic compounds and even superconductors. Experimental evidence has indeed accumulated in support. SnS_2 and CdI_2 itself have been demonstrated to be semi-insulating (Greenaway and Nitsche, 1965), ZrS_2 and $HfSe_2$ to be typical semiconductors (McTaggart, 1958); Greenaway and Nitsche (1965) concluded that $TiTe_2$ is probably a semimetal and Dudkin and Vaidanich (1961) suggested that it had metallic

properties.

Exciton effects have been observed in the partially ionic compounds PbI_2 and CdI_2. The latter is more ionic and gives rise to two pronounced exciton peaks, separated by an antiresonance, at photon energies above the fundamental absorption edge (Greenaway and Nitsche, 1965). The existence of this pronounced excitonic structure deep in the fundamental absorption region can be explained qualitatively in terms of the lower dielectric constant and the correspondingly increased Coulomb interaction in ionic crystals. PbI_2 has been demonstrated by many workers to give rise to exciton effects at photon energies both below and above the absorption edge. The excitons observed at energies above the edge are, as with CdI_2, due to transitions to parabolic, metastable exciton states, degenerate with a quasi-continuum of band states. It will be seen in the next chapter that there is much uncertainty about the nature of the exciton at photon energies below the fundamental edge.

The covalent IV-VI_2 chalcogenides do not give rise to excitonic effects. From a thorough investigation and correlation of their reflectivity spectra, Greenaway and Nitsche (1965) were convinced that interactions perpendicular to the layers are important in determining the band structure. A similar conclusion has been reached by

Greenaway and Harbeke (1965) for the layer structure of bismuth telluride, and also by Brebner and Mooser (1967) for GaSe polytypes.

The optical and electrical properties of GaSe, GaS and GaTe have been the subject of much research. GaS has been found to be an indirect band gap material of $E_g \simeq 2.5$eV but GaSe has a direct gap of about 2.0eV. They are all good photoconductors. This, together with other optical and electrical properties, will be discussed in the following chapter.

2.3 Methods of Preparation of Layer Compounds.

Layer compounds in single crystal form have been prepared using some of the techniques applied generally to single crystal growth. These will, for the most part, be mentioned in this section, whilst chemical transport reactions will be dealt with in more detail. This method has been found to be extremely valuable for many layer compounds.

Single crystal platelets of both PbI_2 and CdI_2 crystallize from saturated aqueous solutions. Whereas CdI_2 crystals up to 500μms. in thickness may be obtained, the PbI_2 crystals rarely exceed a few microns. Much thicker single crystals of PbI_2 can be grown from a melt of zone-refined material by the Bridgman method. This technique,

however, is liable to involve large constraining forces and leads to a high concentration of defects. These forces may be eliminated by the use of a new method of crystal growth in silica gel (Henisch, Dennis and Hanoka, 1965), for the latter yields mechanically to the growing crystal. PbI_2 crystals of relatively high purity and a high degree of perfection have been prepared by this technique, (Dennis and Henisch, 1967).

The gallium monochalcogenides and group IV-VI_2 chalcogenides have both been grown from the melt and also by simple sublimation or by vapour transport. They may also be prepared under less extreme conditions by means of chemical transport. This technique was introduced by Schaefer (1962), and has proved a very useful method for growing crystals from the vapour phase.

Chemical transport reactions are based on the fact that a transport of matter can occur in a chemical system consisting of one solid and n gaseous components in equilibrium, if the equilibrium constant is made to vary locally. This can be achieved by imposing a temperature gradient along the vessel containing the system. The simplest arrangement is a closed tube with a polycrystalline solid, (e.g. $SnSe_2$), at a temperature T_1 at one end (Zone 1), and T_2 at the other end (Zone 2). In the absence of any other component in the tube, the system reduces to n=1. At high

enough temperatures and $T_1 > T_2$, normal sublimation of $SnSe_2$ will occur.

If, however, a substance such as iodine, which forms a volatile compound with $SnSe_2$, is introduced, an equilibrium will be established:

$$SnSe_2 + I_2 \rightleftharpoons SnI_2 + 2Se.$$

Deposition of $SnSe_2$ in Zone 2 will occur because of the different equilibrium conditions in the two halves of the tube. Single crystals can only be obtained by adjusting the experimental parameters in such a manner that, once a certain number of seeds are formed in Zone 2, the amount of material arriving in this zone per second corresponds to the velocity of growth of the seeds.

CHAPTER 3

A Survey of Previous Work.

3.1 Introduction.

In this chapter, a brief review will first be given of the optical and electrical properties of the gallium monochalcogenides. Of all the layer compounds, these have been the subject of the most thorough experimental and theoretical investigations. A more detailed survey of the properties of PbI_2 will follow and will include decomposition, conductivity and optical studies. The latter has provided valuable information on the band structure and led to interesting excitonic effects both at the fundamental absorption edge and at higher energies. These effects will be compared and contrasted with similar ones observed in CdI_2. No electrical transport data for PbI_2 could be found in the literature, so that the work described in the following chapters of this thesis provides the only information on this aspect.

3.2.1 Electrical Transport in the Gallium Monochalcogenides.

It must first be noted that the work in this section refers to electrical conduction perpendicular to the c-axis. There is no information available in the literature concerned with transport along this axis.

Fischer and Brebner (1962a) have investigated resistivity and Hall coefficients for single crystal samples of GaTe and GaSe. The p-type materials yielded hole mobilities of 40 $cm^2volt^{-1}sec^{-1}$ and 30 $cm^2volt^{-1}sec^{-1}$ respectively at 20°C and a temperature dependence of $T^{-1.8}$ and $T^{-1.6}$ (fig. 3.1). Electron mobilities of similar magnitude and temperature dependence were reported earlier by Fielding, Fischer and Mooser for GaTe (1959). These latter galvanomagnetic measurements indicated an intrinsic region above 600°K, with an activation energy corresponding to the band gap of 1.65eV.

The work of Fischer and Brebner (1962a) further revealed that cold-worked GaTe crystals showed an increase in both resistivity and Hall coefficient as large as 30%. To account for this, they proposed a model in which the dislocations introduced by mechanical working were associated with dangling bonds, which correspond to energy states close to the conduction and valence bands.

More recently, Fivaz and Mooser (1964) have carried out further hole mobility measurements on GaSe. Their results, shown in fig. 3.2, led to mobility values an order of magnitude greater than those previously reported by Fischer and Brebner. This has been ascribed to the superior quality of transport reacted samples as compared with crystals grown from the melt. However, they

also found a very strong temperature dependence, $\mu \sim T^{-2.2}$. This was interpreted in terms of a proposed new electron-phonon interaction characteristic of layer compounds, and is described in more detail in Chapter 4. It can account for the rapid decrease of mobility with increasing temperature and is supported by the fact that the results yield a vibrational energy ($\hbar\omega$) between 50 and 100meV. This is consistent with the values deduced from force constants normally met in covalent crystals.

3.2.2 Optical Properties of the Gallium Monochalcogenides.

The optical absorption edge of GaTe was studied by Brebner, Fischer and Mooser (1962) and determined to lie at 1.78 eV (40°K) and 1.65eV (300°K). This is in close agreement with similar observations reported earlier by Fielding, Fischer and Mooser (1959), and also with the photoconductive response measurements of Ryvkin and Khansevarow (1956). In addition, Brebner et al observed a pronounced line structure near the absorption edge, strongly temperature dependent, the strength of which could be increased by subjecting samples to mechanical work (c.f. Fischer and Brebner, 1962a) and decreased by annealing. These observations led to the conclusion that the structure was not of an excitonic nature, but rather associated with the degree of crystalline imperfection of the samples.

Bassani, Greenaway and Fischer (1964) have extended earlier absorption measurements on GaSe and GaS, notably those of Brebner and Fischer (1962b), to shorter wavelengths. The absorption curves, shown in figs. 3.3a and b, bear a marked similarity, and both materials show the presence of excitons at energies just below the band edge. They are interpreted in terms of current exciton theory and their binding energy has been determined from a formula derived by Elliott (1957). The first two lines reported in GaSe give a binding energy of 0.037eV and a band gap of 2.139eV at 77°K. At energies greater than the fundamental edge both GaSe and GaS are characterised by three main reflectivity peaks, the corresponding transitions in GaS occuring at higher energies. It is interesting to note that, whereas the lowest energy peak of each material was attributed to the same transition, the optical work of Gasanova, Akhondov and Nizametdinova (1966) on GaS_xSe_{1-x} single crystals indicated that the corresponding middle peaks were caused by different transitions.

It has been previously mentioned (Chapter 2) that interactions in the c-direction play a rcle in determining the band structure. Evidence for this in GaSe has been furnished by Brebner and Mooser (1967) by comparing the exciton series in polytypes of this compound. They recorded that the series, and hence the band gap,

was displaced to higher energies by up to 0.049eV in different GaSe modifications. This was due to adjacent layer arrangements being different, so as to lead to an alignment of cations and anions such that an ionic contribution resulted to the weak interlayer bonding. The exciton series itself does not fit the idealized, two-dimensional, hydrogenic series investigated by Ralph (1965). Furthermore, Brebner concluded that the exciton in its ground state extends over about five layer packets in the c-direction (i.e. about 40Å), even though the hole mass in this direction is extraordinarily large (Kamimira and Nakao, 1966).

3.2.3 Band Structure Calculations for GaSe and GaS.

Calculations, of a limited nature, have been attempted by Fischer (1963) on the basis of a two-dimensional free electron model and also by Bassani, Greenaway and Fischer (1964) using the tight binding approach. Both failed to give any real picture of the valence and conduction bands. The best computation to date is that performed by Bassani and Pastori (1967). They have utilised a semi-empirical approach to the tight binding method in the two-dimensional approximation, thus neglecting interactions between layers. This model has been justified by Kamimura and Nakao (1966), who proved with a three-dimensional

calculation in the tight binding approximation that the effective masses in the K_z direction are extremely large. The results of Bassani and Pastori are reproduced in figs. 3.4a and b. It is seen that GaSe has a direct optical gap $\Gamma_1^+ - \Gamma_3^+$,but GaS an indirect one,the transition concerned being from the $\Gamma_1^+ - P_1^+$ states. It is stressed that these differences are mainly due to different lattice parameters,and the atomic value of the p-valence state of Se being shifted to higher energy values with respect to that of S. The band structure of Bassani and Pastori successfully explains many of the experimentally observed optical properties.

3.3.1 The Decomposition of PbI_2 Induced by Electron Bombardment.

The alkali halides,metallic dihalides and hydroxides form a group of materials that can be structurally altered when bombarded with radiation that is not sufficiently energetic to cause direct atomic collision displacement. Forty (1960), wishing to gain more insight into the processes occuring,studied the structural changes and chemical decomposition in very thin platelets of PbI_2 under the beam of an electron microscope. He observed an initial rearrangement of dislocations and formation of new isolated loops,followed by the appearance of mobile

cavities. It was these that provided the sites for the precipitation of lead, the final stage in the decomposition.

A mechanism to account for these observations was later proposed by Forty (1961). It can be conveniently summarised by the following equations:

(i) $I^- \xrightarrow[\text{incident electron}]{\text{ionisation by}} I + e$

(I^- = iodide ion in lattice)

(ii) $I \xrightarrow[\text{thermal energy}]{\text{recoil or}} I \text{ interstitial} + I^- \text{ vacancy}$

(iii) $Pb^{2+} \xrightarrow[\text{from } I^- \text{ vacancy}]{\text{repulsive force}} Pb^{2+} \text{ interstitial} + Pb^{2+} \text{ vacancy}$

(iv) $Pb^{2+} + 2e \longrightarrow Pb$

3.3.2 Conductivity in PbI_2 along the Layers.

The photoconductivity in thin single platelets of PbI_2, perpendicular to the c-axis, has been measured by Forty and Dawood (1962). It was shown to consist of three separate regions between room temperature and 300°C (fig. 3.5). Up to about 180°C the measurements revealed a photoconductive region of activation energy 0.23eV, which was interpreted in terms of the release of charge carriers from traps. However, at 180°C, the conductivity abruptly decreased over a range of 40°C (see section 3.3.3). Thereafter, it rose again to show predominantly

ionic conductivity, proceeding by two distinct mechanisms. The first region, from 230°C to 275°C, displayed an activation energy of 0.42eV whilst above this temperature an activation energy of 1.3eV was in evidence. Both the latter results are in good agreement with Seith (1929) on compressed powders of PbI_2. These were interpreted by Mott and Gurney (1940) as due to extrinsic and intrinsic ionic conduction respectively, and the present authors place a similar interpretation on their results. From various considerations they conclude that the extrinsic conductivity is due mainly to the movement of anion defects, whilst the intrinsic region is connected predominantly with the creation and movement of Pb^{2+} ions.

Henisch and Srinivasagopalan (1966) have performed photoconductive decay measurements with high background light intensity, and claim that under these conditions recombination was the dominant process. The estimated lifetime in their p-type PbI_2 grown in silica gel was 600μsec. Its field dependence led them to an estimated hole mobility of $1 cm^2 volt^{-1} sec^{-1}$ along the layers. However, in view of the results to be presented in this thesis for hole transport parallel to the c-axis, this would seem to be far too low.

Dark conductivity measurements on gel grown PbI_2 by Dugam and Hemisch (1967a), over the temperature

range 200°K to 400°K, revealed an activation energy of 0.26eV. This was in good agreement with their infra red absorption measurements up to 15μms, for an absorption band was seen at 4.2μms (0.29eV), and attributed to absorbing centres of concentration $5.10^{14}cm^{-3}$. The activation energy of 0.26eV should be compared with that of 0.23eV obtained by Forty and Dawood (1962).

3.3.3 Photodecomposition in PbI_2.

Light was shed on the cause of the anomalous fall in photoconductivity between 180°C and 220°C (see fig. 3.5) observed by Forty and Dawood (section 3.3.2) when they established that it coincided with the precipitation of particles of metallic lead. Both only occur in illuminated specimens and at temperatures exceeding 170°C. The decrease in photoconductivity can then be accounted for by a sudden increase in the rate of trapping of photo-electrons or -holes at ion defects. The critical temperature of around 180°C was presumed to imply that at this temperature defects are formed frequently enough and have sufficient mobility to form stable traps, allowing the aggregation of the lead precipitate.

Further investigation by Dawood, Forty and Tubbs (1965) disclosed more information on the nature of photodecomposition. They showed that decomposition is

only caused by wavelengths that are strongly absorbed in PbI_2. As shown in fig. 3.6a, Tubbs (1964) recorded at 100°K a strong absorption peak at 2.52eV (4930Å) preceding a continuous absorption spectrum, with a further absorption peak at 3.2eV (3750Å). A definite correlation was noticed between these peaks and others observed in the spectral response curves for photoconductivity (fig. 3.6b) and for photodecomposition. Since the absorption peaks correspond to exciton transitions (admittedly, at the time the peak at 3.2eV was interpreted by Tubbs as a band to band transition), it would seem justifiable to assume that excitons play an important role in decomposition. Quantitative measurements by Dawood, Forty and Tubbs revealed that the amount of photodecomposition varied as the square of the intensity, as found by Jacobs and Tompkins (1952) in the metallic azides, and as the square root of the time. This suggests a bimolecular process, and the following model has been suggested by Dawood et al.

Visible light of wavelength smaller than about 5200Å produces mobile excitons, mostly in the surface regions. At higher temperatures, if two such excitons become trapped at the same site, most likely a surface imperfection, it is energetically possible for them to interact. The products of such a reaction would be an iodine molecule, two anion vacancies and two electrons

adjacent to the original vacancies. The precipitation of lead then ensues, either by the aggregation of F-centres (the two electrons are trapped at the iodide ion vacancies produced), or by the trapping of electrons by Pb^{2+} ions. The latter is quite feasible for, after the excitons react, a Pb^{2+} ion is left with only one nearest neighbour I^- ion and can thus readily trap the two electrons to form a lead atom.

Dawood, Forty and Tubbs also demonstrate the practical applications of photodecomposition in the field of image recording photography. Single crystals show rather poor resolution, as the precipitates form preferentially at surface imperfections and reach a considerable size before they scatter light. This is in contrast to evaporated films, which are claimed to have at least as good a resolution as the best photographic emulsions, since the surface imperfections are so numerous and the crystallite size so small.

3.3.4 The Fundamental Absorption Edge of PbI_2.

The absorption spectrum of PbI_2 at room temperature was first measured by Hilsch and Pohl (1928) and then by Fesefeld (1930). Imai (1961), using evaporated films, has performed a similar investigation but over a wider wavelength region and also at low temperatures.

His results, shown in figs. 3.7a and b, agree with the earlier ones on the positioning of the fundamental edge at around 5000Å, although a shoulder was now revealed superimposed upon the edge. This shoulder narrowed into a very prominent peak at low temperatures and was attributed to an exciton transition, but no fine structure was observed.

The temperature dependence of the edge was measured by Imai and the absorption coefficient found to obey Urbach's rule. The fact that this rule holds would appear to support the ionic character claimed by some authors for PbI_2.

The above work was undertaken in an attempt to observe the hydrogenic-like exciton series at the fundamental edge which had earlier been reported by Nikitine (1955), and more recently observed by him with other collaborators on different occasions. The most recent results (Nikitine, Schmitt-Burkel, Biellman and Ringeissen, 1964) show the strong exciton absorption line at 4949Å (77°K) to be resolved into several absorption lines at 4.2°K (see fig. 3.7b for 'Nikitine's Series'). The lines fit a hydrogenic-type formula, except the first one, and Haken (1957) has shown that good agreement would not be expected for n=1. The first line is by far the most intense and thus the series would seem to fit that class of Mott-Wannier, or delocalised, excitons which result from

transitions in which the wave vector k=0.

The difference in the results of Imai and Nikitine, outlined above, is indicative of a much wider disagreement which persisted on the question of the exciton lines observed at the fundamental edge. Many such lines have been reported, but there is little agreement as to their wavelengths, number, half-widths and absorption coefficients. This may be partly accounted for by the fact that, for instance, the peak wavelength is sensitive to small changes in the lattice parameter. However, the work of Forty and Tubbs (1965) would appear to provide a consistent explanation for the many differing results published on the exciton spectra in PbI_2.

This work was performed at 4.2°K and measurements disclosed the absorption peak to depend upon the film thickness, as shown in fig. 3.8. For films of thickness less than 400Å, a single absorption peak was observed at 4905Å. This revealed a shoulder on the short wavelength side for thicker specimens, the strength of which increased with film thickness. Eventually, with a film thickness of about 2500Å, the two peaks were of equal prominence, the second peak being located at 4890Å. An explanation of this effect was forthcoming when electron diffraction results showed thin films to consist of an aggregate of crystallites oriented with their c-axes

normal to the substrate, whilst thicker films also contained crystallites with their c-axes parallel to the substrate. The authors justifiably claim this work to throw open to question the issue of Nikitine's hydrogenic series. The third line, which was not always observed, may be simply structure sensitive, for the present work shows that the exciton spectra of anisotropic crystals are very sensitive to specimen structure and orientation.

The effect of polarisation on the absorption spectrum and photoconductive response, particularly around the edge, has been studied by Dugan and Henisch (1967a) and is closely related to the above work. The peak response in the photoconductivity, for the electric vector of the incident radiation respectively parallel and perpendicular to the c-axis, was located at 5015Å and 5065Å. This corresponds to an energy difference of 0.025eV. The difference in the absorption coefficients at the edge indicated a dichroism of 0.048eV.

3.3.5 Exciton Effects in PbI_2 at Energies above the Fundamental Edge.

Imai, in the work previously referred to (1961), observed two temperature-dependent peaks at energies above the edge, at 3.2eV and 4.5eV (fig. 3.7a). These agree well with the later transmission measurements at

100°K (fig. 3.6a) taken by Tubbs (1964), who also identified a peak at 4.01eV. The factors which suggested to Tubbs that these peaks correspond to excitons were the high absorption coefficient in this region (about 5.10^5 cm^{-1}) and their sharpening at lower temperatures.

Excitonic structure above the fundamental edge in PbI_2, and also in the very similar layer compound CdI_2, has been reported by Greenaway and Nitsche (1965) and then by Brahms (1965). A similarity in the lower energy spectral range of the two compounds was noted by Brahms, from which he concluded that the upper valence bands are probably associated with iodine wave functions and are p-like. However, the energy band shape at the Γ (000) symmetry point would seem to be different in the two compounds, since the exciton occuring at the band edge (2.513eV) in PbI_2 was not present in CdI_2.

A more thorough investigation of metastable excitons in both PbI_2 and CdI_2 has been performed by Greenaway and Harbeke (1966). The reflectivity spectrum of PbI_2 (fig. 3.9a) consists of broad, temperature-independent maxima, corresponding to band-band transitions. Superimposed upon these is a line structure, which sharpens considerably at lower temperatures and for this reason was attributed to exciton effects. Three pronounced lines above the edge were recorded at 3.26eV, 4.45eV, and 5.71eV

(the first two agree with those of Imai and Tubbs) and are interpreted as due to metastable exciton states associated with van Hove critical points.

A most important result of this investigation was that, for PbI_2, the exciton states were only present for the electric vector of the incident radiation parallel to the layers. Fig. 3.9b shows that all states, including that at the edge, disappear for the electric vector parallel to the c-axis. This seems to prove that these excitons are of a two-dimensional nature, with the electron and hole confined to the same layer so that the dipole moment of the exciton is parallel to the electric vector.

The reflectivity of CdI_2 at low temperatures was shown by Greenaway and Harbeke to consist of two very strong peaks, each subject to fine structure. However, the exciton structure was present for both polarisations, and the lines could be fitted to a normal three-dimensional hydrogenic model. It is thus seen that these two compounds, with the same structure and nearly equal atomic distances, have entirely different excitonic properties.

3.3.6 Other Properties.

The photoconductive response of PbI_2 crystals grown from a silica gel has been reported by Dugan and Henisch (1968), and is given in fig. 3.10a. It

reveals features at 1.99, 2.16, 2.41 and 3.06eV. The three lower energy features coincide with peaks in their photoluminescence spectrum, fig. 3.10b, the latter also showing peaks at 2.31eV and 1.85eV. The photoluminescence peaks at 2.16eV and 1.99eV each have two shoulders associated with them, suggesting the existence of 0.03eV optical phonons. These results, together with a defect level at 0.46eV above the top of the valence band and obtained by Dugan and Henisch from an analysis of temperature quenching of the photocurrent, will be used in the following section to build a plausible band structure for PbI_2.

The dielectric constant of PbI_2 has been measured by several workers on different types of sample and at various frequencies to give results differing by over an order of magnitude. Dugan and Henisch (1967b), using single crystals, have repeated these measurements in the frequency range 10^2-10^5cps and at temperatures between 110°K and 450°K. They found the dielectric constant to be frequency independent below 210°K, but above this temperature to decrease with increasing frequency until a constant average value of 6.21 was reached at about 10^4cps. They also demonstrated the capacitance of specimens to be photosensitive at the lower measurement frequencies. These findings thus provide an explanation for the wide range of dielectric constant values previously reported.

A comparison of n^2 (=6.25), where n is the long wavelength refractive index obtained experimentally by Dugan and Henisch (1967b), with the constant value of the dielectric constant (=6.21), is very informative. It shows that the dielectric constant arises almost entirely from the electronic polarisation of the crystal, and PbI_2 would seem therefore less ionic than was previously thought.

3.3.7 Band Structure Model for PbI_2.

On the basis of the optical and photo-conductive data, Tubbs (1964) suggested the schematic energy band model shown in fig. 3.11. It involves a split valence band, due to spin-orbit interaction, and excitonic states both above and below the conduction band minimum. It should be noted that the value of the band gap is set at 3.1eV. Tubbs concluded this from a number of observations, such as a temperature-independent shoulder in the absorption spectrum and the second peak seen in the photoconductive response (fig. 3.6b) at this energy.

The above band scheme model has been extended by Tubbs and Forty (1965) to take into account the two exciton lines observed by them around 4900Å (fig. 3.8) for different polarisations of the incident radiation. They envisage the upper branch of the valence band to be split, due to the crystal field, by about 0.01eV, in similar

qualitative fashion to the valence band models proposed by Birman for CdS (1959) and Parsons, Wardzynski and Yoffe (1961) for CdSe. The two exciton lines are then interpreted as transitions from the two upper branches of the valence band to a localised exciton level below the conduction band.

The above valence band scheme has been utilised by Dugan and Henisch (1967a) to interpret their results of fundamental absorption and photoconductivity described in previous sections. Their suggested energy band model is shown in fig. 3.12. From their polarisation experiments, the energy interval between the two upper branches of the valence band is more definitely assigned at 0.048eV. The models, however, differ on the following points, for Dugan and Henisch have incorporated the results of other workers, notably Nikitine et al (1964) and Imai and Ishiguro (1959). The former concluded from studies of exciton spectra that a band transition occurs at 2.568eV in PbI_2 and that the first exciton level lies 0.033eV below the conduction band. Imai and Ishiguro attributed a peak in the absorption spectrum at 3.07eV to a transition to an exciton state, whereas Tubbs (1964) interpreted a shoulder in his absorption spectrum at this energy as indicating the onset of band-band transitions. The interpretation of Dugan and Henisch was that the peak corresponded to a

transition from the bottom valence sub-band to the first exciton level. Consequently, an energy difference of 0.54eV was assigned between the lower and upper edges of the valence band.

The above model of Dugan and Henisch was later rectified by them (1968) to take account of their photoconductive response (fig. 3.10a), photoluminescence spectra (fig. 3.10b), and photocurrent temperature quenching results, described in the previous section. The amended energy level diagram is shown in fig. 3.13. The transitions revealed by these experiments can be accounted for by this scheme, but note the arbitrary introduction of a level 0.1eV below the conduction band to account for the 2.31 and 1.85eV transitions. The latter feature in the photoluminescence spectra would then be achieved by a radiative transition from the 0.1eV level to that level 0.46eV above the valence band. It is pointed out that this transition would not then be apparent in the photoconductive response. That this is the case supports the 0.1eV level. However, one may then ask why the 2.31eV feature was not then in evidence? This model will again be the subject of discussion in Chapter 7.

CHAPTER 4

Theoretical Basis of Transport in Low Mobility Materials.

4.1 Introduction.

A layer compound such as PbI_2 is characterised by strong covalent, and even partially ionic, bonds within the layers, but by very much weaker van der Waals forces between layers. The interatomic orbital overlaps between adjacent layers may well be quite small relative to those within a layer. Consequently, one would expect a pronounced anisotropy in the electrical transport properties in the two directions. Conduction perpendicular to the c-axis (i.e. along the layers) should be associated with carrier mobilities of the order of $100 cm^2 sec^{-1} volt^{-1}$ at room temperature, which have in fact been measured in the case of GaSe and MoS_2 (section 3.2.1). Here the conventional semiconductor theory should be applicable. However, the transport along the c-axis, in the weakly overlapping direction, may well proceed by a fundamentally different mechanism. As this case is of particular interest in the present work, it is relevant first to examine the limits of validity of the band picture and then to discuss the transport theories which might be applicable.

4.2 Limits of Validity of Band Picture.

The requirements of Heisenberg's uncertainty principle are of fundamental importance in connection with transport within a narrow band. One criterion for the band approach to be a good one is that the uncertainty in the energy of a carrier after a scattering event should not exceed the bandwidth, W.

Thus, $$W \geq \hbar/\tau \qquad (4.1)$$

where τ is the scattering relaxation time. This enables a lower limit to be set on mobility for the band theory of conduction to apply.

Since, $$\mu = (e/m^*)\tau \qquad (4.2)$$

inequality 4.1 yields

$$\mu \geq \frac{e\hbar}{m^* W} \qquad (4.3)$$

The Bloch tight binding approach, applied to a simple cubic lattice of period a, leads to the following relation between the energy, E(k), of a carrier and its propagation vector k,

$$E(k) = C - 2J(\cos k_x a + \cos k_y a + \cos k_z a) \qquad (4.4)$$

where C is a constant, J is the exchange energy between an atom and one of its nearest neighbours, and k_x, k_y, k_z, are the components of k along the principal axes of the crystal (see, e.g. Dekker, p.260). The zone limits are given by $k_x, k_y, k_z = \pm \pi/a$ and the bandwidth is simply

$$W = 12J \qquad (4.5)$$

On the same model, the carrier effective mass at the band edge is given by

$$\frac{1}{m^*} = \frac{1}{\hbar^2} \cdot \frac{\partial^2 E(K)}{\partial K^2} = \frac{2}{\hbar^2} \cdot Ja^2 \qquad (4.6)$$

We can then write $\frac{1}{m^* W} = \frac{a^2}{6\hbar^2}$ and by substitution into inequality (4.3) obtain

$$\mu \geq \frac{ea^2}{6\hbar}.$$

For a = 4.5Å (the spacing between iodine atoms in adjacent layers, c.f. fig. 2.1), this leads to mobilities in the region of $1 cm^2 volt^{-1} sec^{-1}$ as a lower limit for the band approach to apply.

An alternative formulation by Fröhlich and Sewell (1959), takes into account the requirement that the electron within the band must have a mean kinetic energy which is larger than the uncertainty in energy resulting from the scattering process. This approach leads to room temperature mobilities in the region of $0.1 cm^2 volt^{-1} sec^{-1}$ as the lower limit for which the band approach is applicable.

4.3 The Small Polaron.

When the bandwidth is small, the charge carrier may remain in the region of a lattice site for a time long compared with the period of the lattice vibrations. As a result of the polarisation, the surrounding lattice

particles will be displaced to new equilibrium positions corresponding to a reduction of the total energy of the system. The induced lattice distortion will thus produce a potential well for the carrier, which will be essentially 'self-trapped' with a binding energy E_b. The carrier with its region of lattice distortion is known as a polaron. The term 'small polaron' is used for less polar media where the lattice distortion is fairly localised.

The main condition for the formation of a small polaron is $E_b \gg J$, where J is the overlap energy between neighbouring electron states. The transport of the small polaron has been investigated theoretically by Holstein (1959) and by others. The general results of these theories indicate that essentially two mechanisms can occur, which will now be discussed on the basis of the predicted μ v. 1/T given in fig. 4.1.

(a) At temperatures below T_c (the transition temperature between the two mechanisms), the transport of the small polaron between the neighbouring lattice sites occurs without absorption or the emission of phonons i.e. the polaron quantum number remains unchanged during the transition. In this case the polaron will move as a whole and one describes its transport in terms of Bloch functions. It can be seen from fig. 4.1 that in the low temperature region the mobility decreases with increasing

temperature, consistent with transport in a band. With increasing temperature, scattering becomes more intense and the scattering relaxation time τ will decrease. T_c is the temperature for which the polaron bandwidth $W = \hbar/\tau$ (equation 4.1). This means that the uncertainty in energy after a scattering event will be equal to the polaron bandwidth and the band description breaks down.

(b) For $T > T_c$, the transition of the polaron between sites will be accompanied by absorption and emission of phonons and the polaron will 'break up'. The transport is then a random diffusion process by a series of uncorrelated, phonon-assisted site jumps and referred to as hopping transport.

A somewhat different approach, by Toyozawa (1962), took into account the interaction of carriers with acoustic modes. The model considered was that of an elastic continuum in which the deformation extended over only a few unit cells. This contrasts with theories of the large polaron, applicable to ionic crystals, where the deformation is largely coulombic and extends over many lattice spacings. Toyozawa used the result of Bardeen and Shockley that the perturbing potential for the carrier due to the dilation is given by the local change in energy at the bottom of a band, $V(r) = E_d . \Delta x$, where Δx is the dilation and E_d the deformation constant. He showed that

if the electron-lattice coupling is large, localised states below the conduction band edge would arise. Three types of transport, distinguished as hopping, drift and band motion, were discussed.

Fig. 4.2 shows the relative positions of the available electron states plotted as a function of g^{-1}, where g denotes the electron-lattice coupling constant. For a simple cubic crystal of lattice period a, g is given by,

$$g = \frac{1}{6} \cdot \frac{E_{d.m}^2}{\hbar C a},$$

where C is the compressibility of the crystal. In fig. 4.2 E_t and E_a denote the ground state and first excited state of the polaron respectively.

For large values of g, ($g \geq 1.49$) i.e. strong coupling, the excited self-trapping state (E_a) also lies below the conduction band. On the other hand, for small values of g, ($g \leq 0.903$), the normal band picture applies and self-trapping becomes unimportant. Two types of carrier motion in which self-trapping plays a significant role were distinguished.

(a) In the range $g \geq 1.49$, the electron makes transitions to neighbouring sites via the excited self-trapping state. In this region the process would be essentially adiabatic and the hopping activation energy would be equal to the excitation energy of the self-trapping

state. In the case of strong coupling, the hopping activation energy is given by

$$\frac{0.184\ E_d^2}{Ms^2} < \epsilon < \frac{0.25\ E_d^2}{Ms^2} ,$$

where M is the mass of a unit cell and s is the velocity of sound.

(b) In the range $1.49 \geqslant g \geqslant 0.903$, the electron moves by a transition into the band where it is free to move until again self-trapped in a localized state. This is known as 'drift motion'. In this intermediate coupling range, the drift mobility activation energy is given by

$$0 < \epsilon < \frac{0.184\ E_d^2}{Ms^2} .$$

Both (a) and (b) imply an activated mobility i.e. $\mu \propto \exp(-\epsilon/KT)$.

4.4 The Electron-Phonon Interaction of Fivaz and Mooser.

A new model describing the mobilities of charge carriers in layer structures has recently been propounded by Fivaz and Mooser (1964). They showed that the marked anisotropy of such compounds results in a short range interaction between excess charge carriers and optical lattice vibrations. It is claimed that this model bears a general similarity to the electron-phonon model

of Toyozawa described above.

On examination of the effective potential in which the charge carriers in a layer lattice move, insight is gained into the mechanism of the interaction. In its simplest form the layer structure can be envisaged as a series of atomic layers stacked one upon the other. Consequently, the carriers may be said to move in a series of parallel potential wells, for there is a high and fairly wide potential barrier between the layers but a low and slowly varying potential within each layer. The interaction may therefore be described by means of a deformation potential,

$$\epsilon_d = a(d\epsilon_i/da) \qquad (4.7)$$

where ϵ_i is the energy of the local level within a potential well and a is the width of the well. If the potential within one layer is approximated by a deep square well, one obtains,

$$\epsilon_i = n^2\pi^2\hbar^2/2ma^2$$

and hence

$$\epsilon_d = -2\epsilon_i. \qquad (4.8)$$

For layer compounds a is of the order of a few angstroms, so that even for the lowest level the deformation potential may be as high as several electron volts. Thus, the importance of this interaction on the transport properties of charge carriers in layer compounds is clearly apparent.

The detailed theory of Fivaz and Mooser distinguishes between two regions, characterized by strong or weak carrier-lattice coupling. The transition between the two regions is discontinuous. When the carrier-lattice coupling is weak the carriers behave essentially as free quasi-particles and the diagonal components of the mobility (tensor) in the weak coupling limit are calculated to be,

$$\mu_{xx} = \frac{e}{2m_x w} \cdot \frac{1}{4\pi g^2} \cdot \frac{e^{\hbar w/kT} - 1}{1 + \hbar w/2kT} \qquad (4.9)$$

and

$$\mu_{zz} = \mu_{xx} \cdot \frac{12 I_z^2}{kT \pi^2 \hbar^2 / 2 m_x d_z^2} \cdot \left(1 + \frac{\hbar\omega}{2kT}\right). \qquad (4.10)$$

μ_{xx} and μ_{zz} refer to the mobilities parallel and perpendicular to the layers respectively, I_z is the overlap energy between adjoining cells in adjacent layers and d_z is the interlayer distance. The dimensionless carrier-lattice coupling constant g (different from that of Toyozawa) is given by,

$$g = \left(\frac{m_x}{4\pi MN}\right)\left(\frac{\epsilon_d}{a\hbar\omega}\right) \qquad (4.11)$$

where N = number of unit cells per unit area within a layer and M = reduced mass of unit cell (assumed here to be composed of two identical atoms). All other symbols in the above equations have their usual meaning.

μ_{zz}, of interest in the present work, can be written in the weak coupling limit (i.e. $g^2 \ll 1$) as:

$$\mu_{zz} = \frac{3eI_z^2 d_z^2}{kwg^2 T \hbar^3 \hbar^2} \left(e^{\hbar\omega/kT} - 1\right) \qquad (4.12)$$

On the other hand, if $g^2 > \frac{1}{2}$ the strong coupling condition applies in the Fivaz and Mooser treatment and self-trapping will predominate.

CHAPTER 5

Experimental Method.

5.1 Introduction.

The experimental method used for the drift velocity measurements is based on fast pulse techniques which have been developed in this laboratory for the study of charge transport and related problems in insulating solids (e.g. Spear (1960), Spear and Mort (1963)). In this section, the general features of the method will be considered in relation to the present work, and the following sections will deal with a more detailed description of the various parts of the experimental arrangement.

A block diagram of the experimental arrangement is shown in fig. 5.1. In a drift mobility experiment, the specimen S is prepared in the form of a platelet of known thickness d, and electrodes are evaporated on to the top and bottom faces, T and B. A very short duration excitation from the electron gun is focussed on to one side of the specimen. This is absorbed within a few microns and generates free electron-hole pairs. The application of an electric field E draws carriers of one sign out of the excited region. The transit time t_t is obtained by a charge integration technique. This will lead to the drift velocity v_d and the drift mobility μ_d

from the relations,

$$v_d = \frac{d}{t_t} \quad \text{and} \quad \mu_d = \frac{v_d}{E} \quad .$$

5.2 Electron Pulse Excitation.

The electron gun and the associated fast pulse techniques have been described in detail previously (Spear, 1960; Spear, Lanyon and Mort, 1962), and only a brief description will be given here.

As shown in fig. 5.1, a tetrode electron gun with a directly heated tungsten filament was used. Sliding "O" ring seals were incorporated into the filament assembly, making horizontal and vertical adjustment possible under running conditions. The electron gun and its associated components were raised to a negative potential of about 25KeV, and the second anode A_2 held at earth potential.

The gun was biased off by the potential V_B ($\sim$ 22 volts) applied between the cathode and the gun housing. A fast rising positive voltage pulse was applied from the mercury wetted contact relay (M) to the 75 ohm terminating resistor (R_T) between the grid and the gun housing, to switch on the gun for the duration of the pulse. The connecting line (CL) between the relay and the grid was terminated inside the gun housing to provide

a good match. The length of the excitation pulse could be varied between 2 and 300 nsecs by switching in different lengths of delay line (DL), by means of the coaxial switch (CS); typical pulse lengths used in the present experiments ranged from 5 - 30 nsecs. The beam current was controlled by the charging potential applied to the delay line.

The relay was triggered by a generator to which it was optically coupled by a GaAs lamp (GL). The generator was run at 50c.p.s. and incorporated a phase shift network, which allowed the phase of the trigger pulse to be varied.

The first anode (A_1) held at a fixed voltage (V_{A1}) of 300v. with respect to the negative accelerating potential, ensured that the beam current was largely independent of the accelerating potential. The beam was focussed on to the specimen by the magnetic lens (L).

The specimen holder (described in section 5.5) contained a small Faraday cup for collecting and measuring the incident beam. By turning a switch (not shown in fig. 5.1), a steady potential could be applied to the biasing circuit to give a steady beam current. This was necessary in order to position the incident beam either on to the specimen or into the Faraday cup.

The advantages of electron excitation lie

in the ease with which the pulse length and intensity may be varied. It is also possible to vary, within certain limits, the depth of penetration of the beam into the specimen by adjustment of the accelerating potential.

5.3 Electronics - General.

It has been found in drift velocity experiments that the magnitude of any space charge field resulting from the trapping of the injected carriers may be considerably reduced by pulsing the applied field. The main problem lies then in the synchronisation of the electron pulses with the field pulses.

A Schmitt trigger was used to derive synchronisation pulses (2) from the mains (1), (fig. 5.2). Field pulse synchronisation was achieved by dividing the synchronisation pulses (2) by 1, 2, 4, 8 or 16, as desired, and then generating a relay drive pulse for each of the resultant pulses. The field relay thus closed 50, 50/2, 50/4, 50/8 or 50/16 times each second, and the width of the pulses could be varied from 10 to 30 ms. by varying the width of the relay drive pulses. In fig. 5.2, the field relay is shown closing 50/4 times per second (4).

It has previously been mentioned that the problem of triggering the electron pulses from ground to the gun potential was overcome by means of optical

coupling. The triggering and synchronisation were achieved by using a GaAs lamp (Plessey GALI), which produced 10 μs pulses of near infra-red light ((6) in fig. 5.2). These were detected by an OCP71 phototransistor, and used to synchronise the electron pulses (7) with a variable delay of up to 20ms. to allow for positioning of the electron pulse with respect to the field pulse.

5.4 Determination of the Transit Time.

For the measurement of transit times, a charge integration method was employed, the principle of which is illustrated in fig. 5.3. The excitation pulse, absorbed in a depth $d_p \ll d$, generates N_g electron-hole pairs close to the top electrode (T). Due to the rapid recombination that will occur in this region, only a number N of one type will be drawn into the bulk of the specimen under the action of the applied field. These will induce a charge on the bottom electrode B proportional both to their number and to the distance moved. The integrated charge $q(t)$ at a time t will give rise to a potential difference $\Delta V(t)$ across the resistance R. If C is the total capacity across R, this is given by,

$$\Delta V(t) = \frac{Nex(t)}{Cd} = \frac{Ne\mu_d Et}{Cd} \qquad (5.2)$$

It is assumed that the value of RC is much greater than

the time during which the drift takes place, and that no carriers are lost during transit.

The value of $\Delta V(t)$ expected under ideal conditions is shown in fig. 5.4(a). The linear increase in ΔV terminates sharply at $t = t_t$. By measuring the transit time at various fields, the drift mobility is obtained from the gradient of a graph of $\frac{1}{t_t}$ against E using equation (5.1).

From equation (5.2), it is seen that the potential difference across the resistance (R) is inversely proportional to the total capacity C across R. To reduce this capacity to a minimum, a cathode follower (fig. 5.5) was used before the signal was detected. The signals were displayed on a Tektronix 581 oscilloscope fitted with a type 86 vertical plug-in unit. The maximum charge sensitivity of the system was such that a vertical deflection of 1cm. on the oscilloscope corresponded to the transit of about 5.10^5 electrons.

In order to observe a well-defined transit of carriers, the following conditions have to be satisfied:

a) The drift of the generated carriers across the specimen is a perturbation from space charge neutrality. If this is not to be neutralised, the dielectric relaxation time of the crystal must be longer than the transit time. This is satisfied by the low conductivity specimens

used in these experiments.

b) The transit time must be appreciably longer than the rise time of the measuring equipment.

c) The thickness of the drifting sheet of charge should be much less than the specimen thickness. This can be satisfied by making the excitation pulse duration much shorter than t_t and by ensuring that the depth of penetration of the excitation pulse is much less than d.

d) Above a certain carrier density the space charge effects of the moving carriers become important and modify the field distribution. Experience has shown that, to avoid this effect, it is necessary to limit the number of electrons in the excitation pulse to about (10^5) electrons, leading to less than 10^7 electrons drifting across the specimen.

e) The carrier lifetime with respect to deep traps must be greater than t_t. If this condition is not satisfied, there will be a loss of carriers to such traps during the transit. These trapped charges will alter the field distribution and may affect it appreciably if present in sufficient quantity.

Even if all the above conditions are satisfied, there will still be some broadening of the charge cloud, due to diffusion and the statistical nature of shallow trapping, which may make the transit too

diffuse for accurate measurements.

If the transit time is of the order of the lifetime with respect to a spatially uniform distribution of deep traps, then the charge integration observed will be of the shape shown in fig. 5.4b. If t' is defined by the intersection of the tangent at $t = 0$ and $t \gg t_t$, then Spear and Mort (1963) have shown that,

$$\frac{1}{t'} = \frac{1}{\tau}\left[1 - \exp\frac{(-t_t)}{\tau}\right]^{-1} \qquad (5.3)$$

The value of t' extrapolated to zero field will give τ as indicated in fig. 5.6. Over the range of E generally used, the mobility obtained from the gradient of a graph of $\frac{1}{t'}$ against E is only a few percent different from that obtained by plotting $\frac{1}{t_t}$ against E. At a given value of E however, equation (5.3) must be used to obtain the true drift velocity $\frac{d}{t_t}$, if required, from the measured quantity $\frac{d}{t'}$.

5.5 Specimen Holder.

The specimen holder used in all drift velocity and conductivity measurements is shown in fig. 5.7a.

The specimen (S) was mounted on a thin mica base M (fig. 5.7b) with a little silicone grease to ensure good thermal contact. The brass plate (H) was also smeared with silicone grease and the mica base affixed to it by means of two screws. Electrical screening of the

specimen and its leads was provided by the box (H) and the lid (L). It was possible to vary the temperature of the specimen by cooling or heating the copper rod (C). Low temperatures were obtained using as coolants dry ice in alcohol and liquid nitrogen, whilst an electrically heated ceramic jacket allowed temperatures of up to 500°K to be attained. The rod (C) was connected to the brass plate (A) by the thin walled stainless steel tube (D). The tube D and the evacuated gap between C and D provided excellent thermal insulation between C and A. The plate A was clamped underneath the electron bombardment gear against a neoprene 'O' ring seal, and the complete specimen housing above A and the electron gun was then evacuated to a pressure of 10^{-4} torr.

The incident electrons could be focussed through the lid (L) either on to the specimen or, if the incident pulse itself was to be measured or observed, on to the Faraday cup (F) mounted on an insulator. Electrical connection was made to the specimen electrodes through the glass metal seals T and B in the plate A. The Chromel - Alumel thermocouple leads (TC), which measured the temperature of the specimen, passed through the remaining seal in the plate.

5.6 Specimens and their Preparation.

The crystals used in the present investigation were obtained from boules several mms. thick supplied by Dr. Merz of R.C.A.,Zurich. Most of the results were obtained from two boules,which will in the following be referred to as 'Boule A' and 'Boule B'. The thin platelets required for the drift velocity measurements were cleaved from the thicker crystals by means of the following technique. A section of the face was placed into contact with double-sided tape adhering to a microscope slide. The crystal was then gently removed,resulting in a flake being parted from the main body. A soft brush was now inserted beneath the flake and gently pushed along the layers to complete the partition process. Platelets ranging in thickness from 20 to 70μms. were produced in this manner,but only those with a large enough surface area for the application of electrodes were used.

The next step was to evaporate metal electrodes on to the opposite faces of the crystal at pressures below 5×10^{-5}torr. The electrodes were usually gold, although indium was used to investigate effects due to changes in contact barrier. All the specimens used in the photoconductivity experiments were each prepared with a split,semi-transparent,top electrode, the separation being 1mm. This was obtained by using a

shadow mask technique in the evaporation process.

In order to determine the drift velocity and mobility of the carriers, it is necessary to know accurately the specimen thickness. This was measured by means of a miniature, optical, lever gauge having a magnification of about 10^3 (Spear, Adams and Henderson, 1963). The main advantage of this method lies in there being small chance of damaging the fragile specimens. The PbI_2 crystals, however, tended to be somewhat 'wavy' and this introduced some difficulty in the thickness measurement. Variations of 10% were observed; this represents the combined effect of genuine thickness variation and errors introduced by the 'wavy' nature of the specimens.

5.7 Dark Conductivity Measurements.

To clarify further the conduction mechanism, the dark conductivity of thin platelets of PbI_2 was measured parallel to the c-axis as a function of temperature. At each temperature, the crystal was allowed an hour to reach a state of thermal equilibrium before the application of a steady field. The current was then measured with a Hewlett Packard d.c. microvolt ammeter, model 425A. It was assumed to have reached an equilibrium value when it changed by less than 1% over a twenty minute period. Measurements were taken for both increasing and decreasing

temperature.

5.8 The Photoconductive Response of PbI_2.

Photoconductivity measurements were performed at room temperature for the incident radiation parallel to the c-axis and, also, for the direction of current flow both perpendicular and parallel to this axis. An Optica grating monochromator, with a spectral halfwidth of 16Å per mm. slit width, was employed in conjunction with a tungsten source. The dark- and photo-conductivity were determined by the use of a pulsed field of 600 msec. duration and a repetition period of 1.5secs. The photocurrent was measured by observing the pulsed voltage appearing across the $10^6\,\Omega$ resistor in the input of a Tektronix 581 oscilloscope incorporating the type 1A7 low noise, high sensitivity, plug-in unit. The field was pulsed for a considerable time to allow a state of equilibrium to be reached before the final reading was taken. An alternative d.c. method was also employed, using the Hewlett Packard instrument. Once again, the dark- and photocurrents were allowed to reach equilibrium, and the reading was taken when the current had changed by less than 1% over a twenty minute period.

CHAPTER 6

Experimental Results.

6.1 Room Temperature Hole Drift Mobilities and Lifetime Measurements.

Approximately twenty crystals, ranging in thickness from 20 to 70 μms and all cleaved from the same boule A, have been investigated. When fitted with gold-gold electrodes the dark conductivity of the specimens along the c-axis was of the order of $10^{-12}(\Omega\,\mathrm{cm})^{-1}$, but varied from specimen to specimen. The ~~effective~~ conductivity within the drifting charge layer may be estimated from the number and velocity of the drifting charges, and the duration of the incident electron beam. This leads to the conductivity within this region, which was of the order $10^{-9}(\Omega\mathrm{cm})^{-1}$.

It must be emphasised that the results presented in this chapter refer only to holes. Although electron signals were observed, it was not possible to determine the transit time from these as the lifetime was considerably less than 100 nsecs. A typical curve of $1/t'$ against E for hole transport is given in fig. 6.1. At low applied fields the observed pulse had the shape shown in fig. 5.4b. With larger fields, the rising edge of the pulse became practically linear, as in fig. 5.4a.

As previously mentioned in section 5.4, the intersections of the tangents at $t = 0$ and $t > t_t$ defined t', which was measured as a function of the applied field E. It is seen from fig. 6.1 that the curves have a linear portion at the higher field values which, when extrapolated, does not pass through the origin of co-ordinates. Furthermore, at low fields, the experimental points do not lie on the extrapolated straight line but tend to a constant $1/t'$ value of $1/\tau$, where τ is the free hole lifetime with respect to deep traps. Lifetimes found in the present boule A ranged over an order of magnitude, from 0.5μs to 4μs, and the room temperature hole mobilities lay between 1.8 and 5$cm^2 volt^{-1} sec^{-1}$. Platelets cleaved from the sedond boule B showed such limited hole lifetimes, of the order of 150nsecs, that drift velocity measurements were not possible. In table 1, the room temperature hole mobilities, lifetimes and other information have been collected.

One PbI_2 platelet grown from silica gel, kindly supplied by Professor H.K. Henisch, was also investigated. Because of its method of growth, it should have had far fewer defects than boule A, but very surprisingly neither hole nor electron transits were observable. In fact, the hole signal showed a rising edge equal in duration to the incident electron beam pulse but it then

decayed extremely rapidly. The decay time constant was far shorter than the integrating time constant of the input circuit.

6.2 Temperature Dependence of the Hole Drift Mobilities.

The dependence of the hole drift mobility on the specimen temperature has been investigated for many crystals, mostly in the region from 350°K to 200°K. Results have been obtained on two samples up to 500°K, and on another one down to 150°K. In these experiments great care was necessary if consistent results were to be obtained. Particular attention was given to allowing the specimen time to reach the temperature indicated by the thermocouple before a measurement was made. This was important at the lower temperatures where a few degrees error causes an appreciable variation in $10^3/T$.

A graph of mobility (μ) versus $10^3/T$, plotted semi-logarthmically, is given in fig. 6.2 and collects a number of the higher room temperature mobility specimens. All are seen to be linear on this scale and show mobilities which increase with decreasing temperature. This is a general characteristic of a lattice-controlled transport. Thepresent results can be represented by an equation of the form $\mu \propto \exp \epsilon/kT$, where ϵ represents an energy. It is interesting to note that at $(10^3/T) = 3$,

for example, there exists a correlation between μ and ϵ, in the sense that ϵ decreases with increasing μ. Fig. 6.3 shows a set of results for lower room temperature mobility specimens; the same correlation is observed between μ and ϵ. The onset of another transport mechanism at lower temperatures is also indicated in fig. 6.3, where all curves turn over sharply in the region of 250°K. Below this temperature the mobilities are then either essentially temperature independent or, in the case of specimen P18, a decreasing function of temperaure. This branch has an activation energy of 0.032eV and its significance, together with information provided by the other specimens, will be discussed in the following chapter.

Fig. 6.4 shows the temperature dependence of one of the few exceptional specimens whose hole mobility did not show a linear relation between $\log \mu$ and $10^3/T$. It can be seen that at lower T the mobility is temperature independent.

The results for the region of increasing mobility with decreasing temperature indicate that the lower the mobility at, say, room temperature, the greater is the value of ϵ in the relation $\mu \propto \exp \epsilon/kT$. Fig. 6.5 shows, on a log-log plot, the mobility at T = 333°K against ϵ. It is seen to be linear and shows that there exists a definite correlation between these two quantities.

The relation between ϵ and $(\mu)T = 333°K$ on a linear scale is given in fig. 6.6, from which it can be concluded that, for all practical purposes, ϵ is tending towards a value of between 15 and 20meV.

6.3 The Effect of Heat Treatment on the Hole Mobility and its Temperature Dependence.

It appeared of interest to determine whether changes in the temperature dependence could be induced by heat treatment. Specimen P37, for example, was moderately heated in vacuo at 120°C for 1½hrs. The resulting temperature dependence, together with that before heat treatment, is shown in fig. 6.7. The room temperature mobility is seen to have increased from 2.1 to 2.8$cm^2volt^{-1}sec^{-1}$ and, consistent with the above results, the value of ϵ has decreased. Moreover, the turnover point has moved to a lower temperature. The $1/t'$ versus E plots also revealed that the room temperature lifetime had increased from 1.3 to 2μs.

Specimen P29 was subjected to three successive heat treatments, and the resulting temperature dependence after each stage is given in fig. 6.8. The first heat treatment, for 1½hrs at 150°C, realised no change in the lifetime but the room temperature mobility increased from 4 to 5.6$cm^2volt^{-1}sec^{-1}$. However, the linear

relation between log μ and $10^3/T$ was largely destroyed. The specimen was then further baked for 8hrs at 150°C. This time the lifetime, in similar fashion to P37, increased, from 0.85 μs to greater than 1 μs. The room temperature mobility was further increased, and the general shape of the mobility-temperature dependence retained. The specimen was finally subjected to prolonged heating for 20hrs at 175°C, whereupon the original temperature dependence was restored but the mobilities remained at somewhat higher values. The room temperature lifetime had decreased from the previous run. This final heating now produced the other transport region at lower temperatures, the transition point being once again in the vicinity of 250°K. Although the range of temperatures accessible in this region was limited due to the diminishing lifetime, the results indicate an activation energy of 0.043eV.

Fig. 6.9a shows the results of a high temperature run on specimen P30. The noteworthy feature of this graph, besides its non-linearity on this scale, is the discontinuity around 400°K. This was also apparent, at approximately the same temperature, in another specimen heated to 500°K, but the crystal had a short lifetime and consequently transit measurements could not be taken below ice point. These discontinuities will be seen to be associated with a change in the conduction mechanism, as

observed in dark conductivity measurements. In fact, they are probably due to the space charge associated with the Pb^{2+} ions, for around this temperature they begin to make a contribution to the conductivity (see section 6.6). Specimen P30, heated to 500°K, was subsequently allowed to cool to room temperature and a second run performed (fig. 6.9b). The mobility is seen to have increased at room temperature and above, and there is now a linear relationship between $\log \mu$ and $10^3/T$; also the discontinuity at 400°K is absent. However, the mobility below room temperature now became temperature independent, similar to a number of other specimens, but the transition temperature is higher in this case. It is interesting to note that the room temperature lifetime was smaller after heat treatment.

6.4 Effect of Steady Electron Bombardment on Mobility and its Temperature Dependence.

PbI_2 has been shown to decompose under the action of a high energy electron beam. In view of this, it was considered instructive, since transit measurements are achieved by high energy electron pulses, to see the effect of steady electron bombardment on the mobility. A specimen was bombarded with a steady electron current of $15 \mu A cm^{-2}$ at an energy of 30keV for 10 minutes, its

mobility-temperature variation having been previously determined. The specimen was allowed 48hrs for any defects produced to diffuse and attain equilibrium, and then the mobility again measured as a function of temperature. There was virtually no change, within experimental error, in either mobility or its temperature dependence.

6.5 The ~~Quantum~~ Efficiency of Carrier Generation by Electron Bombardment.

It was noticed during the course of drift velocity experiments that at higher fields the charge drawn across the crystal tended to saturate. This being so, it should then be possible to determine the efficiency of electron bombarment in generating electron-hole pairs, from a knowledge of the incident charge and the bombarding voltage. Previous experiments performed in this laboratory suggest that the primary energy required for the production of an electron-hole pair is approximately three times the band gap. This is supported by the theoretical work of Shockley (1961) and of Klein (1968).

The currents used in these experiments were of the order of 0.15 μA, with a generation time of 15nsecs. Several crystals, all from boule A, were investigated and graphs plotted of charge drawn across the crystal as a function of the applied field. One such curve is given in fig.6.10, and does indeed saturate at the higher

fields. This particular specimen yielded 42eV for the energy required. Other similar values were obtained from all specimens with a mean of 39.5eV.

6.6 Temperature Dependence of Dark Conductivity.

Current-voltage characteristics were first determined for specimens with (a) both electrodes of gold and (b) one indium and one gold electrode, at both room temperature and 130°C. The results are shown in figs. 6.11 and 6.12. From the former it can be concluded that crystals with gold-gold electrodes produce ohmic contacts, whilst fig. 6.12 shows that an indium-gold electrode combination can be either ohmic or injecting. The former prevails when holes enter the crystal through the indium electrode and electrons through the gold, but when reversed the combination becomes injecting. The difference in magnitude should also be noted. It is proposed that these differences arise because the indium electrode is completely blocking for holes, and hence highly injecting for electrons. Consequently, the linear characteristic is due solely to electron conduction, and the non-linear one due to the heavy injection of electrons through the indium electrode.

The following conditions are necessary for the above to apply (on the assumption that surface states

do not play a predominant role):

$$\phi_{Au} \geq \phi_{PbI_2} \qquad (6.1)$$

$$\phi_{In} < \phi_{PbI_2} \qquad (6.2)$$

and therefore $\phi_{Au} > \phi_{In}$ (6.3)

where ϕ_x = work function of X.

Now, $\phi_{Au} \simeq 4.9$eV and $\phi_{In} \simeq 3$eV and the photovoltaic measurements of Henisch and Srinivasagopalan (1966) show that $\phi_{Au} \simeq \phi_{PbI_2}$, but that ϕ_{In} is considerably less than ϕ_{PbI_2}. The model is therefore strongly supported.

The dark current I as a function of temperature was determined for specimens with gold-gold and gold-indium electrodes. A graph of log I vs $10^3/T$ in the temperature region 276°K to 435°K is given in fig. 6.13 for a specimen with both electrodes of gold. It is linear and reveals an activation energy of 0.27eV. Fig. 6.14a shows a plot for a similar specimen. A linear region, with an activation energy of 0.26eV, is again in evidence at the lower temperatures, but a very sharp change in gradient is apparent at T = 403°K. This indicates the onset of another conduction mechanism. For this specimen, the curve has an activation energy of 1.4eV. Fig. 6.14b shows the results obtained when cooling from 470°K; the transition is now less sharp and appears to have moved to a slightly lower temperature. These two specimens are typical of all crystals tested with both electrodes of

gold. They showed a mean activation energy of 0.26eV at lower temperatures and of 1.3eV in the high temperature region. However, the transition temperature between the two mechanisms varied between approximately 400°K and 450°K.

A representative curve for one of the specimens with indium-gold electrodes is given in fig. 6.15. The positive potential is applied to the indium side. The results are similar to those in fig. 6.14; the gradient in the high temperature region is once again 1.3eV, but the low temperature region shows a mean activation energy of 0.55eV for this electrode combination. The transition temperature varied between 400°K and 450°K.

6.7 The Photoconductive Response.

The photoconductivity as a function of wavelength, at room temperature, has been measured on PbI_2 platelets cleaved from both boules A and B. The monochromator output, in terms of photons sec^{-1}, is given in fig. 6.16 as a function of wavelength. All photocurrents subsequently measured were standardised to the output at 5050Å i.e. 10^{12} photons sec^{-1}.

The results for boule B will be described first, and a sample photoconductive response curve is given in fig. 6.17. The radiation was always incident parallel to the c-axis, and curves (a) and (b) in these diagrams

refer, respectively, to photoconduction parallel and perpendicular to this axis. It is seen that the absorption edge, considered to occur at that energy at which the photocurrent is half that at the maximum, is located around 2.35eV at room temperature. Further, the peak response for conduction along the c-axis occurs at slightly higher energies than for conduction perpendicular to it. From this maximum the response falls exceedingly sharply with increasing energy, the half-width of the resulting peak being of the order of 0.05eV. For the photocurrent I_p parallel to the c-axis the response now remains essentially constant until 2.9eV, at which energy it rises slowly to exhibit a broad peak centred around 3.3eV. It was not possible to observe this peak for conduction perpendicular to the c-axis, due to the diminishing lamp output with increasing energy, and the much smaller response in this case. For the majority of specimens, the photoresponse (I_p parallel to the c-axis) was about equal at the two peaks. However, the results for one specimen which did not conform to the general pattern are shown in fig. 6.18. A small peak can still be seen around the absorption edge, but the photoresponse now slowly increases and the 3.3eV peak is about three times greater than that at 2.4eV.

Heat treatment has been shown to affect the mobility and its temperature dependence. For this reason

one specimen was heated in vacuo for 13hrs at 130°C. The resulting photoresponse for the photocurrent along the c-axis is given in fig. 6.19b and to be compared with 6.19a, that before heat treatment. The distinctive differences are clearly seen to be an increase in photoresponse (note the different scales and the fact that a smaller field was used in the heat treated case) and the shift of the absorption edge to higher energies after heat treatment.

A typical photoconductive response curve for a crystal cleaved from boule A is shown in fig. 6.20a and b. It is quite different from the foregoing results obtained from boule B. The absorption edge is shifted about 0.05eV towards higher energies and the sharp peak previously observed is now absent. Instead, after the initial absorption, the photoresponse falls fairly slowly with increasing energy. It also shows no signs of a second peak located at 3.3eV.

CHAPTER 7

Discussion of the Experimental Results.

7.1 The Hole Mobility and its Temperature Dependence.

The results of section 6.1 show that measurements of μ along the c-axis yielded mobilities between 2 and 5 $cm^2 volt^{-1} sec^{-1}$ at room temperature. The theoretical discussion given in section 4.2, together with the fact that μ rises with decreasing T, lead to the somewhat unexpected conclusion that the transport takes place in a band which may ,however, be narrow. The form of the temperature dependence at room temperature and above suggests that scattering by optical modes may be the predominant mechanism.

A more detailed interpretation of the results shown in figs. 6.2 and 6.3 and also of the close correlation between μ and ϵ (fig. 6.6) presents many problems. In the following an attempt has been made at an explanation in terms of each of the two transport theories discussed in Chapter 4.

7.1.1 Interpretation in terms of the Small Polaron Theory (Holstein).

We are dealing here with transport in

a small polaron band (section 4.3). In most applications of this theory (e.g. to S_8, Adams and Spear (1964) and NiO_2, Austin et al (1967)) the charge carrier is treated as being localised near an atom or molecule of the lattice where it interacts with the vibrational modes. In attempting to apply this theory to a layer structure we are deviating from previous models. Here it is assumed that the carrier is essentially confined to a two-dimensional I-Pb-I layer, and we use the concepts of the small polaron theory to describe the transfer between successive layers along the c-axis. Thus the main difference lies in the fact that the carrier has now a far more delocalised character, being associated with a layer rather than a particular atom or molecule. Whether such an extrapolation of small polaron theory is justifiable is difficult to assess, although it should be remembered that the theory as derived by Holstein is based in any case only on a linear chain model. The following interpretation is an exploratory attempt and must therefore be regarded with some caution.

According to Holstein, the small polaron mobility in a narrow band is given by,

$$\mu = \frac{2e\omega_0 a^2}{kT}\left[\frac{E_b \operatorname{csch}(\hbar\omega_0/2kT)}{\pi\hbar\omega_0}\right]^{1/2} \exp\left[\frac{-2E_b}{\hbar\omega_0}\operatorname{csch}(\hbar\omega_0/2kT)\right]$$

Here $\hbar\omega_0$ is taken to represent the predominant optical phonon energy and E_b is the polaron binding energy. The

dimensionless carrier-phonon interaction parameter γ is defined by the ratio ,

$$\gamma = E_b/\hbar\omega_o$$

To investigate the fit of the theory to the experimental curves (at temperatures above the low temperature turnover shown for instance in fig. 6.3), a computer was used to calculate μ for values of $\hbar\omega_o$ between 0.03eV and 0.12eV in 0.01eV steps at T = 400°K, 333°K, 250°K, and 200°K. For each point γ was varied betwwen 0.2 to 8.0 in steps of 0.2.

Representative curves are given in fig.7.1 for values of $\hbar\omega_o$ between 0.04eV and 0.12eV and the E_b values indicated. It should be noticed that all the curves correspond to a constant value of $\gamma = 0.8$. It can be seen that although the mobilities are of the correct magnitude, the curves are by no means as linear as the majority of experimental results. In fact, they resemble more closely the exceptional case shown in fig. 6.4.

For the purpose of investigating the general fit of the experimental results with the computed data, the former are compared in the following with the gradient to the computed curves at $10^3/T = 3$. It will first be assumed that $\hbar\omega_o$ is a constant, characteristic of all crystals. In this case the mobility and temperature

dependence of specimen P15 can, for instance, be fairly well represented by $\hbar\omega_o = 0.045$eV and $\gamma = 0.4$ (i.e. $E_b = 0.018$eV). However, if this value of $\hbar\omega_o$ is used with different γ's to generate other curves it is found that, although a steeper temperature dependence can be obtained with larger γ (e.g. for specimen P18), the corresponding calculated mobility values are far too low. The most satisfactory compromise is a value of $\hbar\omega_o = 0.090$eV and fig. 7.2 shows the family of curves that can be obtained by allowing E_b to vary in order to reproduce the range of the observed temperature dependence. As there is only approximate agreement between theoretical and experimental mobilities, it is concluded that with $\hbar\omega_o$ = constant, the small polaron band description can only give a semi-quantitative fit to the results.

In the second approach, but still within the context of the small polaron theory, both E_b and $\hbar\omega_o$ were assumed to vary between one specimen and another. On the basis of the computer results those parameters ($\hbar\omega_o$ and γ) were chosen which gave the best fit to the experimental results. In fig. 7.3 $\hbar\omega_o$, determined in this way, is plotted against the experimental mobility at T = 333°K. The graph is similar to that shown in fig. 6.6 and suggests an asymptotic value of $\hbar\omega_o \simeq 35$meV. It may be significant to note in this context that a

fundamental optical phonon energy of about 30meV was inferred by Dugan and Henisch (1968) from their photo-luminescence spectra (section 3.3.6, fig. 3.10b).

7.1.2 Interpretation in terms of the Model of Fivaz and Mooser.

Examination of the mobility μ_{zz} derived by Fivaz and Mooser for the condition of weak carrier-lattice coupling (section 4.4), shows it capable of generating the temperature dependence that was experimentally observed i.e. $\log \mu \propto 1/T$. However, for its application in the present context it must be assumed that $\hbar\omega$ varies between specimens.

Fivaz and Mooser have shown that μ_{zz} is given by equation 4.12,

$$\mu_{zz} = \frac{3eI_z^2 d_z^2}{\hbar\pi^3} \frac{1}{g^2} \frac{1}{\hbar\omega Tk} \left(\exp(\hbar\omega/kT)-1\right) \qquad (4.12)$$

Now g^2, given by equation 4.11 can be written as

$$g^2 = \frac{G^2}{(\hbar\omega)^2} \qquad (7.1)$$

where $G^2 = \left(\frac{m_x}{4\pi MN}\right)\left(\frac{\epsilon d}{a}\right)^2$

and is therefore substantially constant.

Therefore $\mu_{zz} = A(\hbar\omega/kT)(\exp(\hbar\omega/kT)-1) \qquad (7.2)$

where $A = \frac{3ed_z^2 I_z^2}{\hbar\pi^3 \cdot G^2} = 0.15 I_z^2$, if μ_{zz} is expressed in practical units and $d_z = 4.5$Å.

Application of (7.2) to the experimental results yields the values of A and $\hbar\omega$ necessary to describe the experimental results. Sample results are given in Table 2. It is seen that $\hbar\omega$ is required to vary between 124meV for P18 (the specimen with largest ϵ) to less than 1meV for P15. Specimens P17 and P8 would need, on this model, even smaller $\hbar\omega$'s.

At this point it must be borne in mind that, although the weak-coupling region applies for $g^2 < \frac{1}{2}$, (7.2) is only valid if $g^2 \ll 1$ (section 4.4). Comparing $g_{P18}\left(=\frac{G}{124}\right)$ with $g_{P15}\left(=\frac{G}{172}\right)$, it is seen that g^2 is required to vary over at least four orders of magnitude. It is therefore possible that the condition $g^2 \ll 1$ may no longer hold for those specimens which require a very small $\hbar\omega$ (say, less than 10meV). Although these specimens may still conform to the weak-coupling region, i.e. $g^2 < \frac{1}{2}$, equation (7.2) is unlikely to give the correct mobility in the extreme cases.

An estimate of the overlap energy I_Z is now possible from a knowledge of A. Using the condition that $g^2 < \frac{1}{2}$, calculation gives the maximum value of I_Z, listed in Table 2. They would appear to be perfectly reasonable. An important aspect to notice in this context is that in this interpretation, large phonon energies correspond to small overlap. A physical explanation of

this point will be attempted in the following section.

Further examination of the calculated data reveals the following:

$$(\hbar\omega)_{P18} : (\hbar\omega)_{P31} \simeq 60:1$$
$$\text{but} \quad (I_z)_{P31} : (I_z)_{P18} \simeq 7:1.$$

One concludes that the variations in I_z required by this theory are about an order of magnitude less than those required by $\hbar\omega$. Once again this seems reasonable.

A very direct check that is possible is to predict the form of fig. 6.6. The gradient ϵ is given by $\epsilon = \frac{d\log\mu}{d1/kT}$. It is shown in Appendix 1 that

$$\epsilon = kT + \hbar\omega + \frac{A(\hbar\omega)^2}{kT} \cdot \frac{1}{\mu} \qquad (7.3)$$

In the limit, as $\hbar\omega \to 0$, $\epsilon \to 2kT$ i.e. 57.2meV for $T = 333°K$. In fig. 7.4 the solid line represents the calculated values of ϵ from equation (7.3) using the $\hbar\omega$ and μ listed in Table 2. The experimental points are the ϵ values given in Table 1. The agreement shows that the Fivaz and Mooser theory leads to a consistent interpretation of the results and is in this respect preferable to the Holstein theory.

7.1.3 Physical Interpretation.

Application of Holstein's small polaron theory to the experimental results requires variations in both E_b and $\hbar\omega_o$. The model of Fivaz and Mooser

requires variations in $\hbar\omega$ and A, and hence in the overlap energy I_z.

The binding energy E_b will be considered first. It is suggested that the variations may arise from one or more of the following.

(i) There are many lattice defects present in the structure, as would be expected in a crystal grown from the melt, but the density is extremely large (about 10^{19}–10^{20} cm^{-3}) and likely to be different from specimen to specimen. A hole will then find itself bound to a lattice site with a certain binding energy in one specimen, but in another will be surrounded by a different defect density leading to a different binding energy. This being so, annealing will remove lattice defects and thereby reduce the polaron binding energy, for E_b will be a minimum in the perfect lattice. According to Holstein's theory, this will increase the mobility and decrease the temperature dependence. This is in accordance with the experimental results on heat treated specimens (e.g. P37, fig. 6.7).

(ii) The original boules (i.e. boules A and B) were fairly free from defects. A large defect density was then generated by the cleaving process. It is quite possible that the lattice planes were displaced from their normal equilibrium positions, but obviously to a different degree in each platelet. The reasoning to explain the

variations in E_b and μ then follows (i) above.

(iii) The original boule was constructed of polytypes, each polytype element extending for, say, 1000Å along the c-axis. Each platelet cleaved from the boule would then be a polytype admixture and the overall binding energy would depend on the proportion of each polytype present. However, if this is the sole reason for E_b variations, then the heat treatment results require for their explanation that one polytype is transformed into another with a lower E_b.

It is relevant in this context to consider the results of Brebner and Mooser (1967) on GaSe polytypes, described in section 3.2.2. They concluded that different polytypes lead to different ionic contributions to the weak interlayer bonding. Hence, the binding energy of the small polaron in PbI_2 would be expected to differ between polytypes.

Whether (i), (ii), or (iii) applies, the binding energy E_b obtained from Holstein's equation will then be a macroscopic average of its fluctuations on a microscopic scale throughout the crystal.

The variations in $\hbar\omega$ required by both Holstein and Fivaz and Mooser can also be explained qualitatively by a variable, but large, defect density or possibly by the polytype hypothesis. It is known that

the introduction of defects undoubtedly affects the phonon spectrum of a perfect crystal, but the theoretical predictions to date are somewhat limited due to the extreme complexities involved in the computation. However, it is known that a sufficiently light impurity atom, or one bound more tightly to the host crystal than the atoms of the host crystal are bound to each other, gives rise to a mode of vibration whose frequency is greater than the maximum frequency of the unperturbed crystal. This is known as a localised phonon mode. It is proposed that such modes are responsible for the $\hbar\omega$ variations.

The defect involved is assumed to be an interstitial lead atom or ion, situated in the gap between adjacent I-Pb-I layers. It is reasonable to assume that PbI_2 is at least partially ionic, even though the measurements of Dugan and Henisch (1967b), described in section 3.3.6, indicate that it is less ionic than was previously supposed. Therefore, in the absence of other Pb atoms (or ions) the defect will probably be more tightly bound to its nearest I atoms (or ions) and will hence give rise to localised phonon modes. The more perfect is the PbI_2 crystal, the smaller will be the effect of this higher frequency phonon mode on the motion of the carrier. As the impurity density increases, higher frequency modes will become more predominant. The effective

$\hbar\omega$ in both Holstein's and Fivaz and Mooser's equations will thus increase with increasing defect density.

It has already been stated (7.1.2) that interpretation in terms of the model of Fivaz and Mooser leads to large phonon energies associated with small overlap. The latter is not inconsistent with the defect hypothesis, because the presence of interstitial atoms (or ions), or alternatively the displacement of layers occuring in the polytypes, is most likely to lead to a decrease in overlap between conducting states in successive layers.

7.1.4 The Low Temperature Transport Region.

It has not been possible to arrive at any detailed interpretation of the low temperature transport region. Three tentative suggestions will be put forward: neutral impurity scattering, a trap controlled mechanism and a double valence band interpretation. The essentially temperature-independent region shown in figs. 6.3, 6.4 and 6.7 is at first sight suggestive of neutral impurity scattering (Erginsoy, 1950), and therefore the possibility of its application to the present results has been considered. However, the following two points recommend its rejection: (i) In the region just below room temperature where many specimens show a turnover, the vast majority

of impurities will be ionised. Thus the only real evidence for neutral impurity scattering would have to come at very much lower temperatures than those used in the experiments. (ii) The two scattering mechanisms i.e. neutral impurity scattering and optical scattering characterised by μ_{NI} and μ_o respectively, would lead to a resultant mobility of $\frac{1}{\mu} = \frac{1}{\mu_{NI}} + \frac{1}{\mu_o}$.
It is difficult to interpret the sharp turnover observed by a combination of these two scattering mechanisms.

The second alternative, that of a trap-controlled mechanism, is suggested by the activation energy of about 30 - 40 meV observed with certain specimens in the low temperature region (notably figs. 6.3 and 6.8). This would usually be interpreted in terms of a shallow trap lying above the top of the valence band. But because this energy approximates to the splitting at the top of the valence band (section 3.3.4) a third alternative model is suggested. According to this, the low temperature behaviour is due to the promotion of holes between the upper two valence bands, in a similar fashion to the model proposed by Spear and Mort (1963) for holes in CdS. If n_u is the density of free holes present in the upper band and n_l the density in the lower band then, provided Maxwell-Boltzman statistics are applicable,

$$\frac{n_u}{n_l} = \frac{N_u}{N_l} \exp \Delta E/kT$$

where N_u = effective density of states in the upper band

N_l = effective density of states in the lower band

and E = energy separation of the bands.

This equation shows that, as the temperature is lowered, more holes will populate the upper band than the lower one in thermal equilibrium. Since the observed mobility in this region was found to decrease with decreasing temperature, the mobility μ_u in the upper band must be appreciably smaller than the mobility μ_l in the lower one, as is the case in CdS.

In the present work, however, the region of decreasing μ with decreasing T was only observed in a minority of specimens (although a 'dip' was observed in several specimens e.g. P34, fig. 6.3). This prevents the interband interpretation from being regarded as anything more than a possibility at this stage.

7.2 Conductivity Measurements as a Function of Temperature.

The activation energy of 0.26eV found in the dark conductivity measurements (fig. 6.13) is interpreted in terms of the release of charge carriers from traps, and signifies a trapping level at about 0.26eV above the valence band. The same conclusion has been reached by Dugan and Henisch (1967a) from similar measurements (section 3.3.2).

However, when fitted with one indium and one gold electrode and with the field direction from indium to gold, an activation energy of 0.55eV was determined. It has been proposed in the preceding chapter that under these conditions it is possible that only electrons are replenished through the gold electrode, when the carriers are extracted. If this model is correct then the activation energy measured under these conditions refers to a fairly deep electron trap, 0.55eV below the conduction band. It will be seen in section 7.4 that the presence of such a level is supported by the photoluminescence spectra of Dugan and Henisch (1968).

It has been found in all the measurements that at higher temperatures the dark current is controlled by a mechanism with an activation energy of 1.3eV. The transition point varies between 400°K and 450°K, and this alone suggests considerable differences between platelets cleaved from the same boule. An interesting point is the absence of an intermediate region with an activation energy of 0.42eV, as was observed by Dawood and Forty (1962) in a direction perpendicular to the c-axis (fig. 3.5). It was interpreted in terms of the movement of anion defects. The present results show that these defects do not contribute to conductivity along the c-axis, although they may still contribute to diffusion in this direction.

The high temperature region can only be interpreted in a similar fashion to Dawood and Forty (1962) and to Mott and Gurney (1940) in terms of the creation and movement of interstitial Pb^{2+} ions. The fact that the transition temperature is higher for conduction perpendicular to the c-axis than parallel to it is consistent with the much higher hole mobility to be expected along the layers. The conductivity due to this carrier will therefore predominate until higher temperatures, all other factors being equal.

7.3 The Photoconductive Response.

The peak in the photoresponse of boule B around the absorption edge (fig. 6.17) could be explained in terms of surface recombination. In contrast to this, the peak centred around 3.3eV in this boule can only correspond to a genuine absorption effect, and is probably due to a transition from the lowest valence band. It will be discussed further in the following section. The effect of heat treatment on the photoconductive response of boule B, fig. 6.19, shows the almost complete removal of the 2.4eV peak, an increase in photosensitivity and an apparent shift of the absorption edge to higher energies. The first two can be explained by the annealing process, which removes defects and hence increases both the bulk and surface lifetimes. However, since this is not a true

absorption measurement the results do not provide conclusive proof for a shift of the 'absorption edge'.

The photoconductive response of boule A, fig. 6.20, differs quite markedly from that of boule B. The absence of the peak around the absorption edge implies that there is little difference between the bulk and surface lifetimes. This may help to account for the fact that transits were observed in boule A, but not in boule B. No peak is observed at 3.3eV in boule A, possibly suggesting this transition in boule B to be associated with a defect level.

7.4 A Band Structure Model.

A band structure model is proposed, based on that of Dugan and Henisch (1968), fig. 3.13, but with a modification and additions. It is given in fig. 7.5a. The lower sub-band A is placed 0.54eV below the top of the valence band B. The defect levels at 0.26eV (C) and 0.46eV (D) above B are retained, but not so the arbitrarily introduced level 0.1eV below the conduction band. Instead, a level E is placed 0.55eV below the conduction band F, in accordance with the interpretation of the conductivity data presented earlier (7.2). The band gap is kept at 2.41eV. A new level G, associated either with a higher conduction band or with defects, is suggested to lie 0.36eV

above the bottom of the first conduction band.

This model would appear to give a more satisfactory explanation of the transitions reported by Dugan and Henisch (1968), described in section 3.3.6. The transitions are shown in fig. 7.5b, with the experimental values of Dugan and Henisch given in parentheses. The omission of the 2.31eV peak in the photoconductive response of Dugan and Henisch is explained by this model (a transition between defect levels) and it is also clear why a peak was never observed corresponding to a 2.06eV transition, as required by the model of Dugan and Henisch. The present model, however, predicts a feature in both the photoconductive response and photoluminescence spectra at 1.86eV, whereas Dugan and Henisch observed this transition in only the latter. It is tentatively suggested that the peak attributed to a 1.99eV transition in their photoconductive response has perhaps been misinterpreted and in fact corresponds to a 1.85eV transition. This is borne out by a closer examination of fig.3.10a. The 1.99eV transition would then be absent in the photoconductive response and this would be expected from the present model, for it corresponds to a transition from defect level D.

The introduction of level G, to account for the 2.31eV transition, is supported by the fact that it predicts a 3.3eV transition between G and the lowest

valence sub-band A. Since the latter transition was observed only in boule B of the present investigation, it would appear probable that it is associated with a defect level. This explanation of the 2.31eV transition requires that it is observed only in the photoluminescence spectra, which is indeed the case. The present interpretation seems therefore preferable to that of Dugan and Henisch. It is evident that the proposed model is consistent with a wider range of observed features and represents therefore a marked improvement on previously suggested band models.

7.5 Conclusions.

(i) Hole mobilities lie between 1.8$cm^2volt^{-1}sec^{-1}$ and 5$cm^2volt^{-1}sec^{-1}$ at room temperature. The results show that, contrary to expectations, the hole transport proceeds in a narrow band and that the mobility is determined by optical scattering.

(ii) Two possible interpretations of the transport results in the temperature region above 250°K have been explored and it is found that the model of Fivaz and Mooser leads to a better agreement with the results than the small polaron theory.

(iii) The variations in the optical phonon energies, overlap energies (or polaron binding energies) between specimens are attributed to large, but differing,

defect densities brought about by some or a combination of the reasons put forward in section 7.1.3.

(iv) The low temperature transport results are not readily interpreted, but several possibilities have been outlined. It would appear that neutral impurity scattering is unlikely; more experimental work is necessary before it can be decided whether the trap controlled or interband transition mechanisms are applicable.

(v) Dark conductivity measurements have confirmed a trapping level 0.26eV above the valence band and indicate the presence of an electron trap 0.55eV below the conduction band.

(vi) Using the above results and the data of other authors, notably Dugan and Henisch (1968), the energy level diagram shown in fig. 7.5 is proposed. It provides a more consistent explanation of many often reported transitions in PbI_2.

Appendix. (see p.72)

Equation 7.3 showed that the mobility perpendicular to the layers, according to the theory of Fivaz and Mooser, can be written in the form

$$\mu = A\hbar\omega\beta(\exp(\hbar\omega\beta) - 1)$$

writing $\beta = 1/kT$

Now, the observed gradient ϵ of the experimental plots of $\log\mu$ v. $1/T$ is given by

$$\epsilon = \frac{d\log\mu}{d(1/kT)} = \frac{d\log\mu}{d\mu} \cdot \frac{d\mu}{d\beta} = \frac{1}{\mu} \cdot \frac{d\mu}{d\beta}$$

Differentiating the above expression for μ,

$$\frac{d\mu}{d\beta} = \hbar\omega A\beta(\hbar\omega \exp\hbar\omega\beta) + (\exp(\hbar\omega\beta) - 1)\hbar\omega A$$

$$= A\beta(\hbar\omega)^2 \exp\hbar\omega\beta + \frac{\mu}{\beta}$$

$$\therefore \epsilon = \frac{1}{\mu} \cdot \frac{d\mu}{d\beta} = \frac{1}{\beta} + \frac{\hbar\omega(\mu + A\beta\omega)}{\mu}$$

$$= \frac{1}{\beta} + \hbar\omega + \frac{A}{\mu}\beta(\hbar\omega)^2$$

$$\therefore \epsilon = kT + \hbar\omega + \frac{\hbar\omega}{\exp(\hbar\omega/kT)-1}$$

and $(Lt\,\epsilon)_{\hbar\omega \to 0} = 2kT$.

REFERENCES

Adams, A. and Spear, W.E., 1964, J. Phys. Chem. Sol., 25,1113.

Austin, Springthorpe, Smith and Turner, 1967, Proc. Phys. Soc., 90,567.

Bassani, F., Greenaway, D.L. and Fischer, G., 1964, Proc. Int. Conf. Phys. Semicond., Paris, p.51.

Bassani, F. and Pastori, G., 1967, Il Nuovo Cimento, 50B,95.

Birman, J.L., 1959, Phys. Rev. Lett., 2,157.

Brahms, S., 1965, Phys. Lett., 19,272.

Brebner, J.L. and Fischer, G., 1962a, J. Phys. Chem. Sol., 23,1363.

Brebner, J.L. and Fischer, G., 1962b, Proc. Int. Phys. Semicond., Exeter, p. 760.

Brebner, J.L., Fischer, G. and Mooser, E., 1962, J. Phys. Chem. Sol., 23,1417.

Brebner, J.L. and Mooser, E., 1967, Phys. Letts., 24A,274.

Bube, R.H. and Lind, E.L., 1960, Phys. Rev., 119,1535.

Dawood, R.I. and Forty, A.J., 1962, Phil. Mag., 7,1633.

Dawood, R.I., Forty, A.J. and Tubbs, M.R., 1965, Proc. Roy. Soc., 284A,272.

Dennis, J. and Henisch, H.K., 1967, J. Electrochem. Soc., 114,263.

Dudkin, L.D. and Vaidanich, V.I., 1961, Voprosy Met. i. Fiz. Poluprovod. AK. Nauk. SSSR. Trudy i. Seveschchaiya, Moscov, p. 113-22.

Dugan, A.E. and Henisch, H.K., 1967a, J. Phys. Chem. Sol., 28,1885.

Dugan, A.E. and Henisch, H.K., 1967b, J. Phys. Chem. Sol., 28,971.

Dugan, A.E. and Henisch, H.K., 1968, Phys. Rev., 171,1047.

Elliot, R.J., 1957, Phys. Rev., 108,1384.

Erginsoy, C., 1950, Phys. Rev., 79,1013.

Eucken, A. and Buchner, E., 1934, Z. Phys. Chem., 27B,321.

Fielding, P., Fischer, G. and Mooser, E., 1959, J. Phys. Chem. Sol., 8,434.

Fischer, G., 1963, Helv. Phys. Acta, 36,317.

Fivaz, R. and Mooser, E., 1964, Phys. Rev., 136A,833.

Forty, A.J., 1960, Phil. Mag., 5,787.

Forty, A.J., 1961, Phil. Mag., 6,895.

Frȍhlich, H. and Sewell, G.L., 1959, Proc. Phys. Soc. (London), 74,643.

Gasanova, N.A., Akhundov, G.A. and Nizametdinova, M.A., 1966, Phys. Stat. Solidi, 17,K115.

Greenaway, D.L. and Harbeke, G., 1965, Conf. Solid State Phys. (Bristol).

Greenaway, D.L. and Harbeke, G., 1966, Proc. Int. Conf. Phys. Semicond. (Kyoto), p. 151.

Greenaway, D.L. and Nitsche, R., 1965, J. Phys. Chem. Sol., 26,1445.

Haken H., 1957, Halbleiterprobleme,edited by W. Schottky (Braunschweig, Vieweg),4.

Henisch, H.K., Dennis, J. and Hanoka, J.L., 1965, J. Phys. Chem. Sol., 86,443.

Henisch, H.K. and Srinivasagopalan, C., 1966, Solid State Comm., 4,415.

Heydweiller, A., 1920, Z. Phys., 3,308.

Hilsch, R. and Pohl, P.W., 1928, Z. Phys., 48,384.

Holstein, T., 1959, Annals of Physics, 8,325.

Hulliger, F., 1960, Helv. Phys. Acta, 33,959.

Imai, I., 1961, J. Phys. Chem. Sol., 22,81.

Imai, I. and Ishiguro, K., 1959, Suppl. Prog. Theor. Phys., 12,174.

Jacobs, P.W.M. and Tompkins, F.C., 1952, Proc. Roy. Soc., 215A,254.

Kamimura, H. and Nakao, K., 1966, Proc. Int. Conf. Phys. Semicond. (Kyoto). p. 27.

Klein, C.A., 1968, J. Appl. Phys., 39,2029.

McTaggart, F.K., 1958, Astral. J. Chem., 11,471.

Mott, N.F. and Gurney, R.W., 1940, Electronic Processes in Ionic Crystals (Oxford Univ. Press).

Nikitine, S., 1955, C.R. Acad. Sci. Paris, 240.64.

Nikitine, S., Schmitt-Burkel, J., Biellman, J. and

Ringeissen, J., 1964, J. Phys. Chem. Sol., 25,951.

Parsons, R.B., Wardzynski, W. and Yoffe, A.D., 1961, Proc. Roy. Soc., A262,120.

Ralph, H.I., 1965, Solid State Comm., 3,303.

Ryvkin, S.M. and Khansevarov, R.I., 1956, Zh. Tekh. Fiz., 26,2781.

Schaefer, H., 1962, Chemische Transportreaktionen, (Weinheim).

Seith, W., 1929, Z. Phys., 57,869.

Shockley, W., 1961, Solid State Electronics, 2,35.

Spear, W.E., 1960, Proc. Phys. Soc., 76,826.

Spear, W.E., Adams, A. and Henderson, G., 1963, J. Sci. Instrum., 40,332.

Spear, W.E., Lanyon, H.P.D. and Mort, J., 1962, J. Sci. Instrum., 39,81.

Spear, W.E. and Mort, J., 1963, Proc. Phys. Soc., 81,130.

Toyozawa, Y., 1962, Polarons and Excitons (Oliver and Boyd), p. 211.

Tubbs, M.R., 1964, Proc. Roy. Soc., 280A,566.

Tubbs, M.R., 1966, J. Phys. Chem. Sol., 27,1667.

Tubbs, M.R. and Forty, A.J., 1965, J. Phys. Chem. Sol., 26,711.

Yamashita, J. and Kurosawa, T., 1958, J. Phys. Chem. Sol., 5,34.

Fig. 2.1

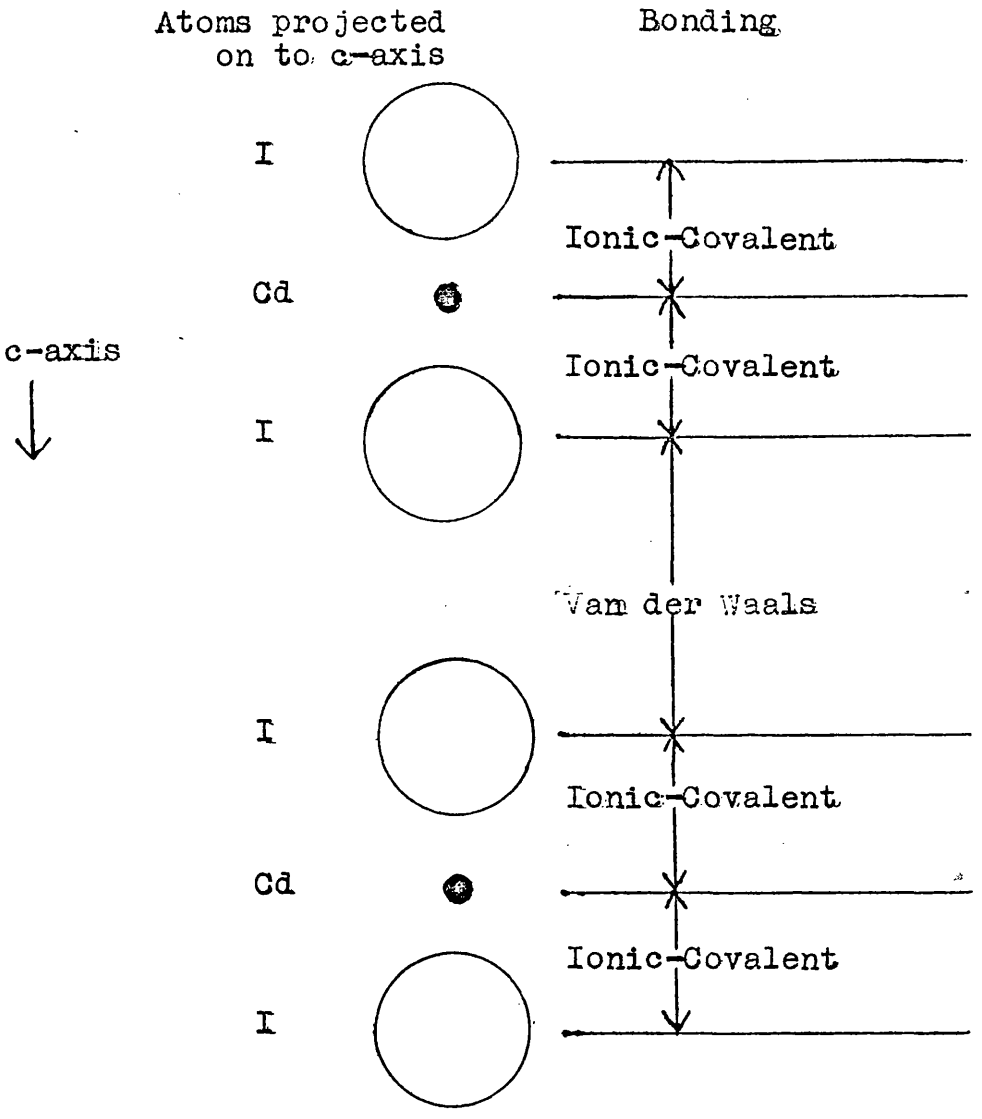

Fig. 2.1 Schematic Representation of the Bonding in the Layer Compound CdI_2.

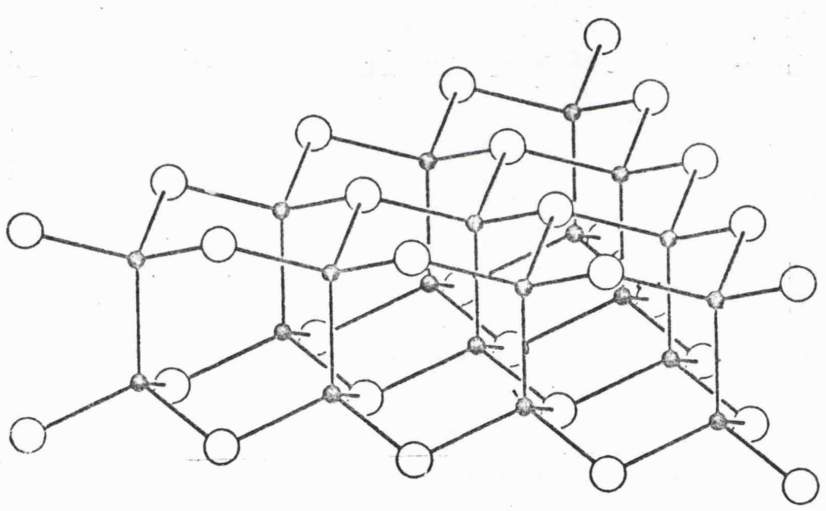

Fig. 2.2 Structure of one of the four-fold Layers of GaS and GaSe; ● Ga atoms, ○ S or Se atoms.

Fig. 3.1

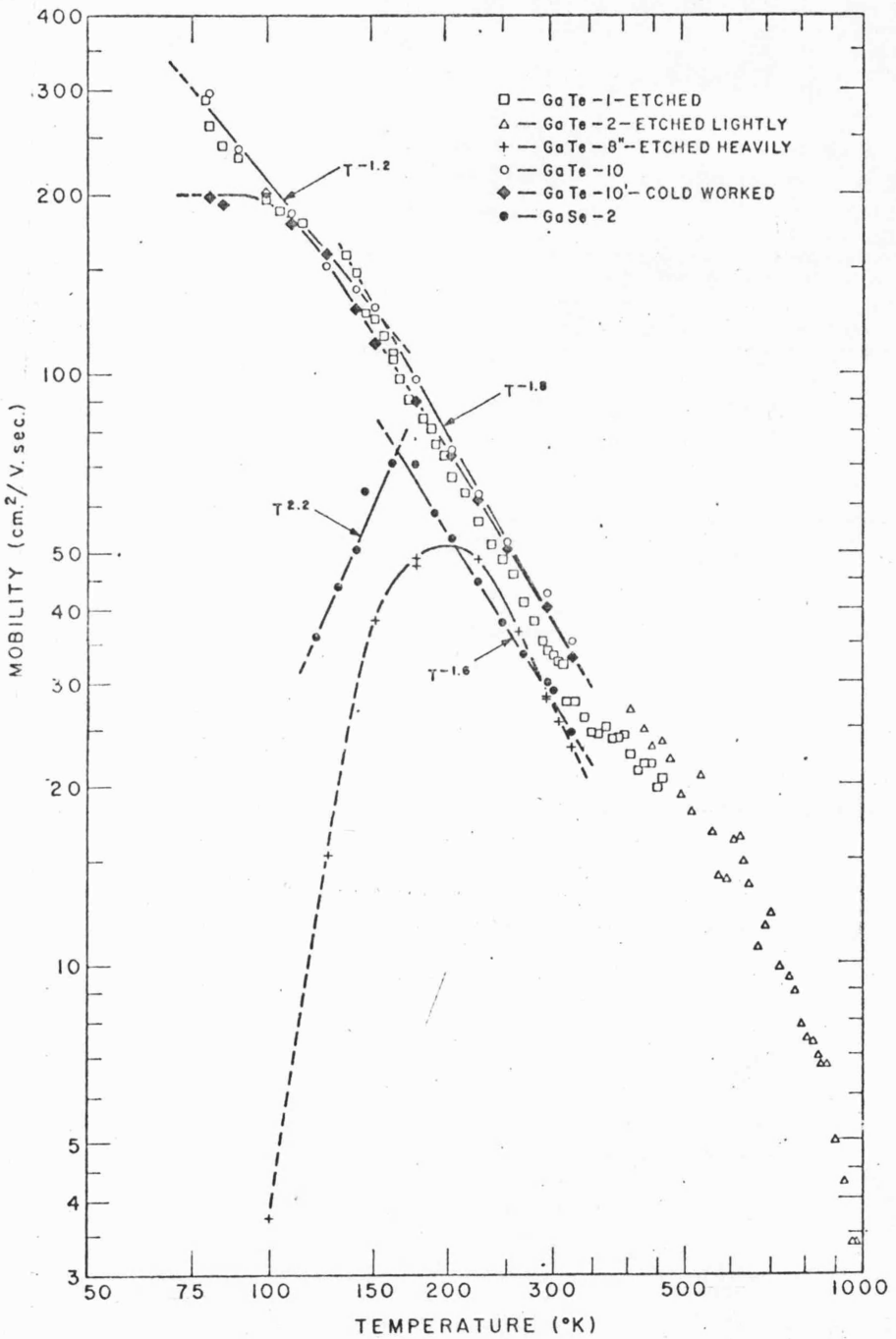

Fig. 3.1 Hall Mobility of Holes against Temperature for various samples of GaTe and GaSe (after Fischer and Brebner, 1962a).

Figs. 3.2, 3.3a and b.

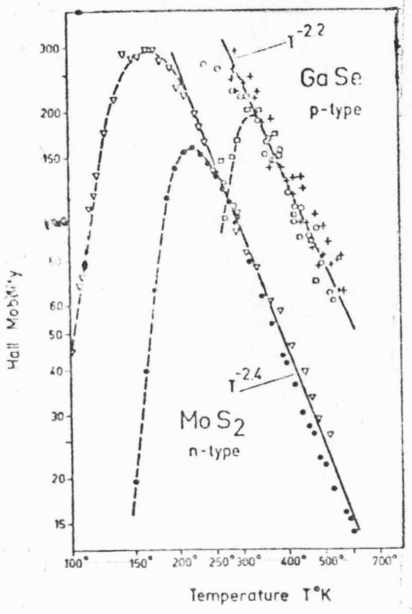

Fig. 3.2 Hall Mobilities of the Charge Carriers in Monocrystalline GaSe and MoS_2 (after Fivaz and Mooser, 1964).

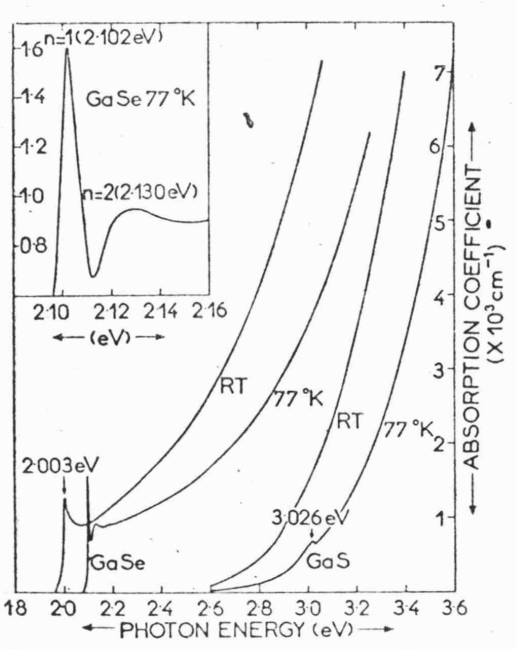

Absorption curves of GaS and GaSe at room temperature and 77 °K.

Fig. 3.3a

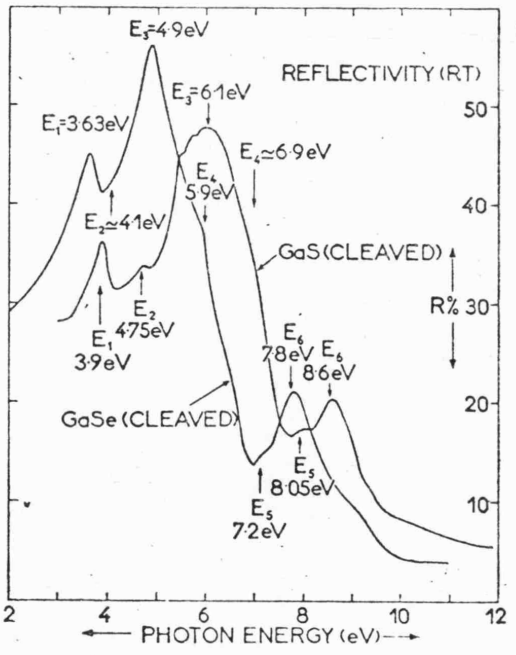

Reflectivity of cleaved GaS and GaSe at room temperature.

Fig. 3.3b

(after Bassani, Greenaway and Fischer, 1964)

Figs. 3.4a and b.

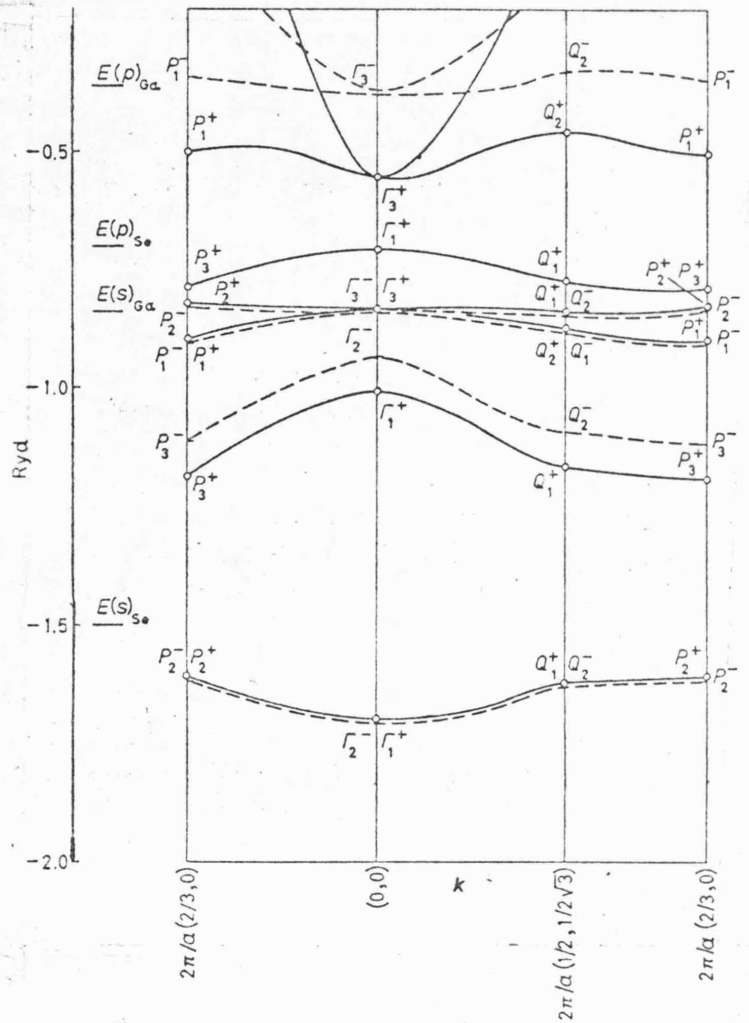

Fig. 3.4a Band Structure of two-dimensional GaSe.

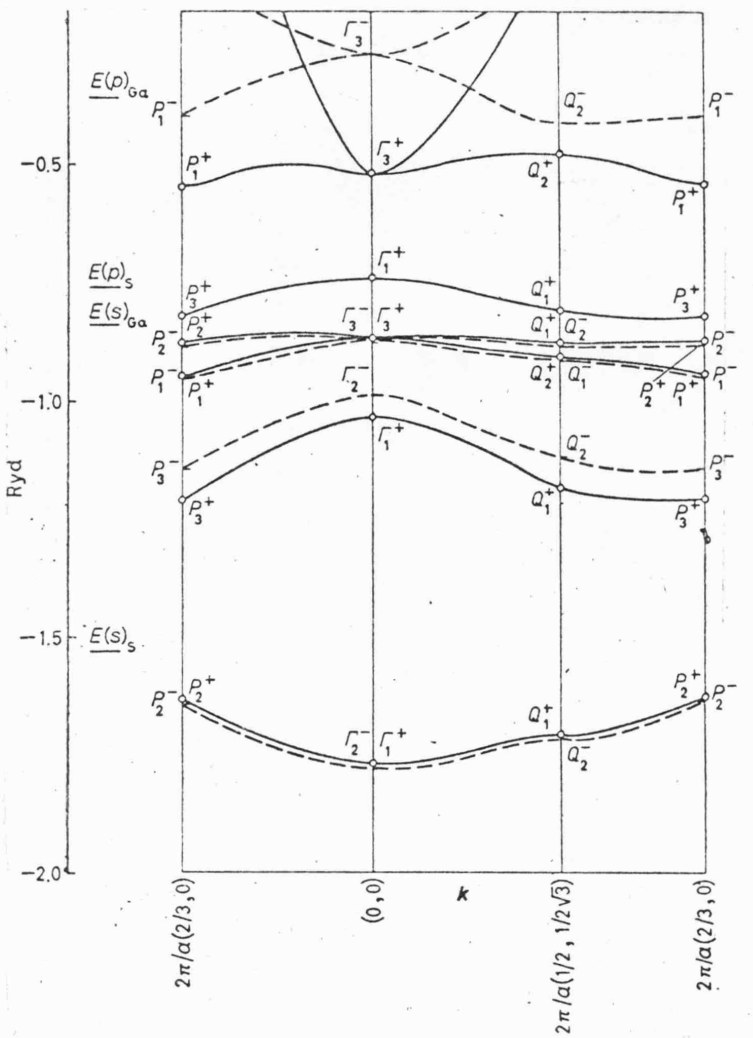

Fig. 3.4b Band Structure of two-dimensional GaS.

(after Bassani and Pastori, 1967)

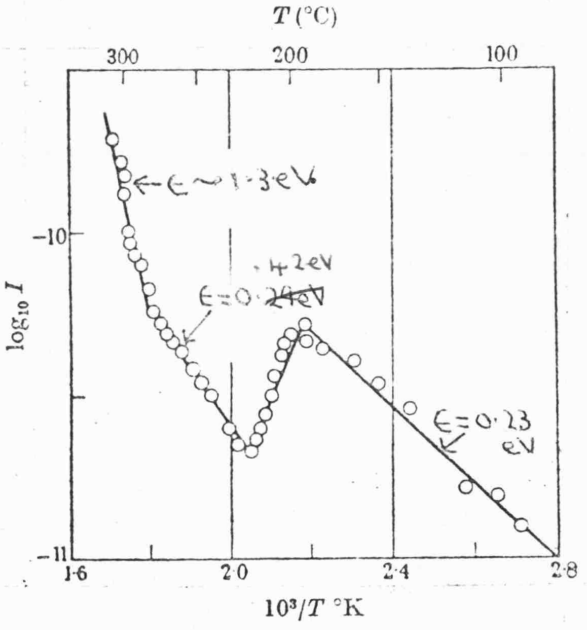

Fig. 3.5 The Variation of Electrical Conductivity with Temperature for an Illuminated Crystal of Lead Iodide.
(after Forty and Dawood, 1962)

Figs. 3.6a and b.

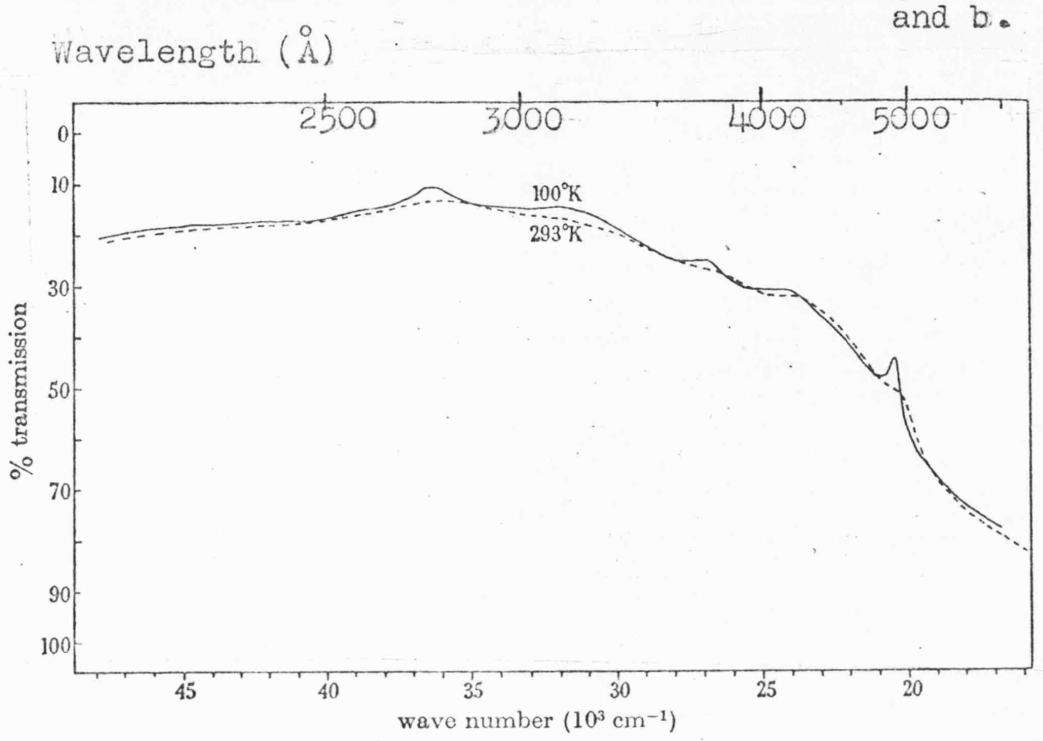

Fig. 3.6a The Transmission Spectra of an Evaporated Film of Lead Iodide at Low Temperatures. (after Tubbs, 1964)

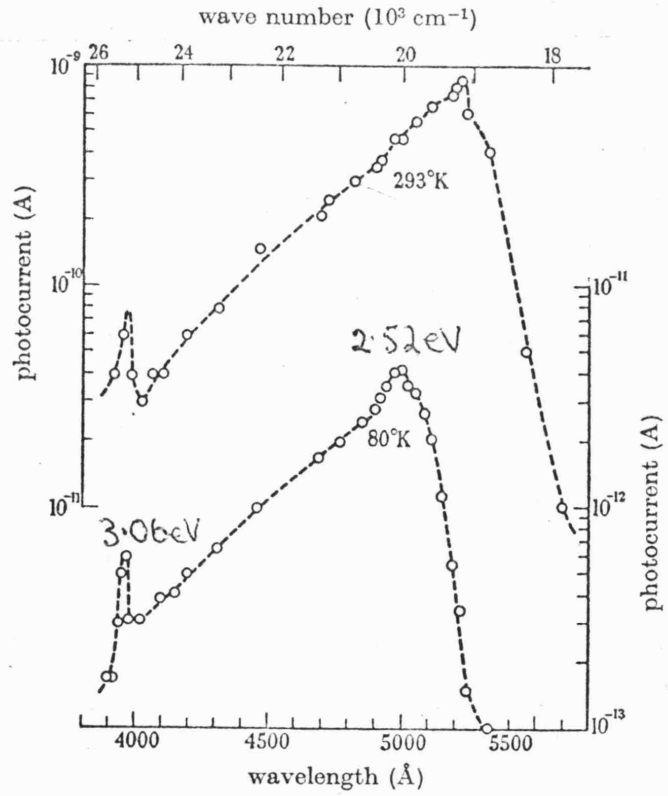

Fig. 3.6b The Spectral Distribution of Photoconductivity for a Single Crystal of Lead Iodide. (after Tubbs, 1964)

Figs. 3.7a and b.

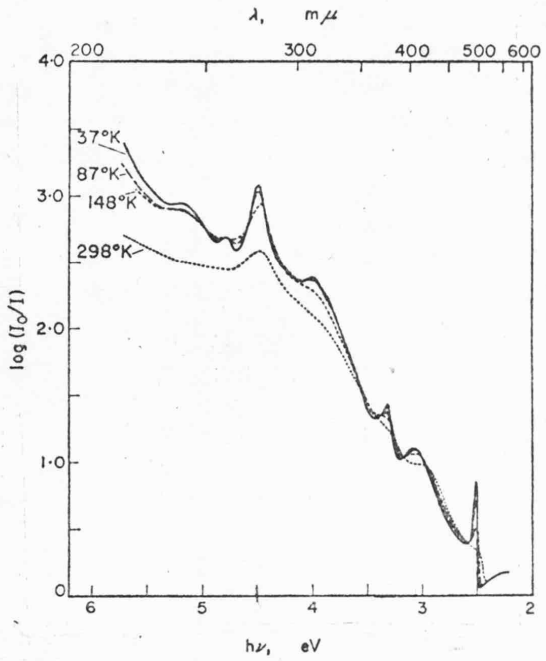

Fig. 3.7a The Optical Absorption Spectrum of PbI_2.

(after Imai, 1961)

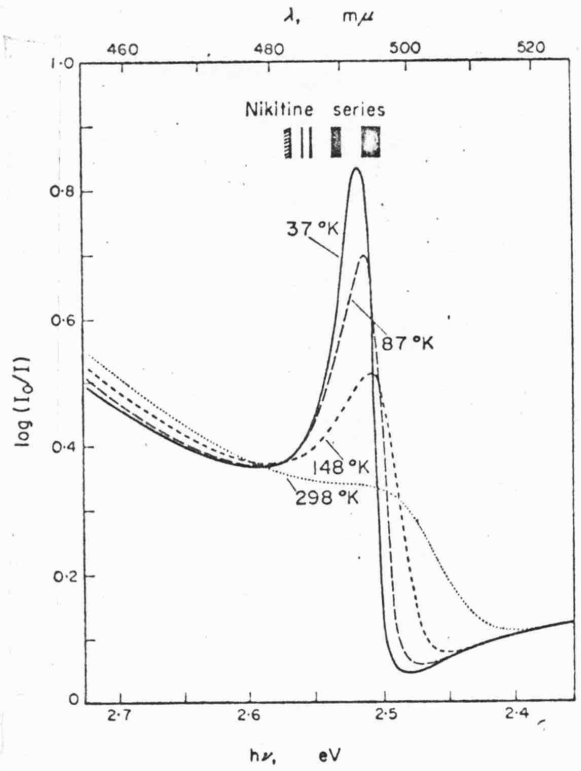

Fig. 3.7b Details of the Curves near the first Band in Fig. 3.7a.

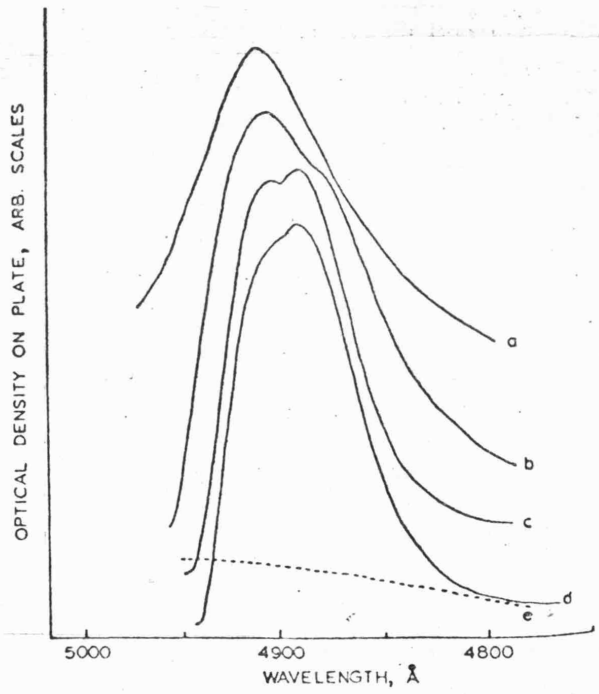

Fig. 3.8 Microdensiometer Traces of Absorption Spectra taken at 4.2°K for Evaporated Films of PbI_2 with Thicknesses of (a) 400Å; (b) 700Å; (c) 2500Å; (d) 2900Å, with Comparison Spectrum (e) (after Tubbs and Forty, 1965)

Figs. 3.9a
and b.

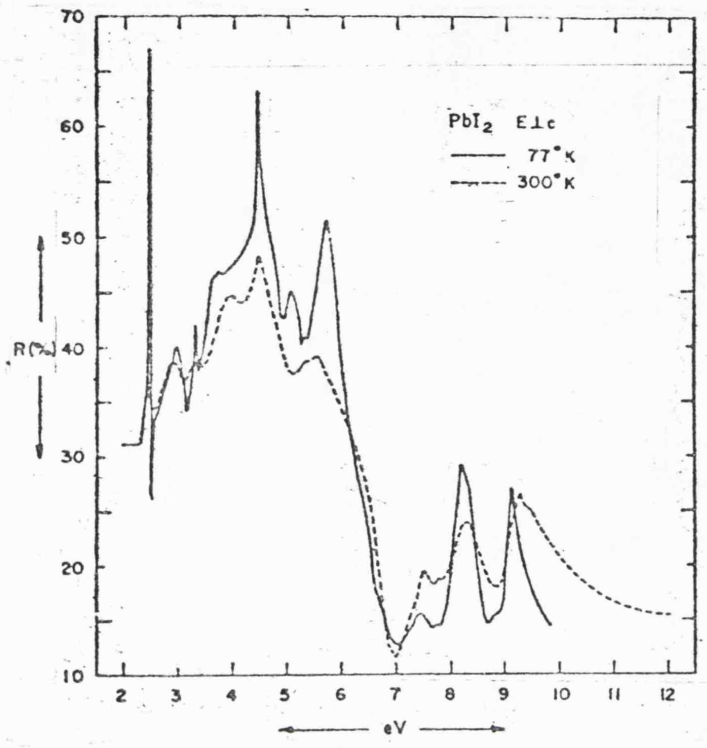

Fig. 3.9a Reflectivity of PbI_2 at 300°K and 77°K, E⊥C.
(after Greenaway and Harbeke, 1966)

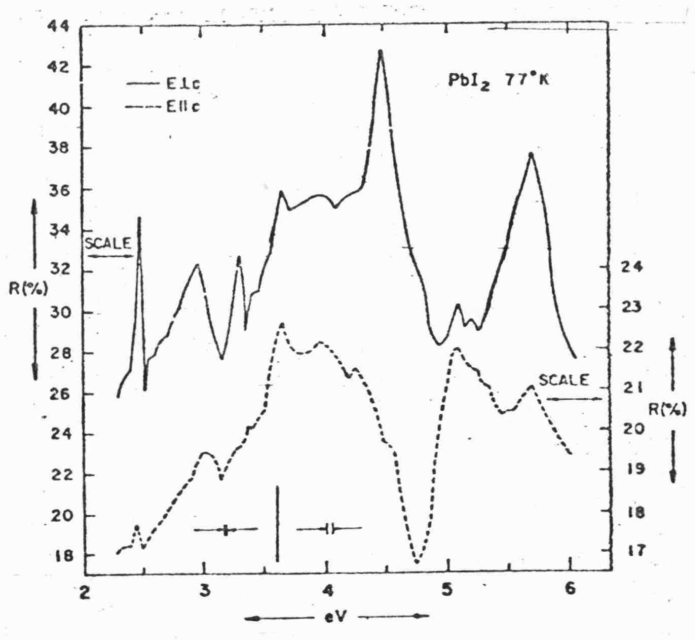

Fig. 3.9b Reflectivity of PbI_2 at 77°K, E∥C and E⊥C.
(after Greenaway and Harbeke, 1966)

Figs. 3.10a and b.

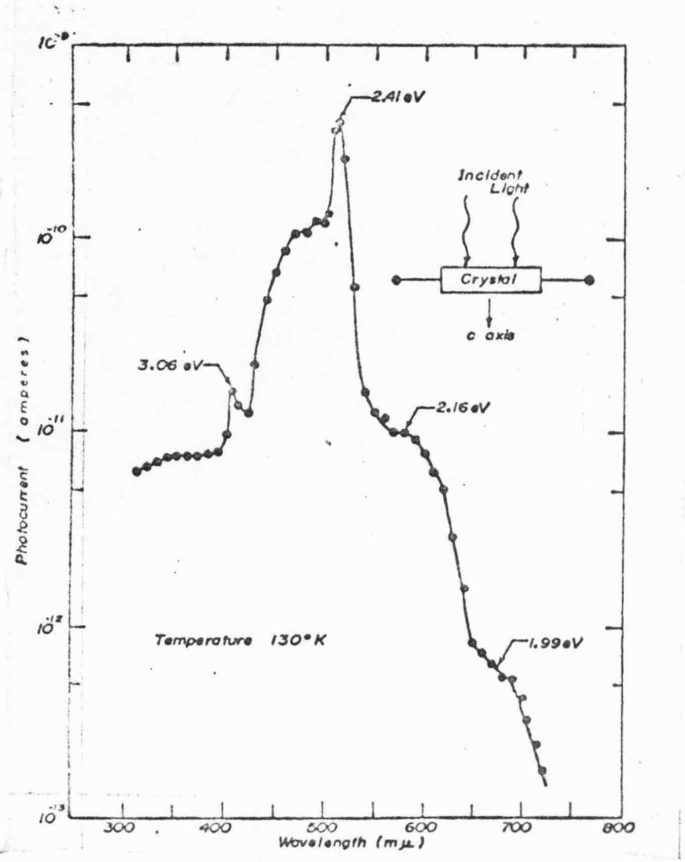

Fig. 3.10a Photoresponse of a PbI_2 Single Crystal.

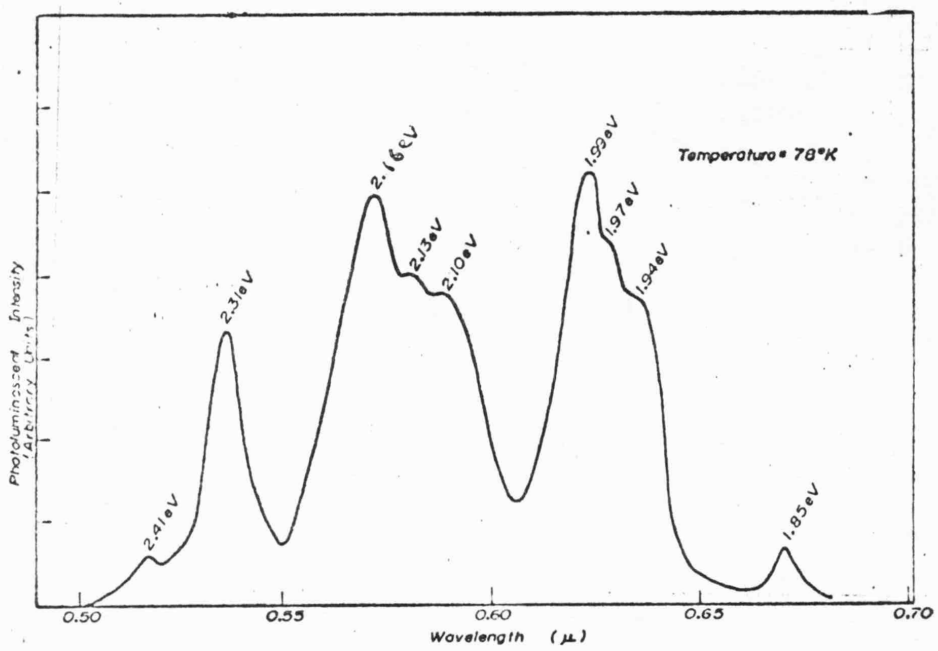

Fig. 3.10b Photoluminescence Spectrum of a PbI_2 Single Crystal.

(after Dugan and Henisch, 1968)

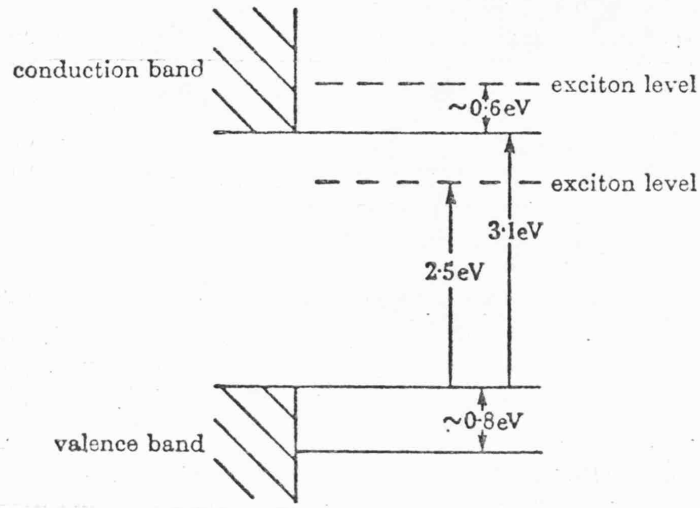

Fig. 3.11 Schematic Diagram of the Electron Energy Bands at k = o in PbI_2.
(after Tubbs, 1964)

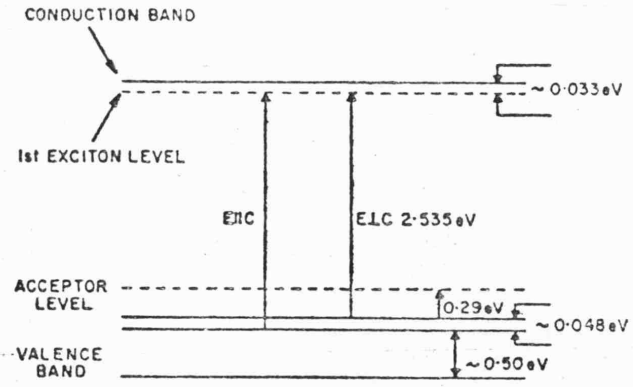

Fig. 3.12 Schematic Optical Energy Level Diagram of PbI_2 at k = o.
(after Dugan and Henisch, 1967a)

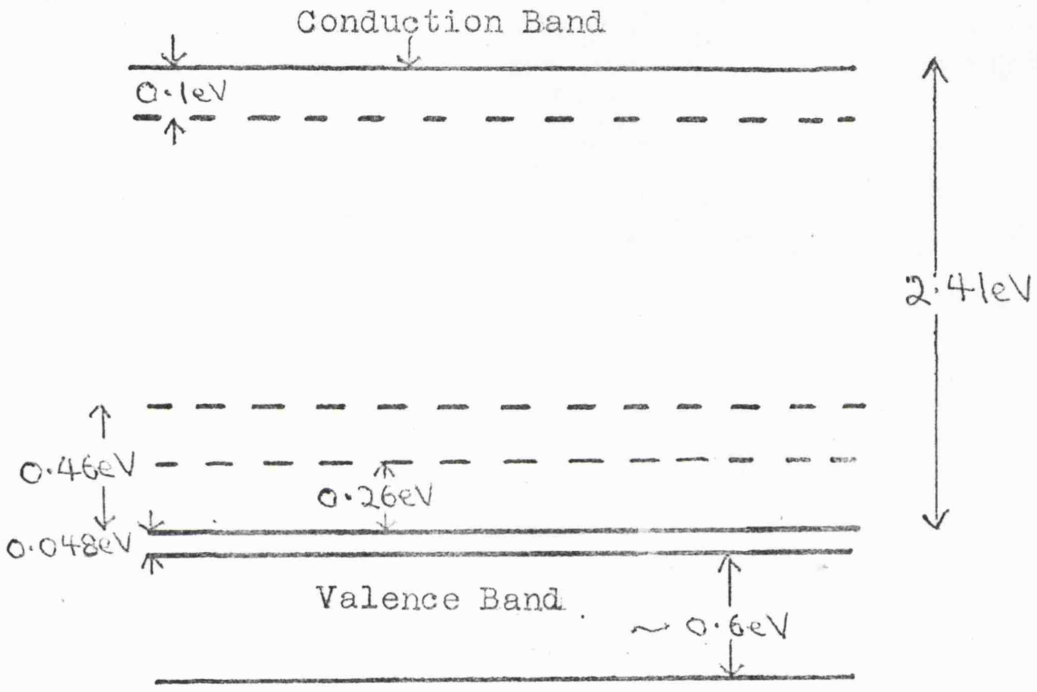

Fig. 3.13 Energy Level Diagram showing Split-Valence Band and Defect Level Structure for Gel-Grown PbI_2 Single Crystals.
(after Dugan and Henisch, 1968)

Fig. 4.1

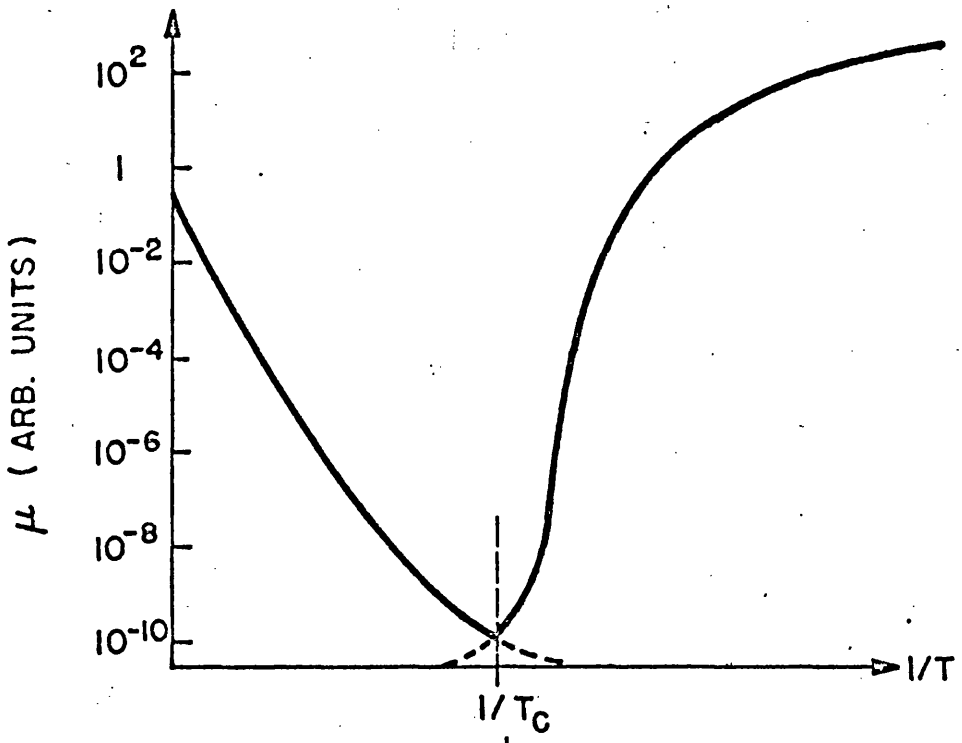

$T > T_C$	$T < T_C$
PHONON ASSISTED HOPPING $\hbar/\tau > W$	SMALL POLARON BAND $\hbar/\tau < W$
NO CORRELATION BETWEEN INITIAL AND FINAL PHONON STATES.	PHONON STATES REMAIN UNCHANGED DURING INTER-MOLECULAR TRANSISTIONS.

Fig. 4.1

Fig. 4.2

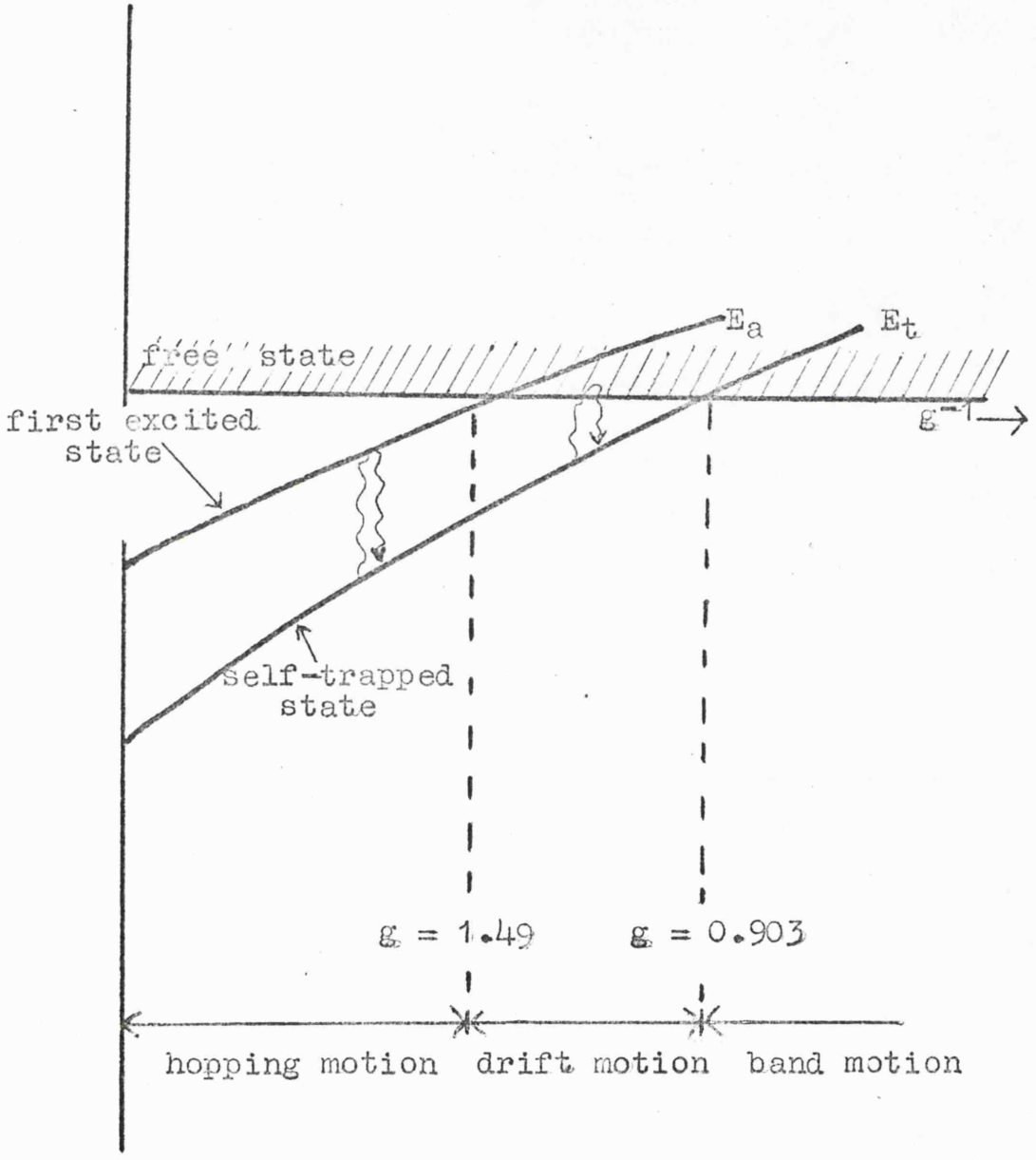

Fig. 4.2 Energies of the Self-Trapped States Relative to that of the Free State according to Toyozawa.

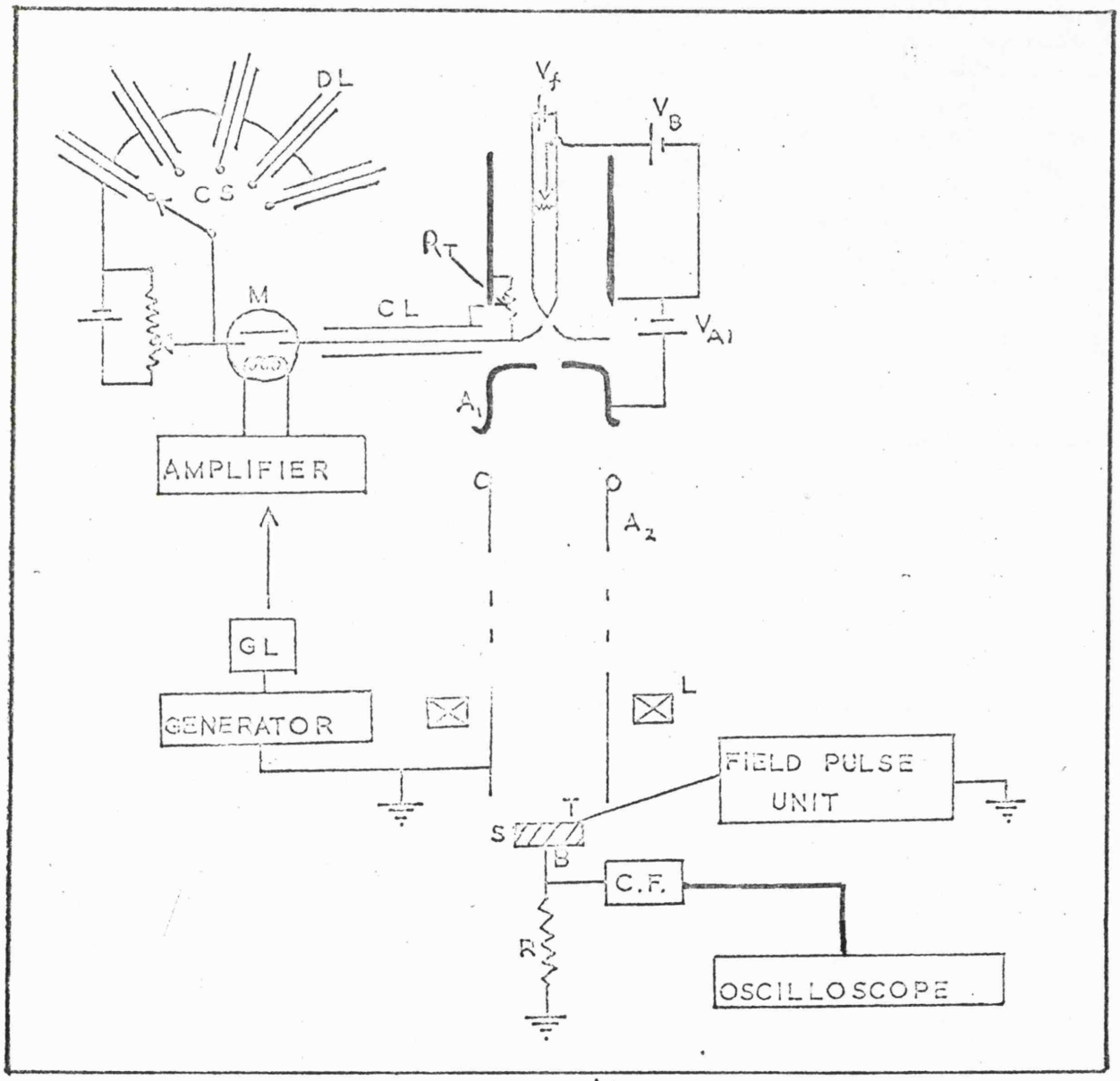

Fig. 5.1 Block Diagram of the Experimental Arrangement for Electron Pulse Excitation.

Fig. 5.2

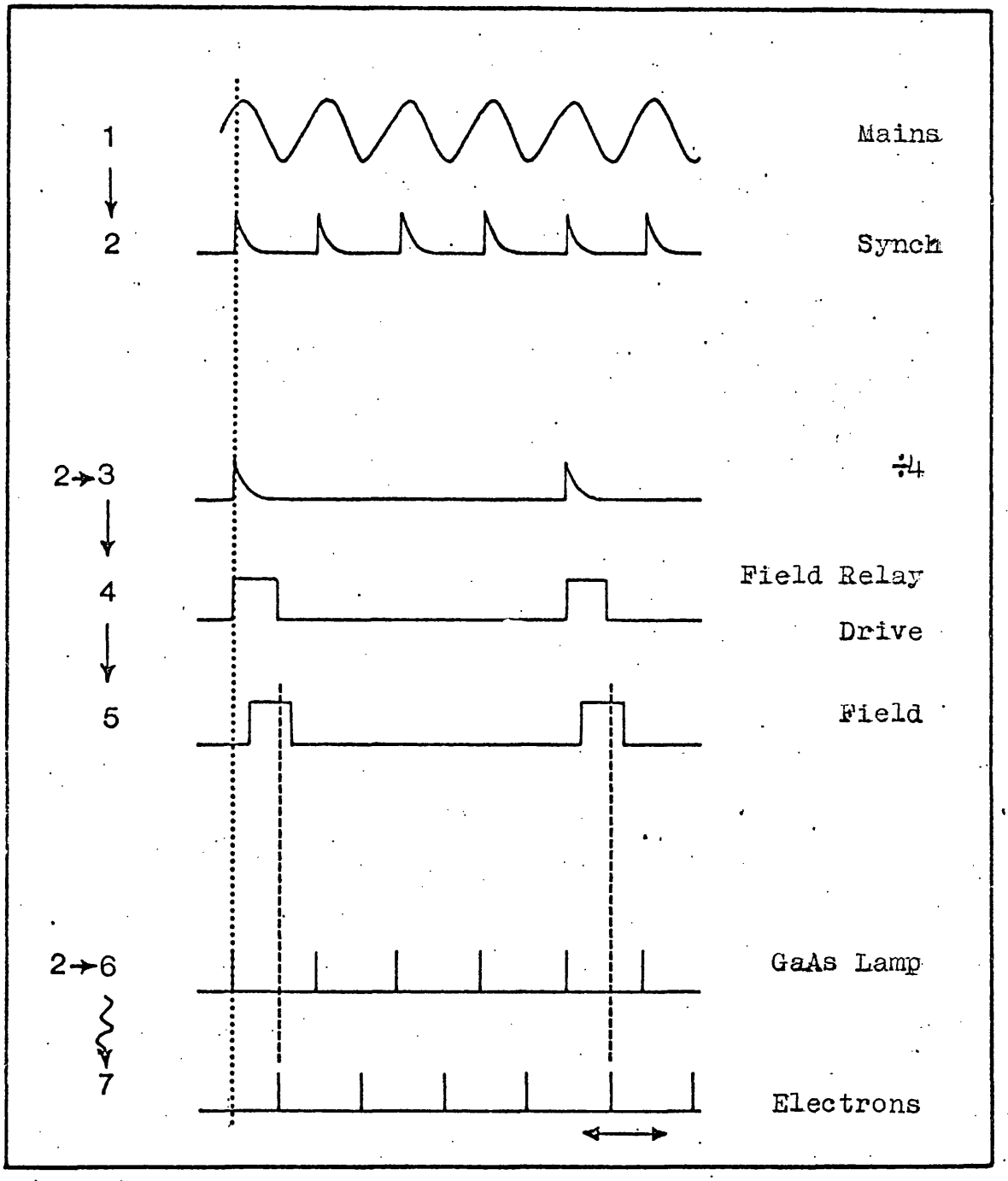

Fig. 5.2 Electron Pulse Synchronisation.

Fig. 5.3

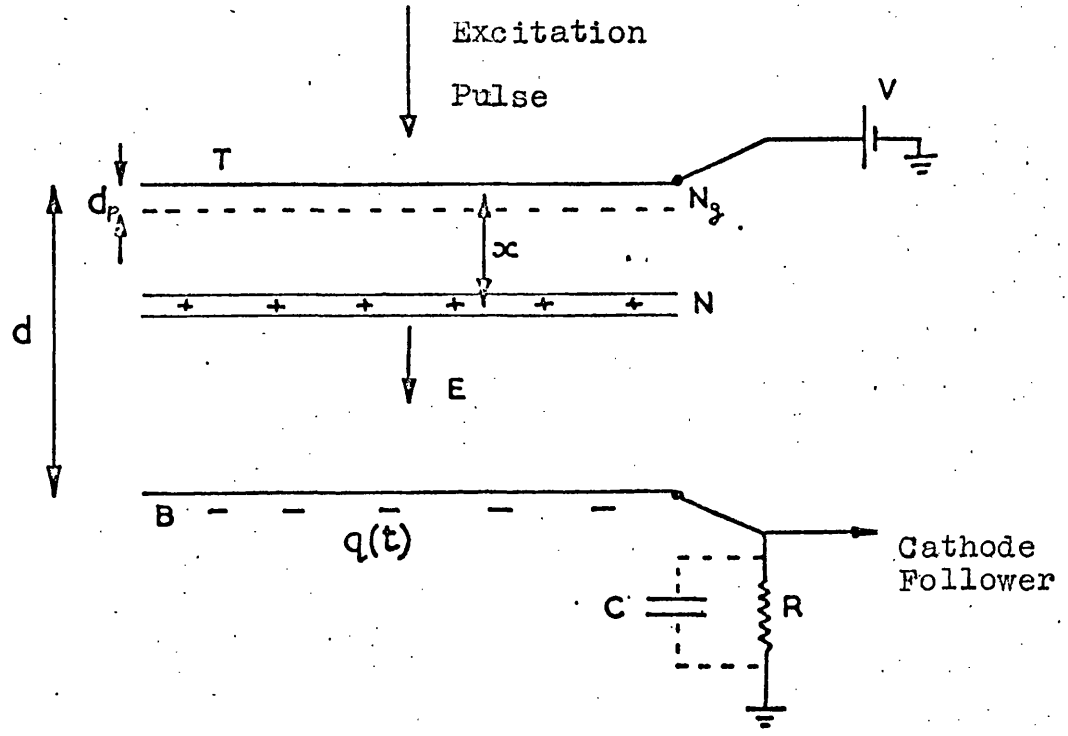

Fig. 5.3 Illustrating the Principle of Charge Integration for Transit Time Measurements.

Figs. 5.4a
and b.

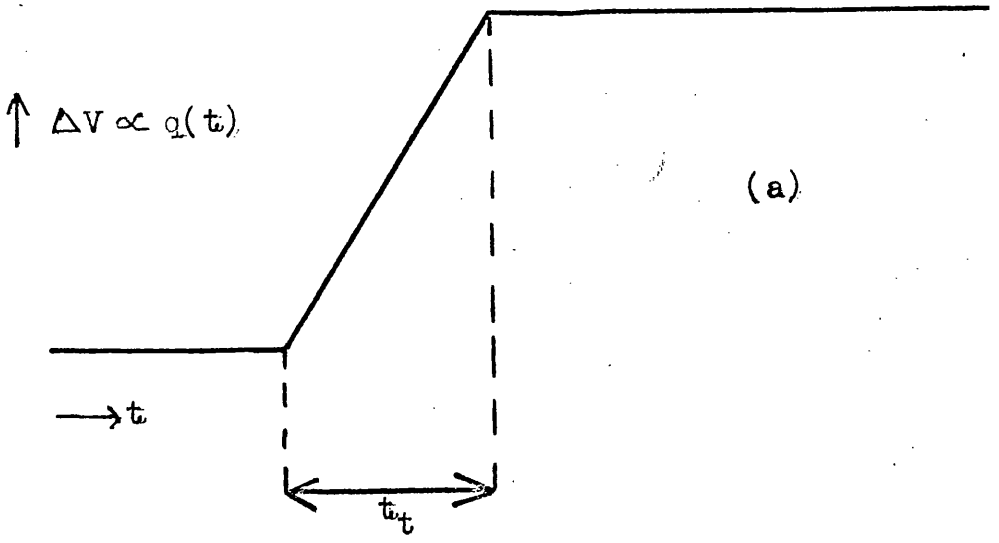

Fig. 5.4a Integrated Signal of Carrier Transit expected under Ideal Conditions.

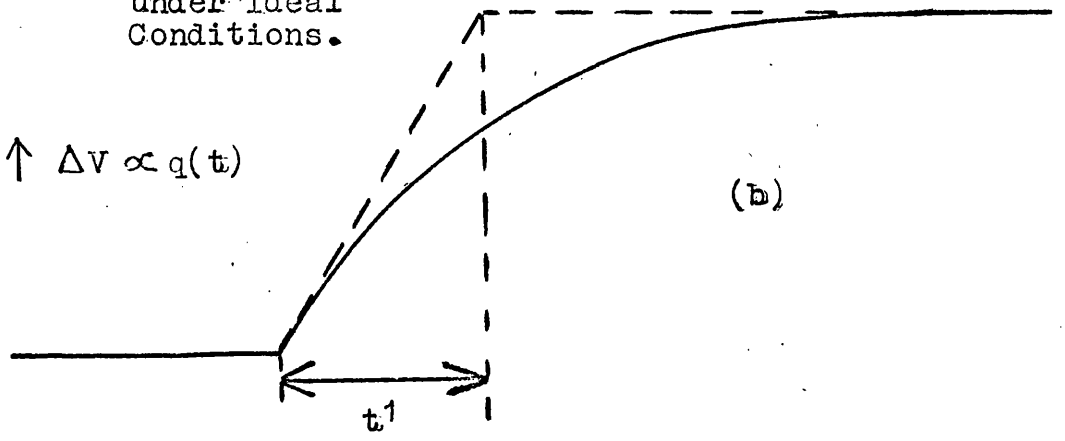

Fig. 5.4b Integrated Signal of Carrier Transit in presence of Deep Traps and/or at Low Applied Fields.

Fig. 5.5

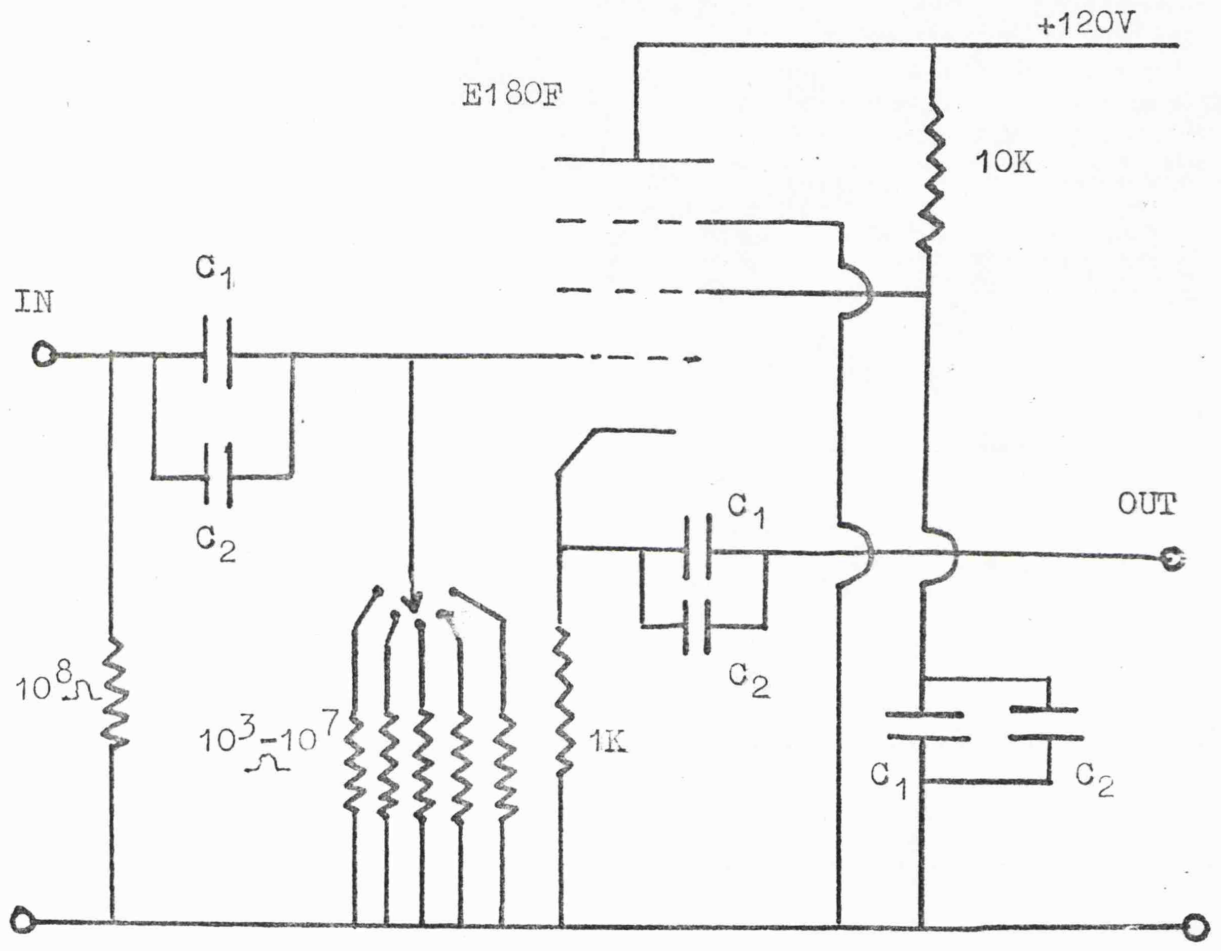

$C_1 = 0.1\mu F$ $C_2 = 0.001\mu F$

Fig. 5.5 Circuit Diagram of Cathode Follower.

Fig. 5.6

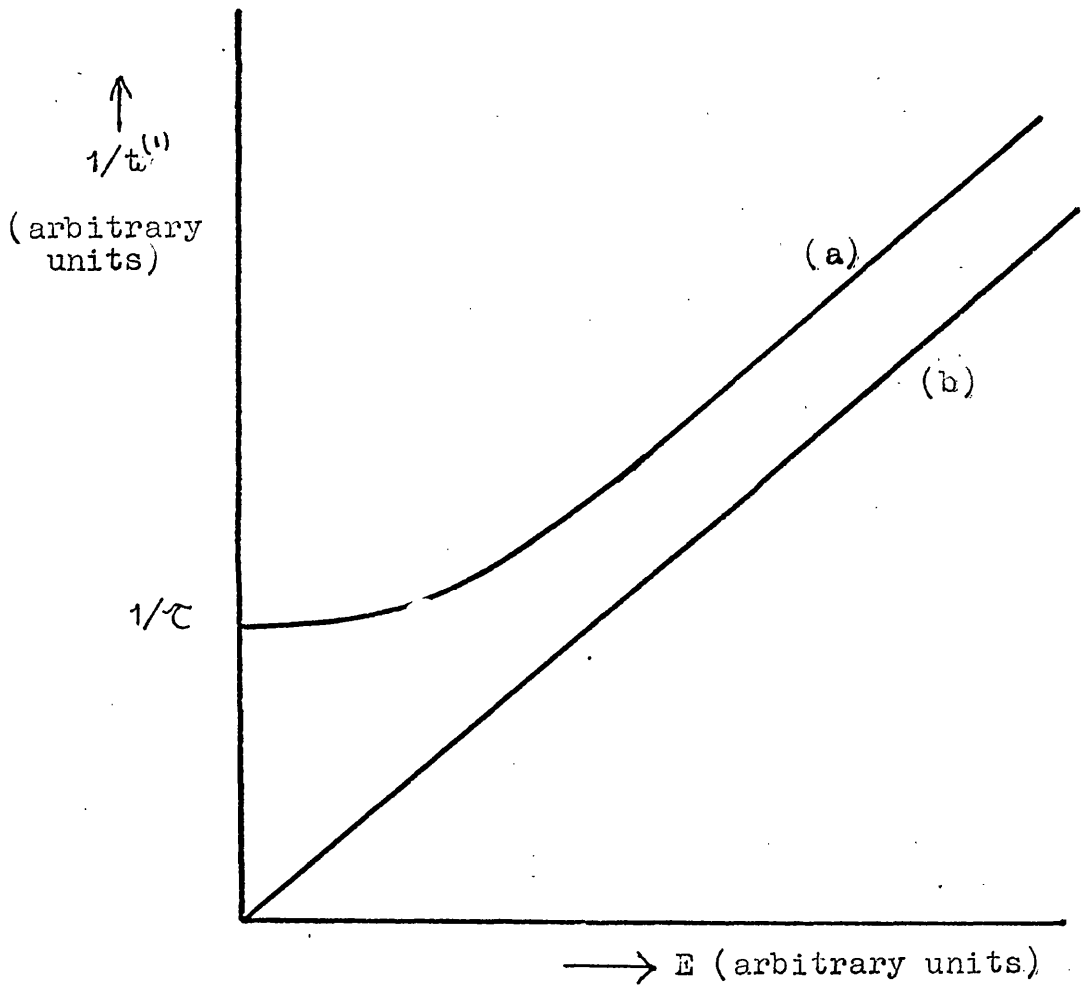

Fig. 5.6 Graphs showing (a) $1/t'$ v. E and (b) $1/t_t$ v. E i.e. corrected for lifetime.

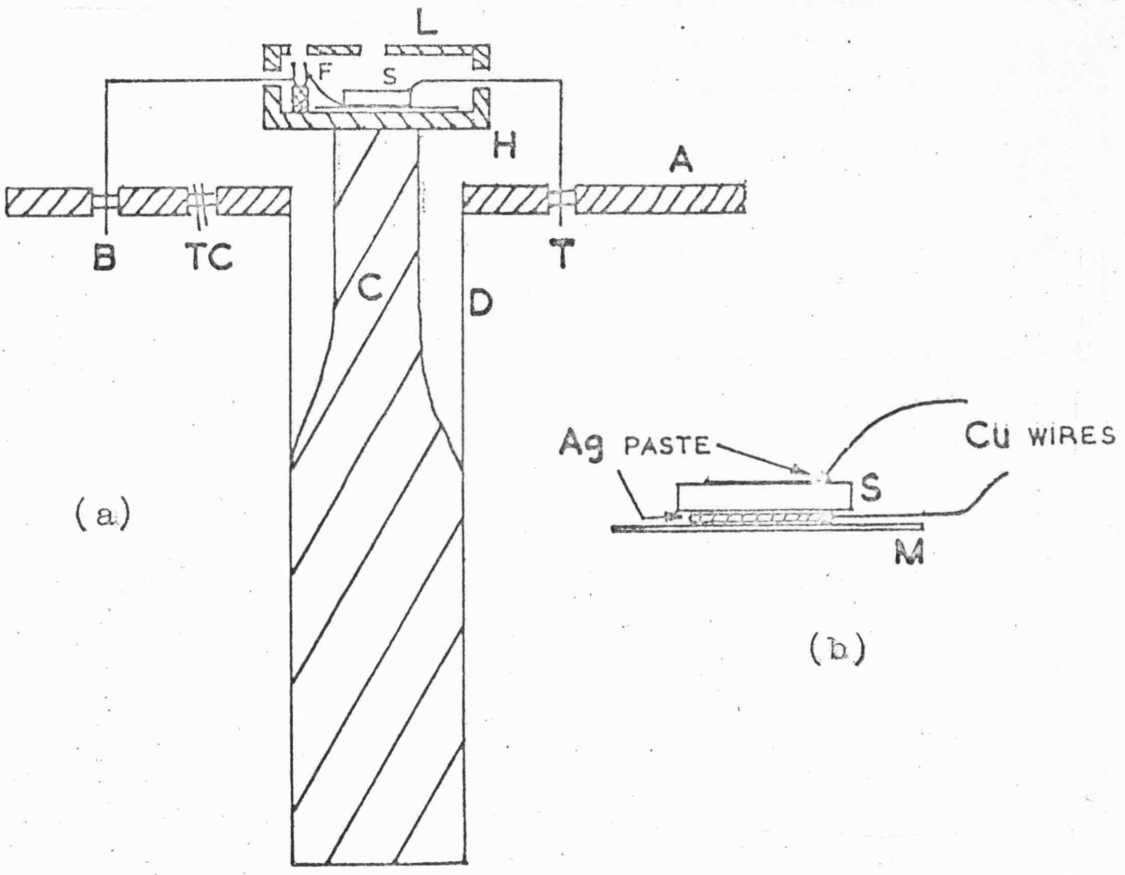

Fig. 5.7a Specimen Holder for Transit Measurements.

Fig. 5.7b Specimen Mounting Arrangement.

Fig. 6.1

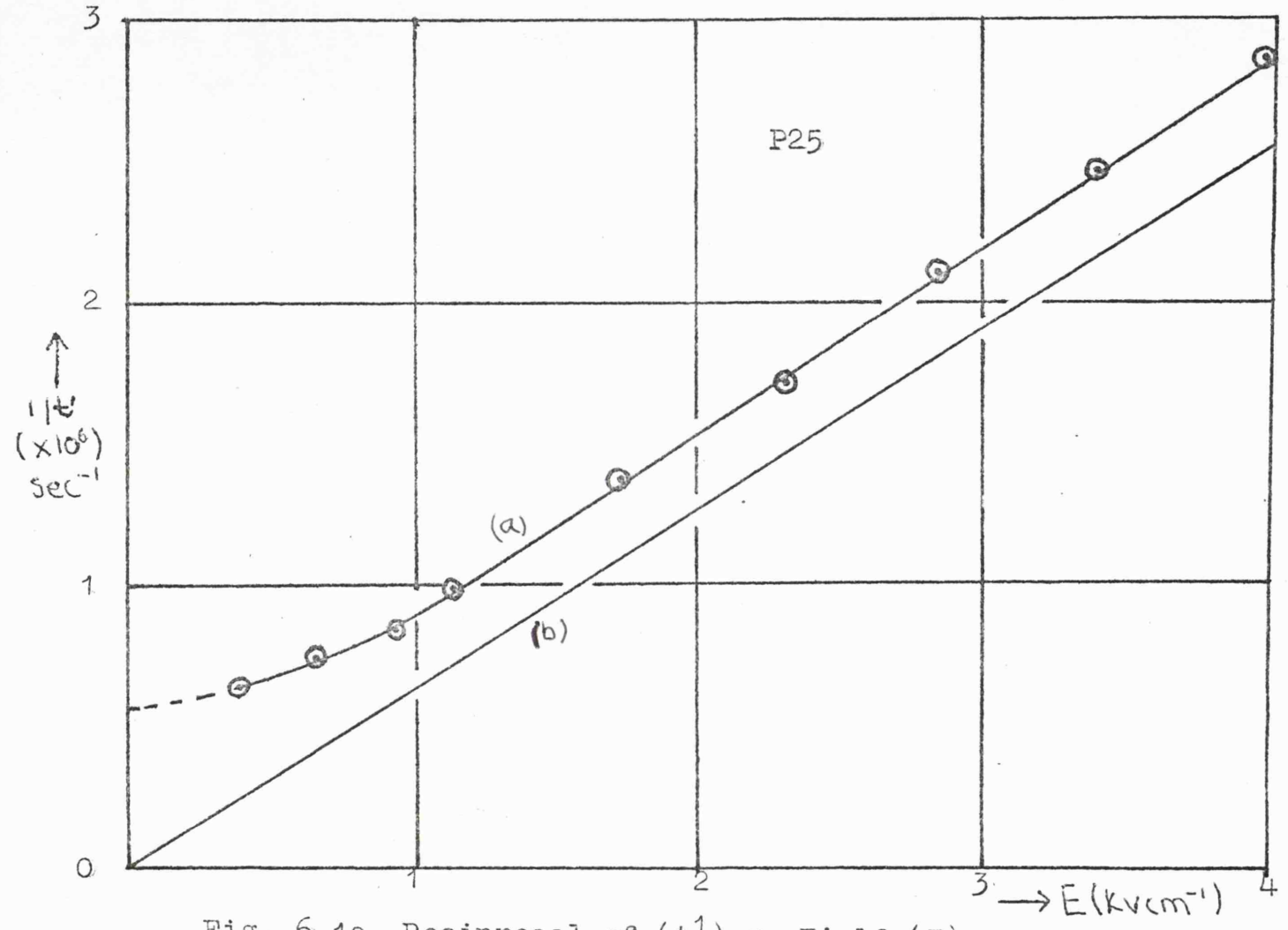

Fig. 6.1a Reciprocal of (t^1) v. Field (E).
Fig. 6.1b Reciprocal of (t_t) v. Field (E) i.e. corrected for lifetime.

Fig. 6.2

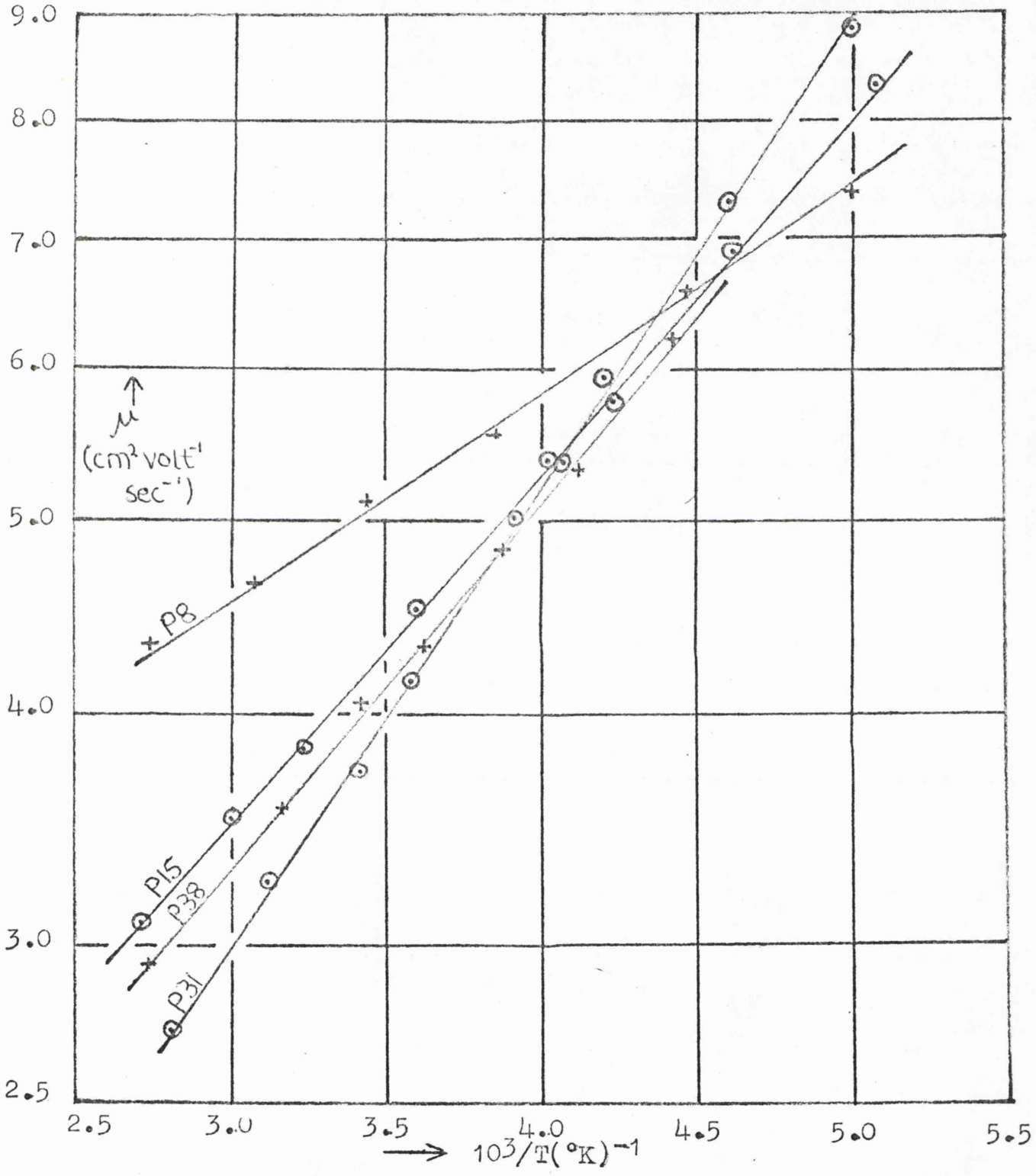

Fig. 6.2 Mobility (μ) plotted as a function of $10^3/T(^\circ K)^{-1}$.

Fig. 6.3

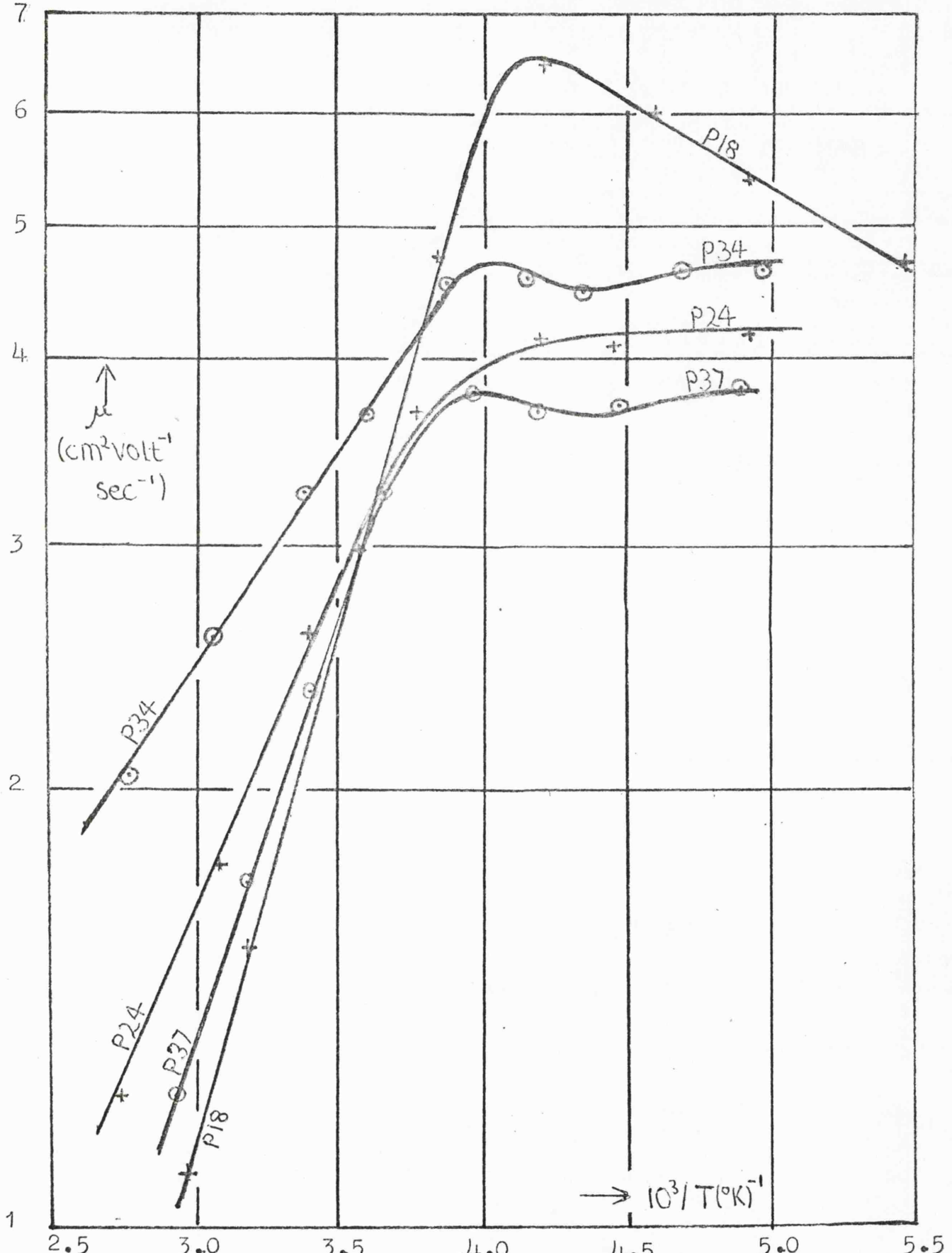

Fig. 6.3 Mobility (μ) v. $10^3/T(°K)^{-1}$.

Fig. 6.4

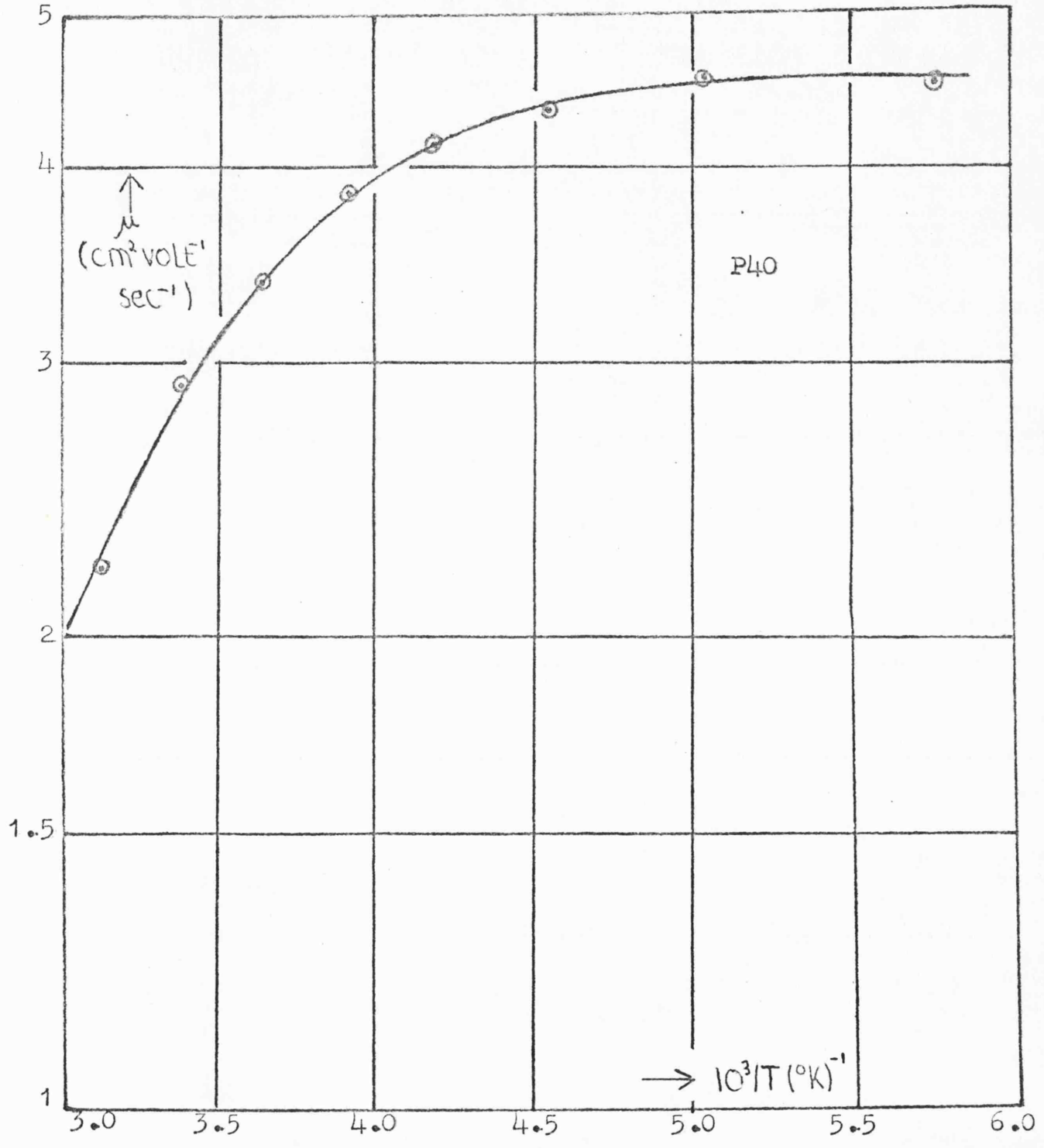

Fig. 6.4 Mobility (μ) v. $10^3/T(^\circ K)^{-1}$

Fig. 6.5

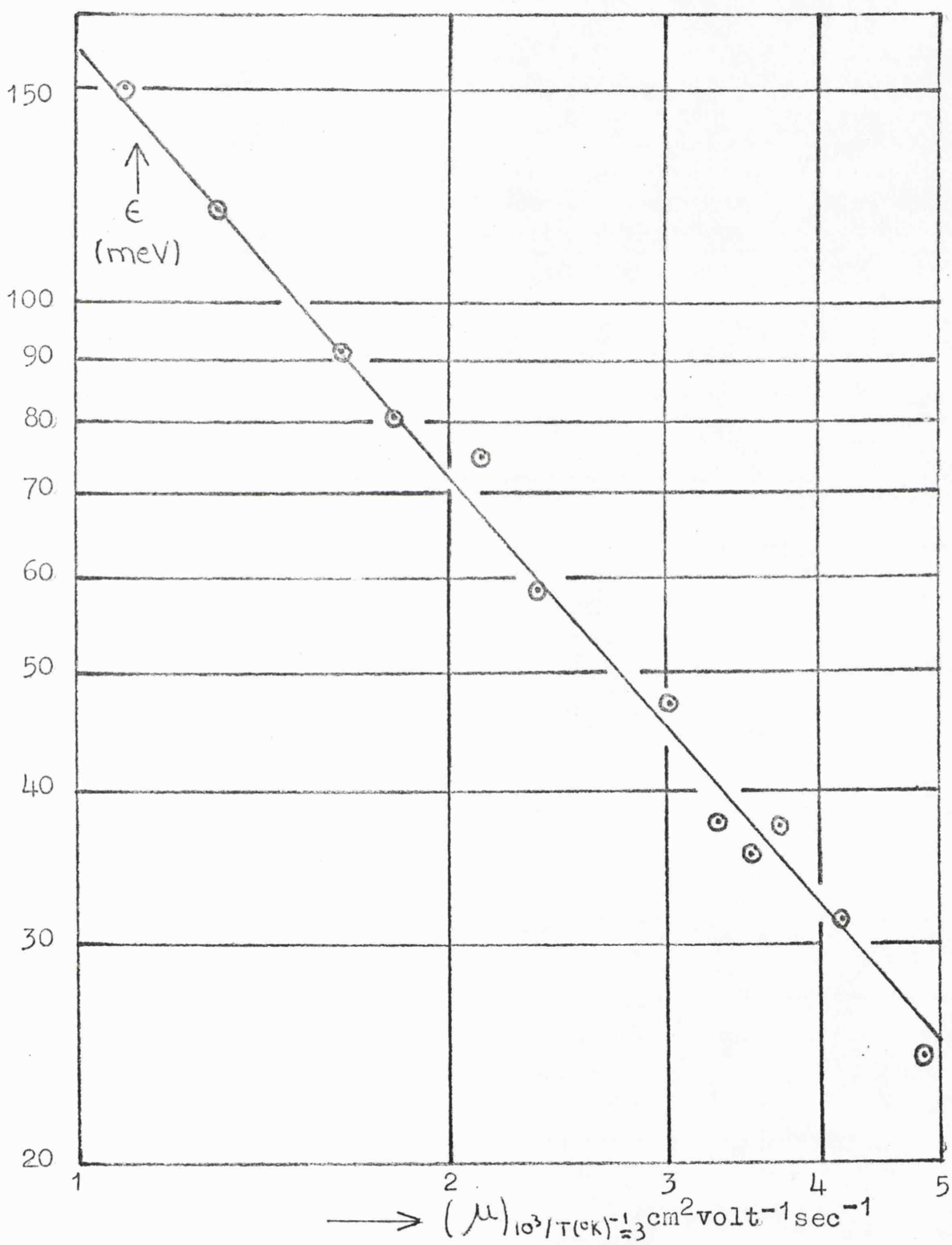

Fig. 6.5 Experimental Temperature Dependence (ϵ) v. Mobility at T = 333°K.

Fig. 6.6

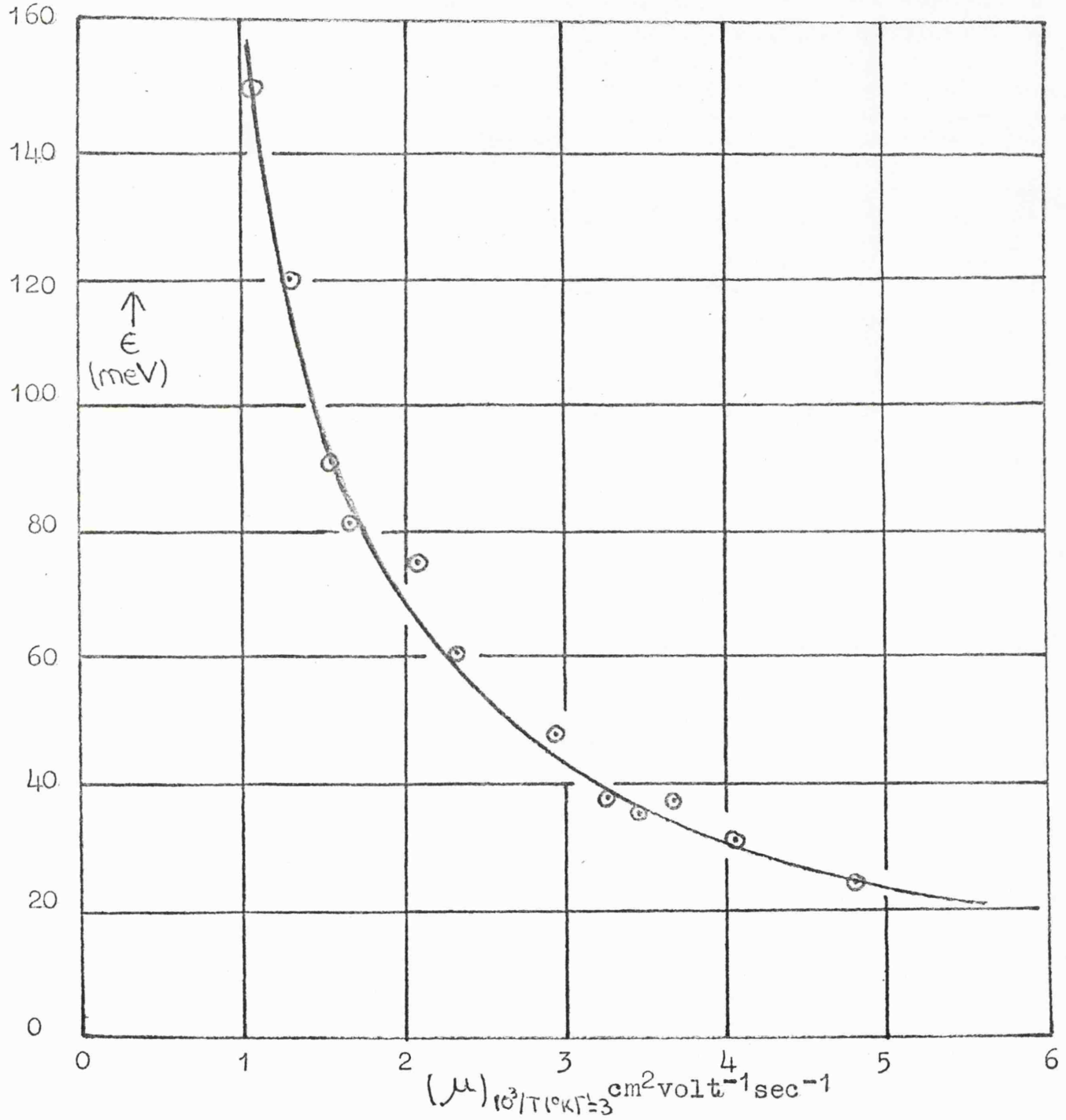

Fig 6.6 Linear Plot of Temperature Dependence(ϵ) V. Mobility at T = 333°K.

Fig. 6.7

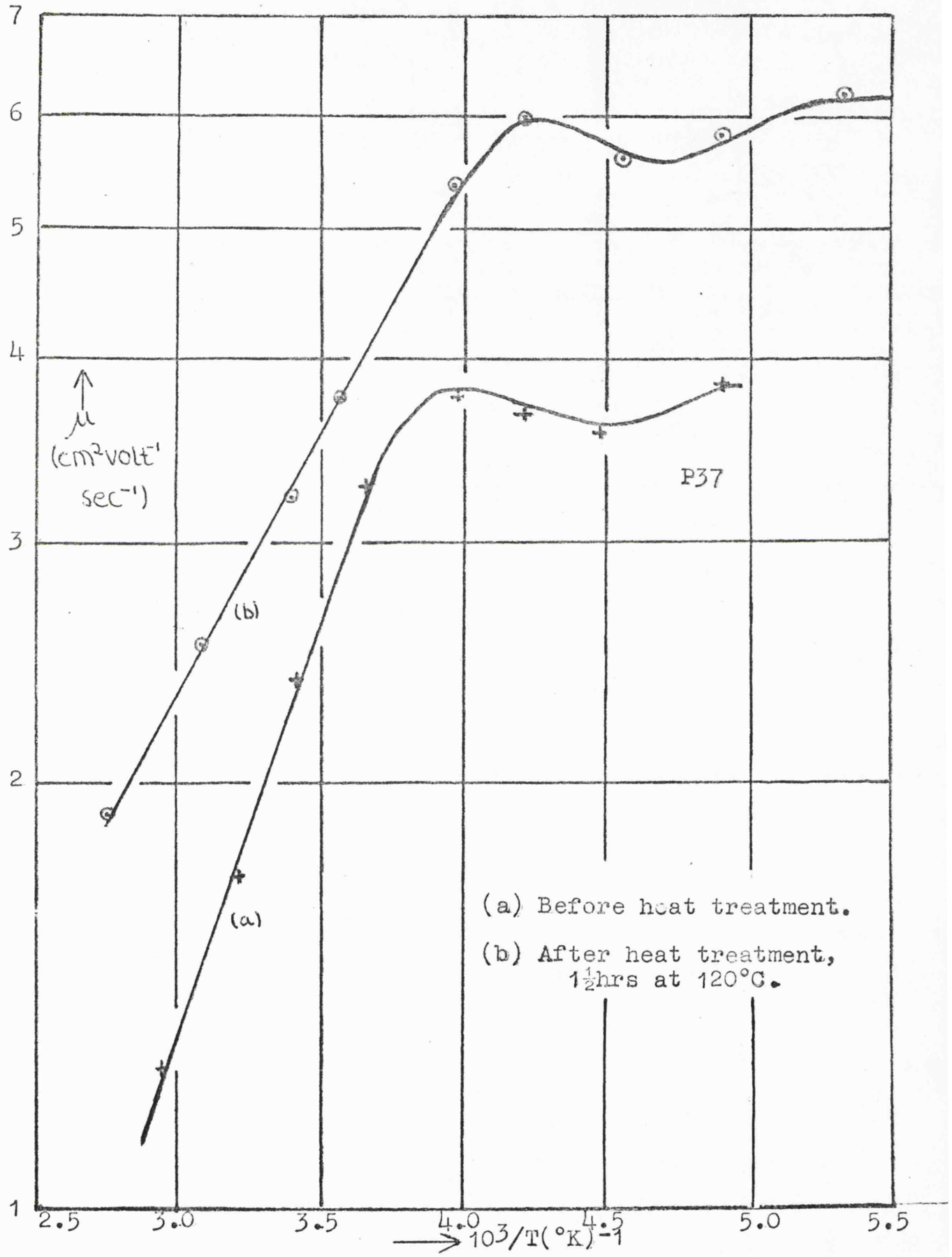

Fig. 6.7 Effect of Heat Treatment on Mobility–Temperature Dependence.

Fig. 6.8

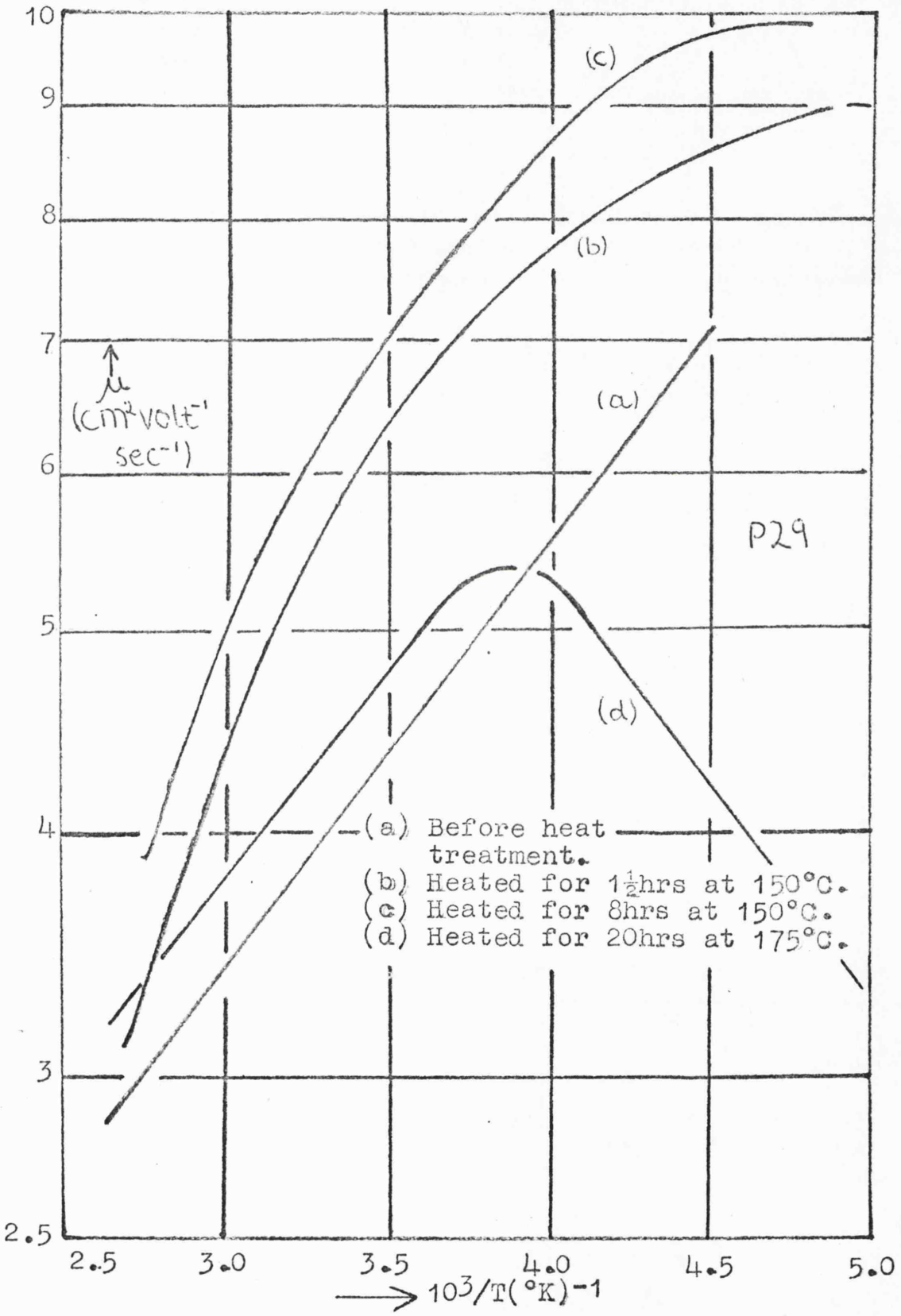

Fig. 6.8 Effect of Successive Heat Treatments on Mobility-Temperature Dependence.

Fig. 6.9a abd b

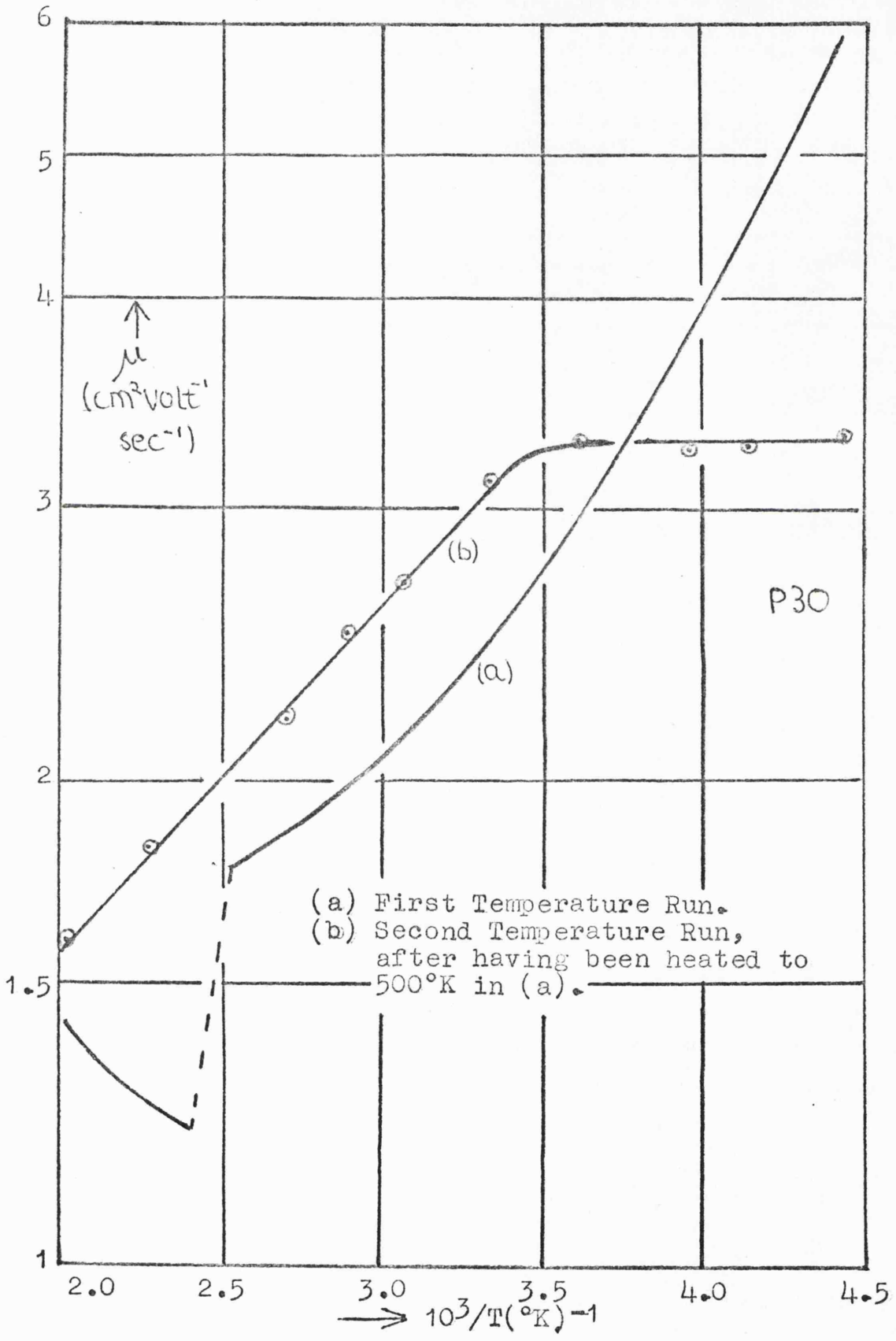

Fig. 6.9a and b Effect of Heat Treatment on Mobility -Temperature Dependence.

Fig. 6.10

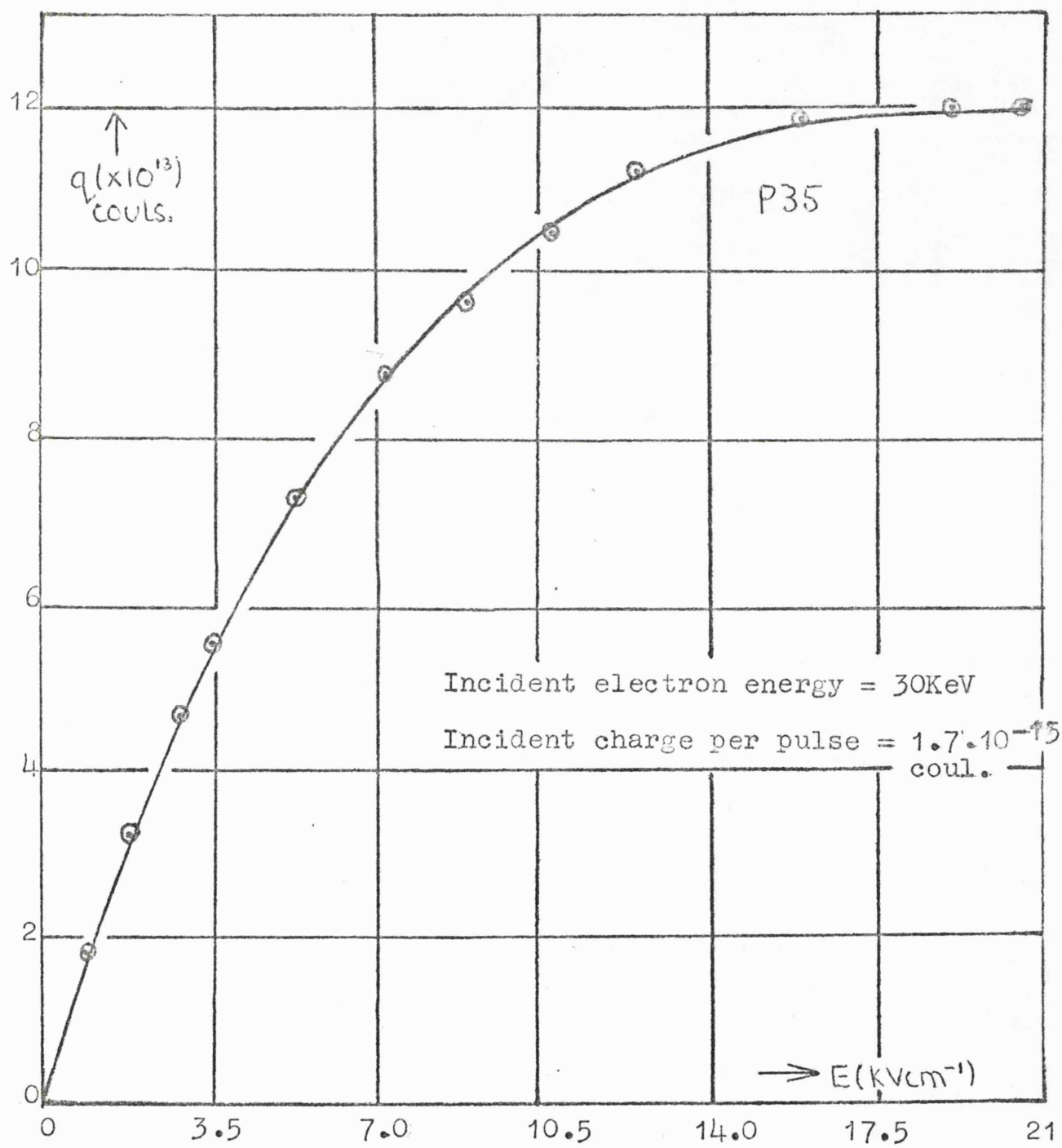

Fig 6.10 Charge drawn across crystal (q) as a function of the applied field (E).

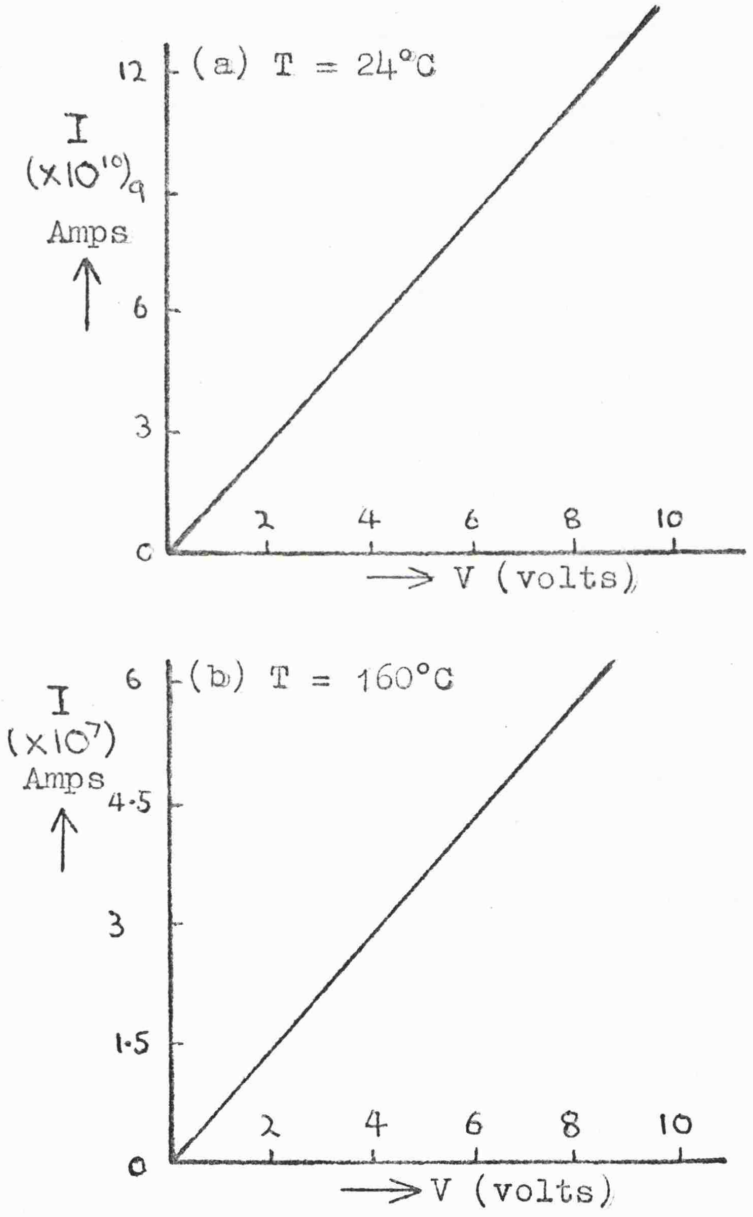

Fig. 6.11a and b. I-V Characteristics for Gold-Gold Electrodes.

Fig. 6.12a,b,c,d.

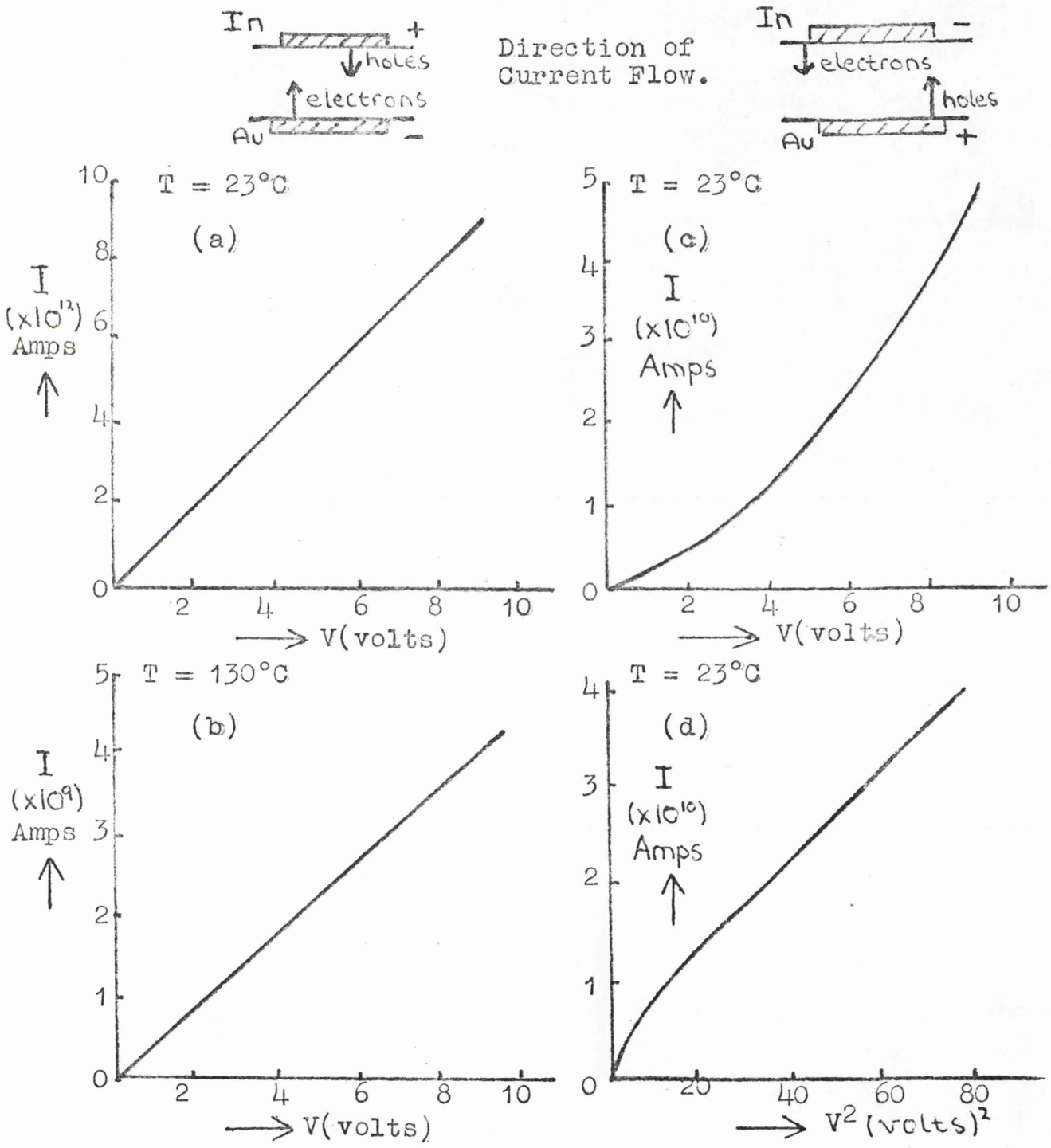

Fig. 6.12a,b,c,d. Characteristics for Indium-Gold Electrode Combination.

Fig. 6.13

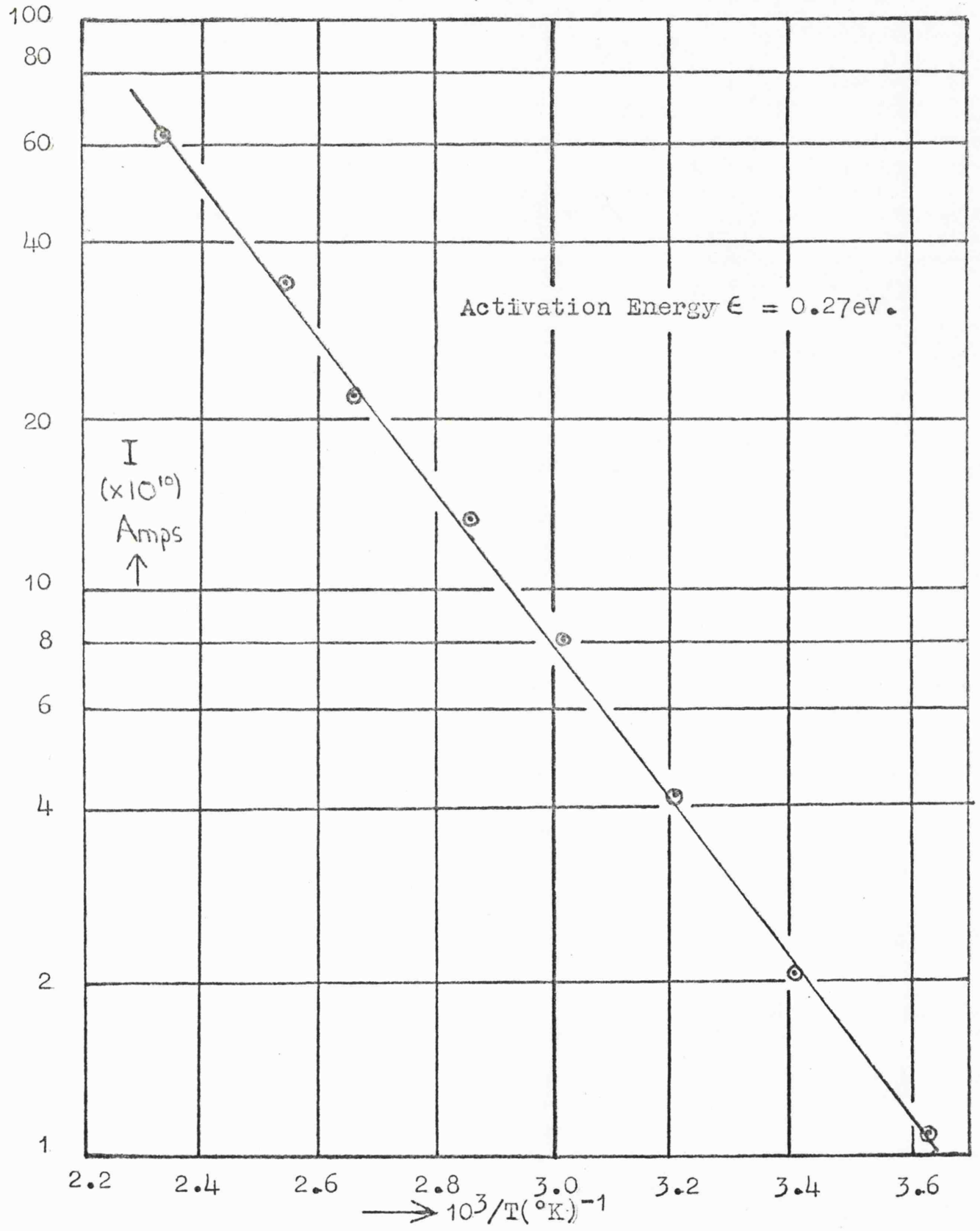

Fig. 6.13 Log of Dark Current as a Function of $10^3/T(°K)^{-1}$ (Gold-Gold Electrodes).

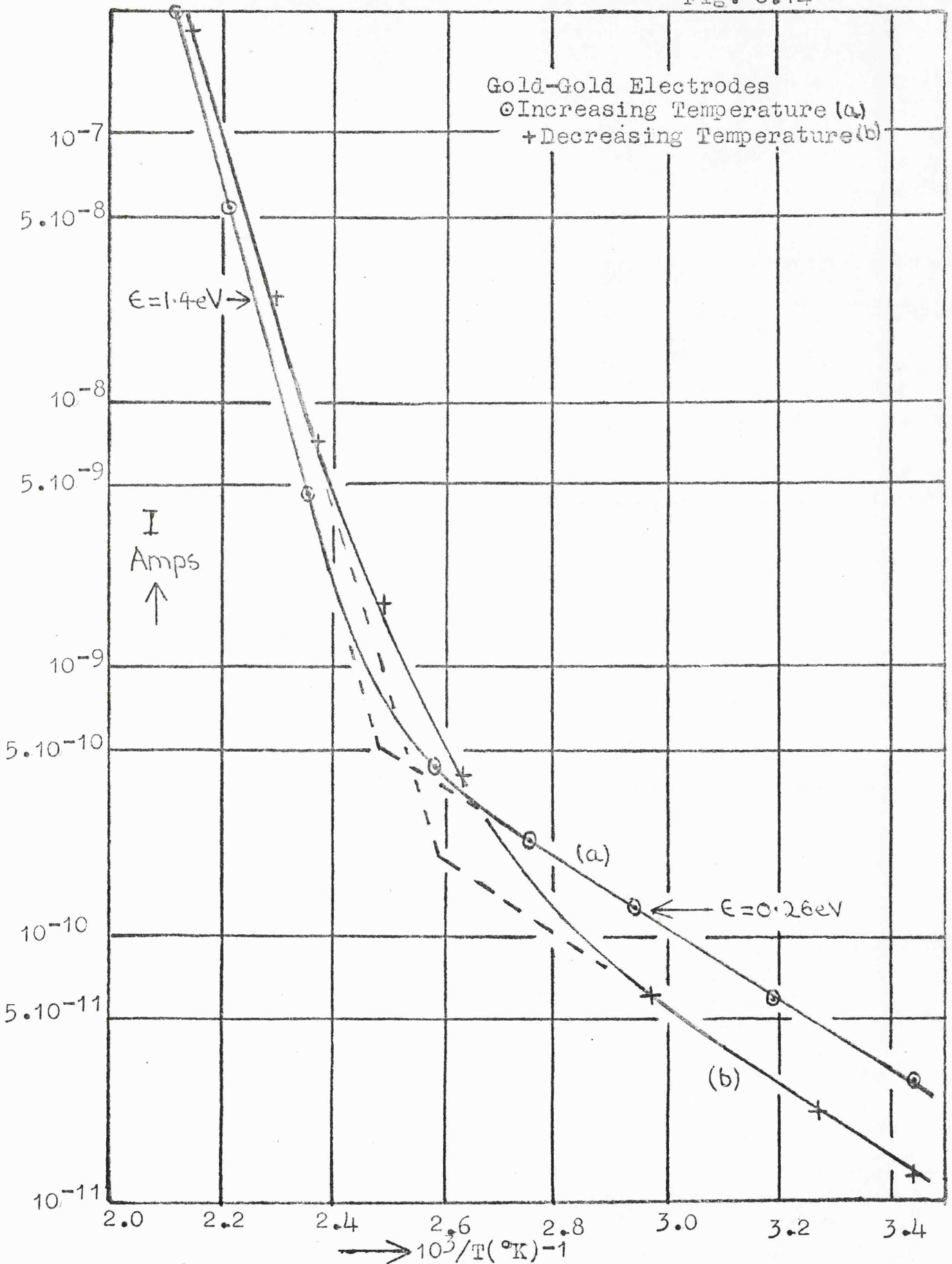

Fig. 6.14 Log of Dark Current (I) as a Function of $10^3/T(^{\circ}K)^{-1}$. (Gold-Gold Electrodes)

Fig. 6.15

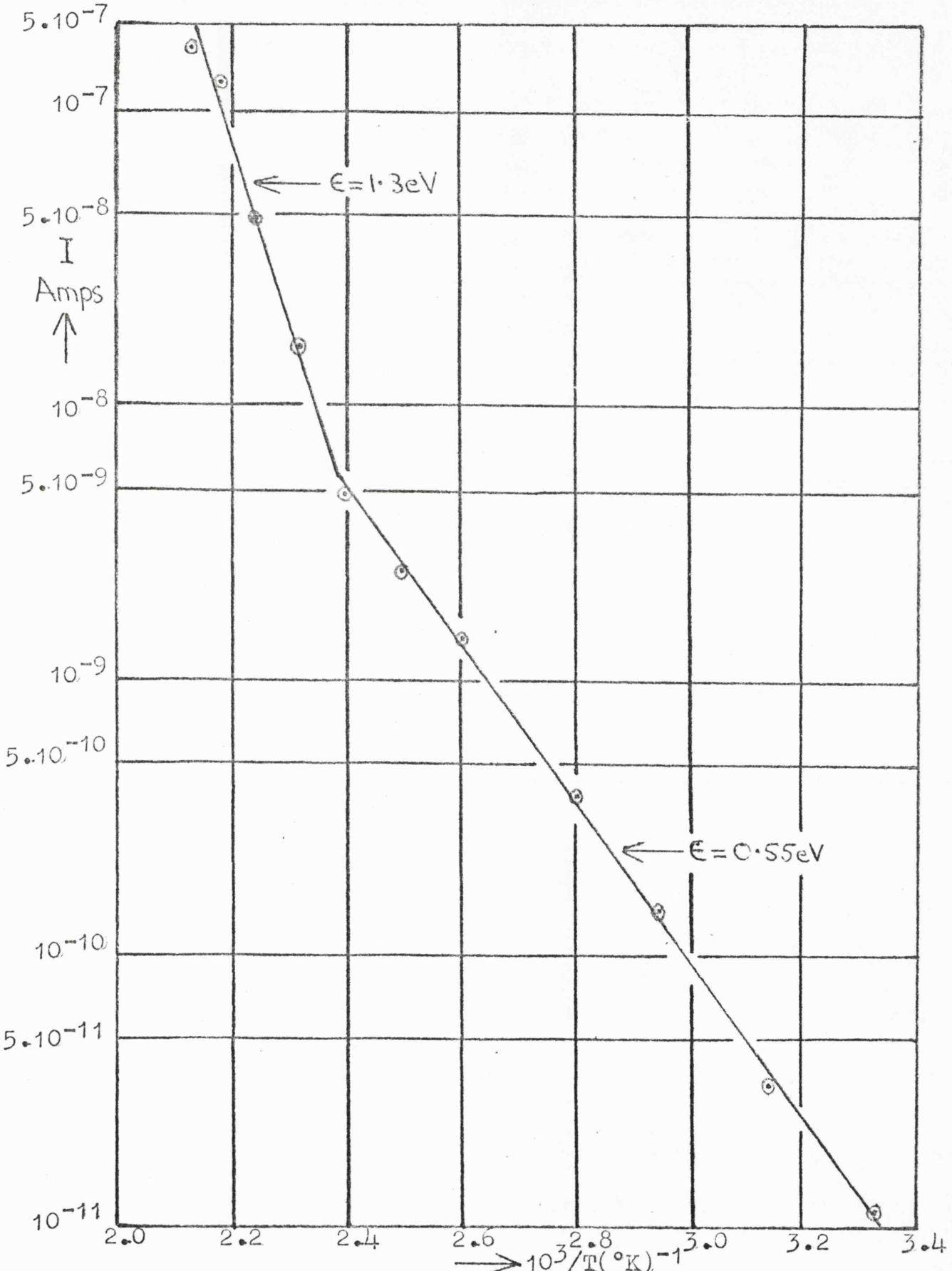

Fig. 6.15 Log of Dark Current (I) as a Function of $10^3/T$ for a Specimen with Indium-Gold Electrodes.

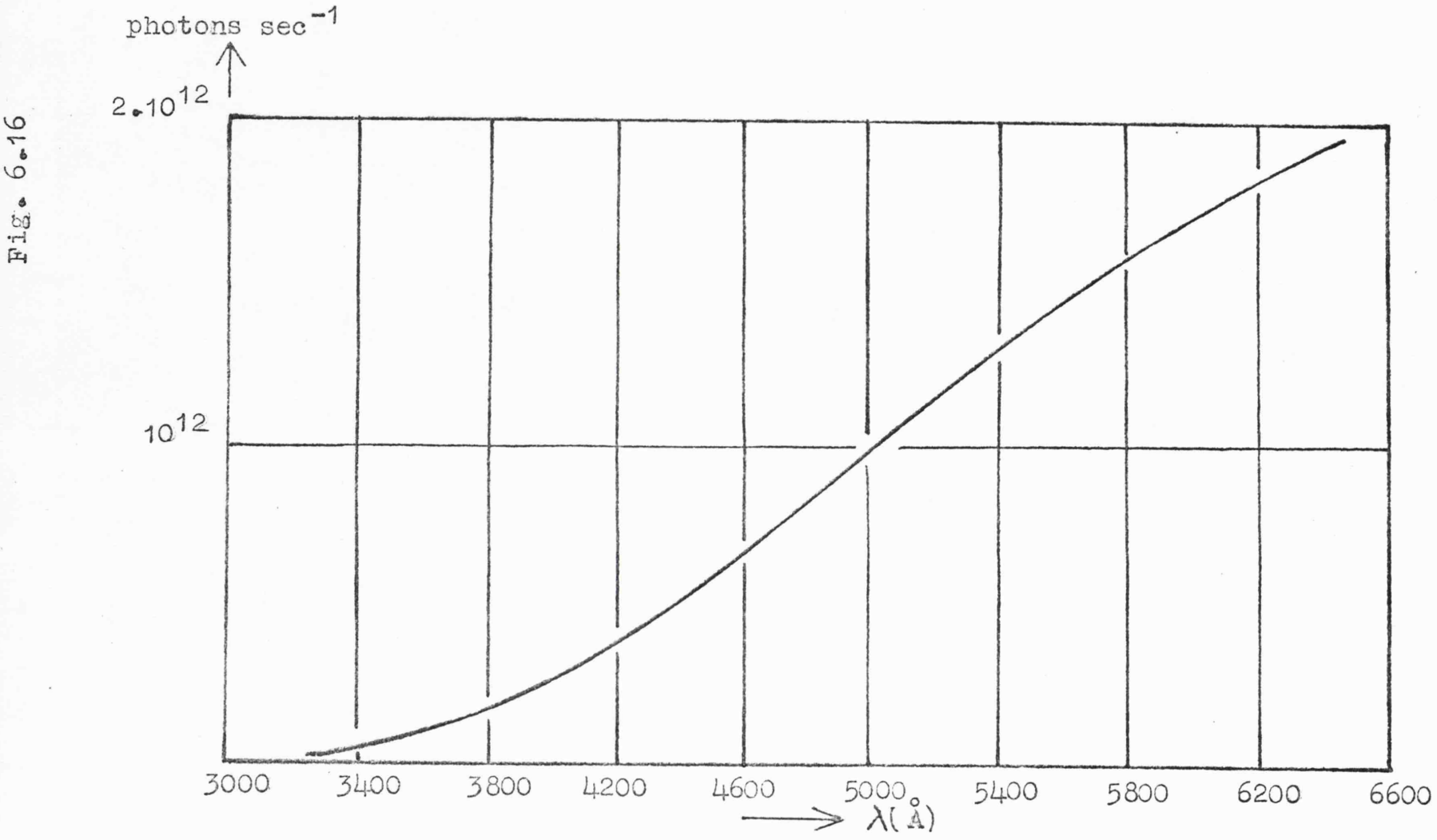

Fig. 6.16

Fig. 6.16 Monochromator Output for Slit Width of 1mm.

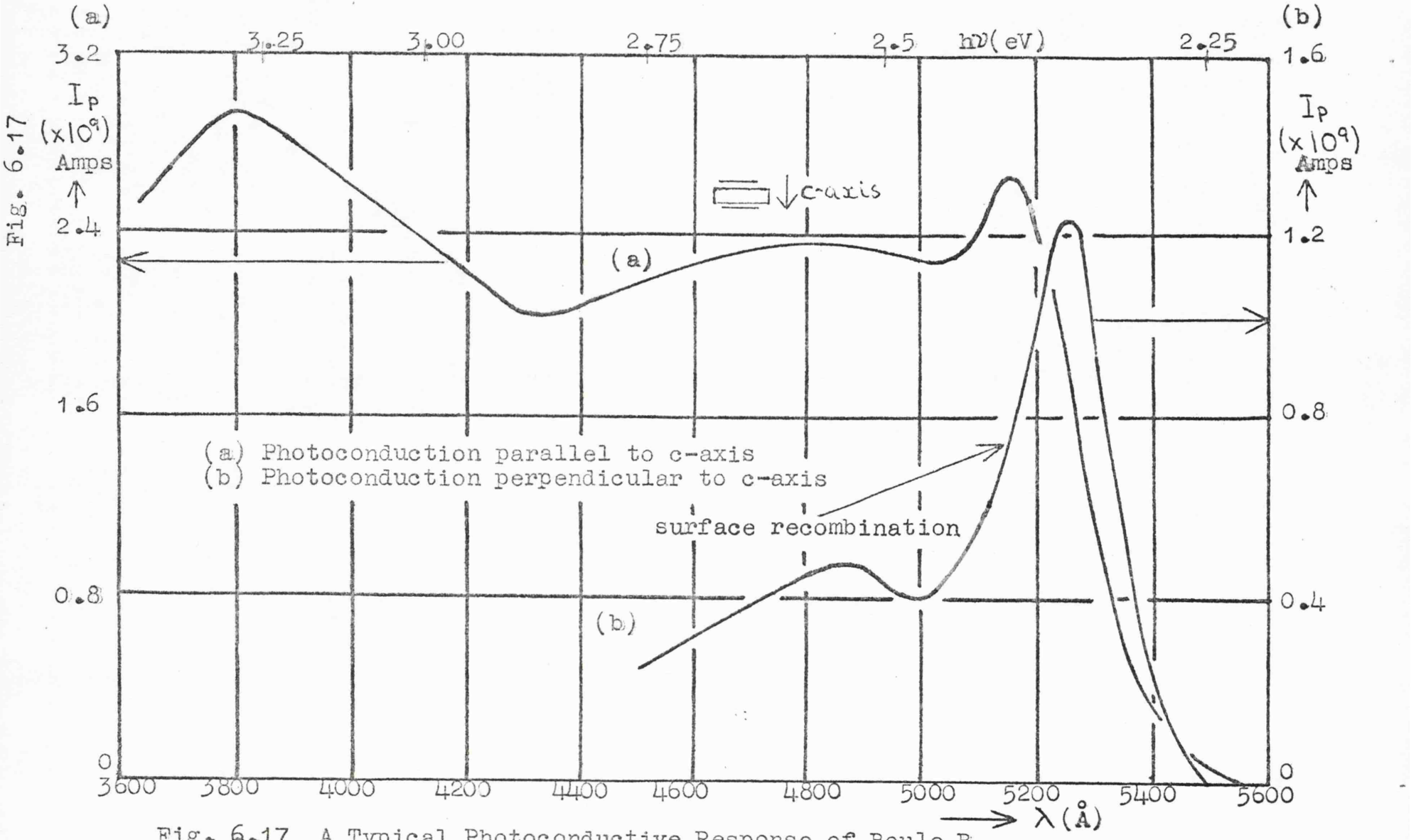

Fig. 6.17

Fig. 6.17 A Typical Photoconductive Response of Boule B
(a) Ip// c-axis (b) Ip⊥ c-axis.

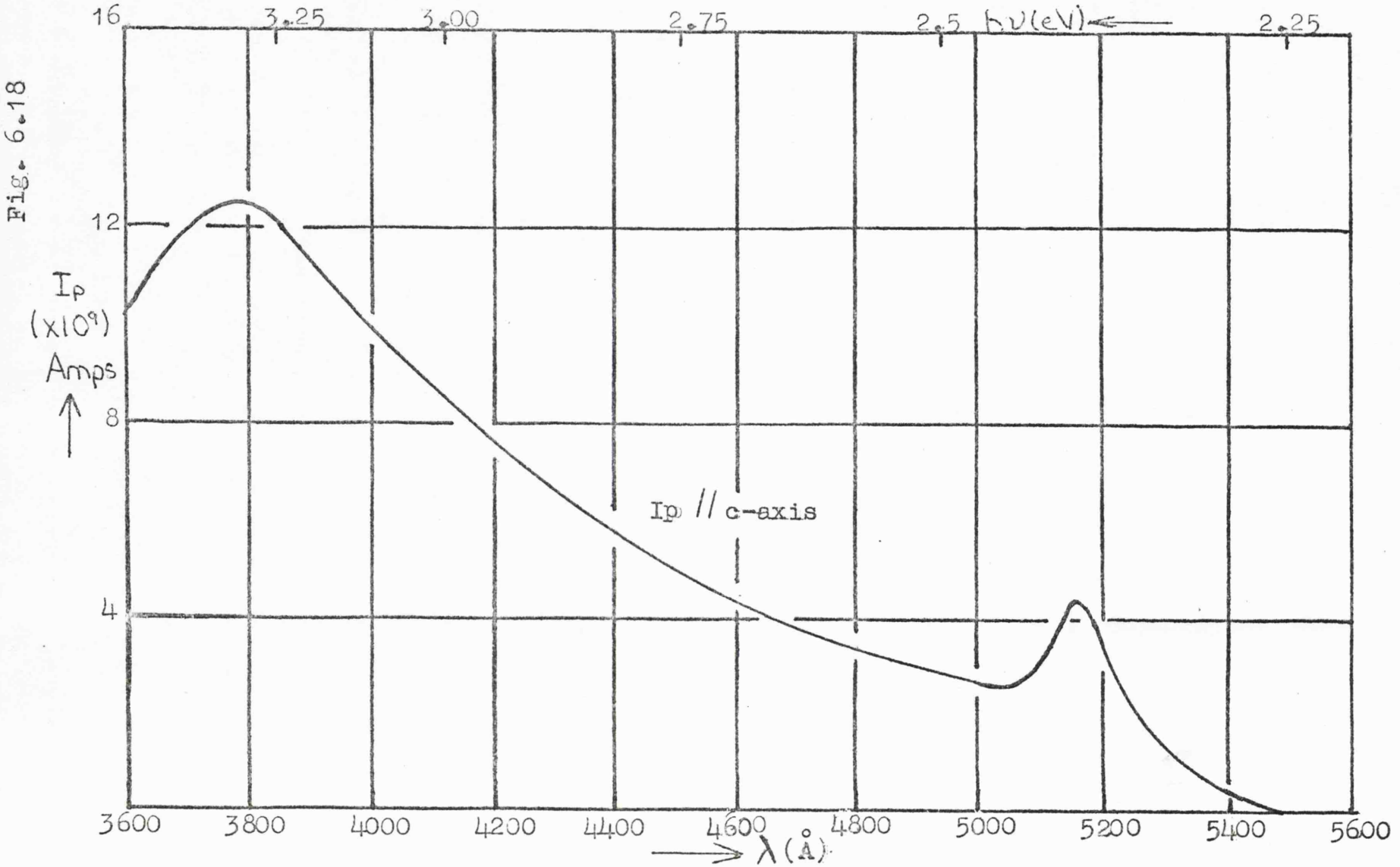

Fig. 6.18 An Exceptional Photoconductive Response of Boule B.

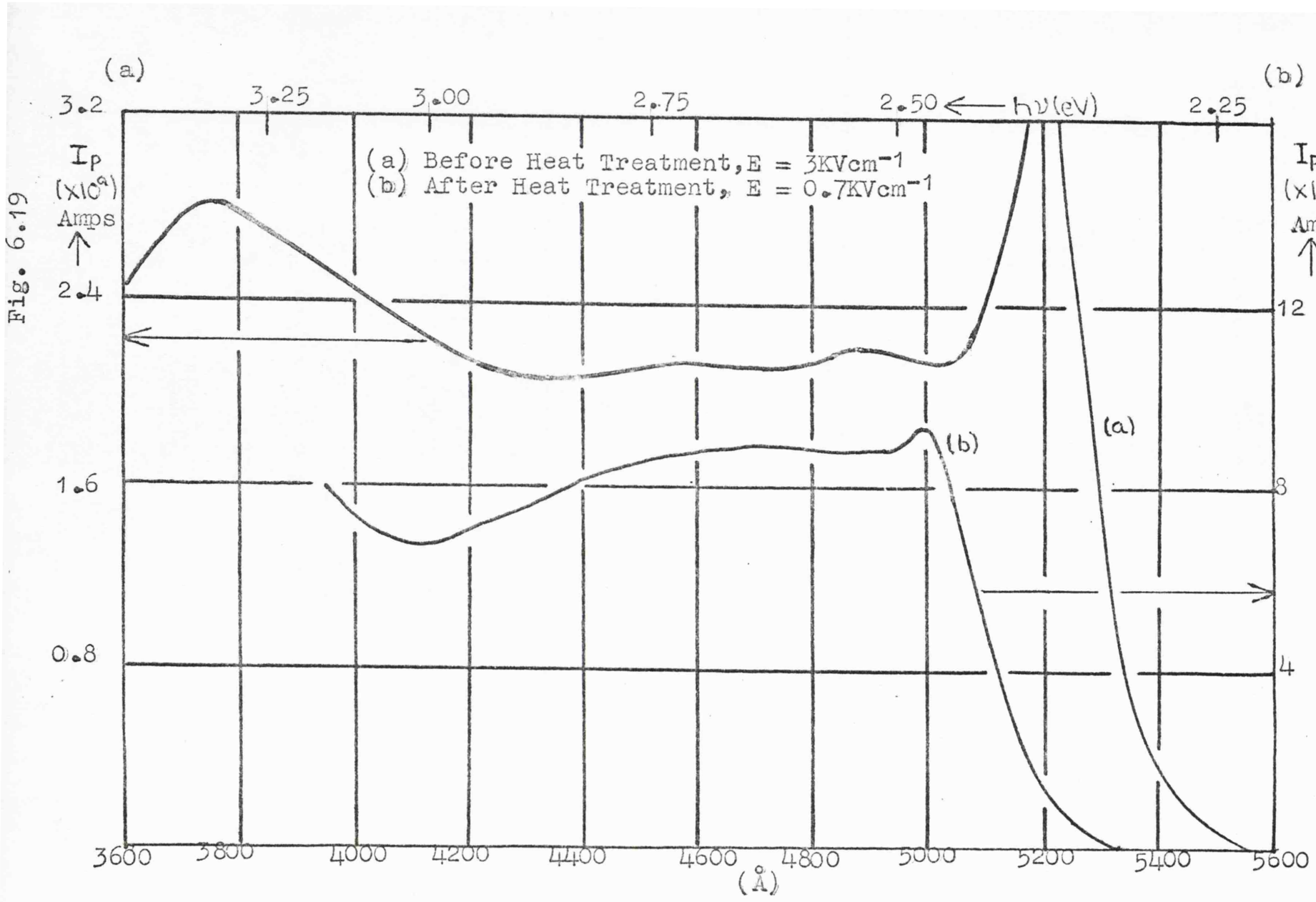

Fig. 6.19

Fig. 6.19 The Effect of Heat Treatment on the Photoconductive Response of Boule B (Ip//c).

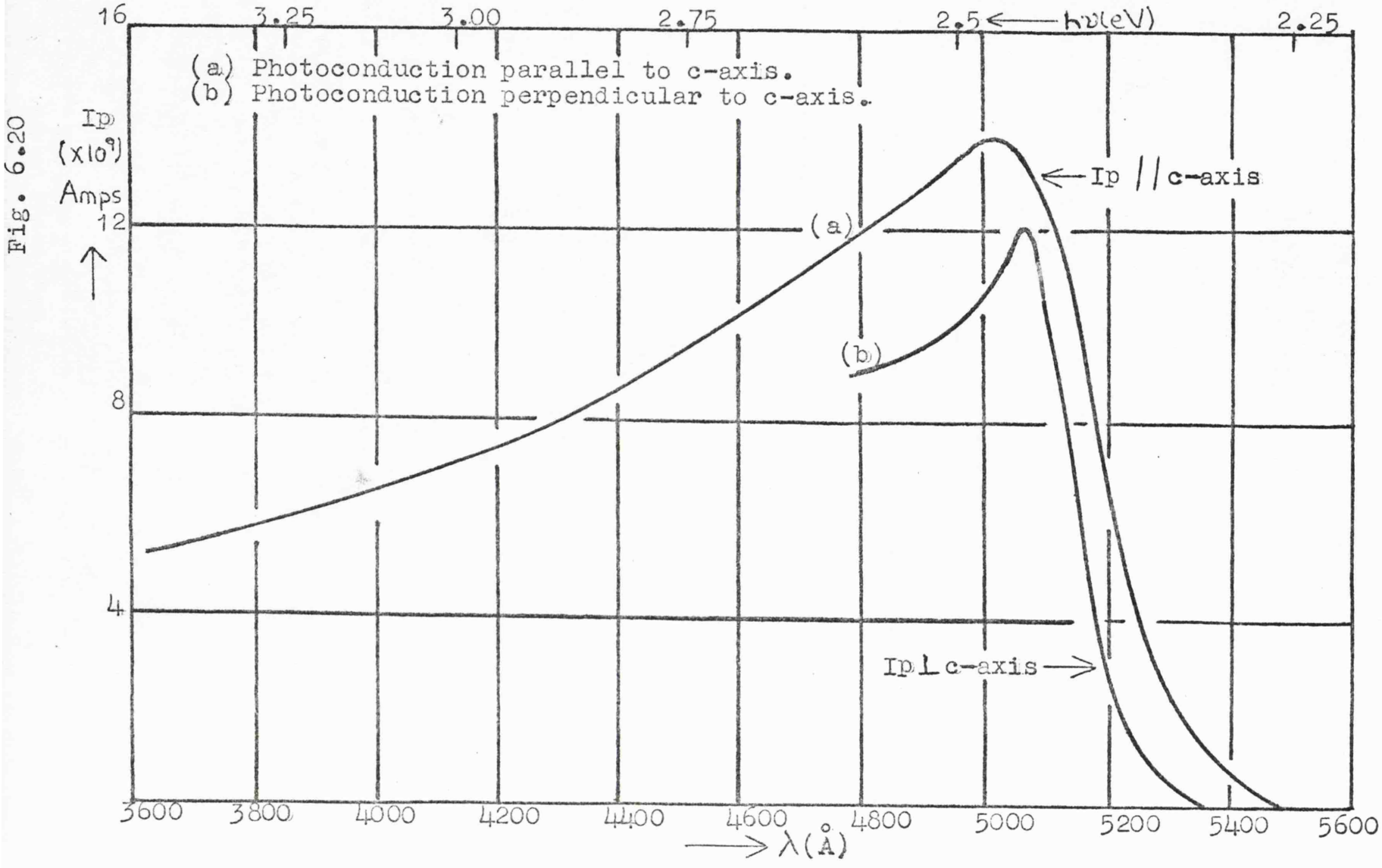

Fig. 6.20 A Typical Photoconductive Response of Boule A.

Fig. 7.1

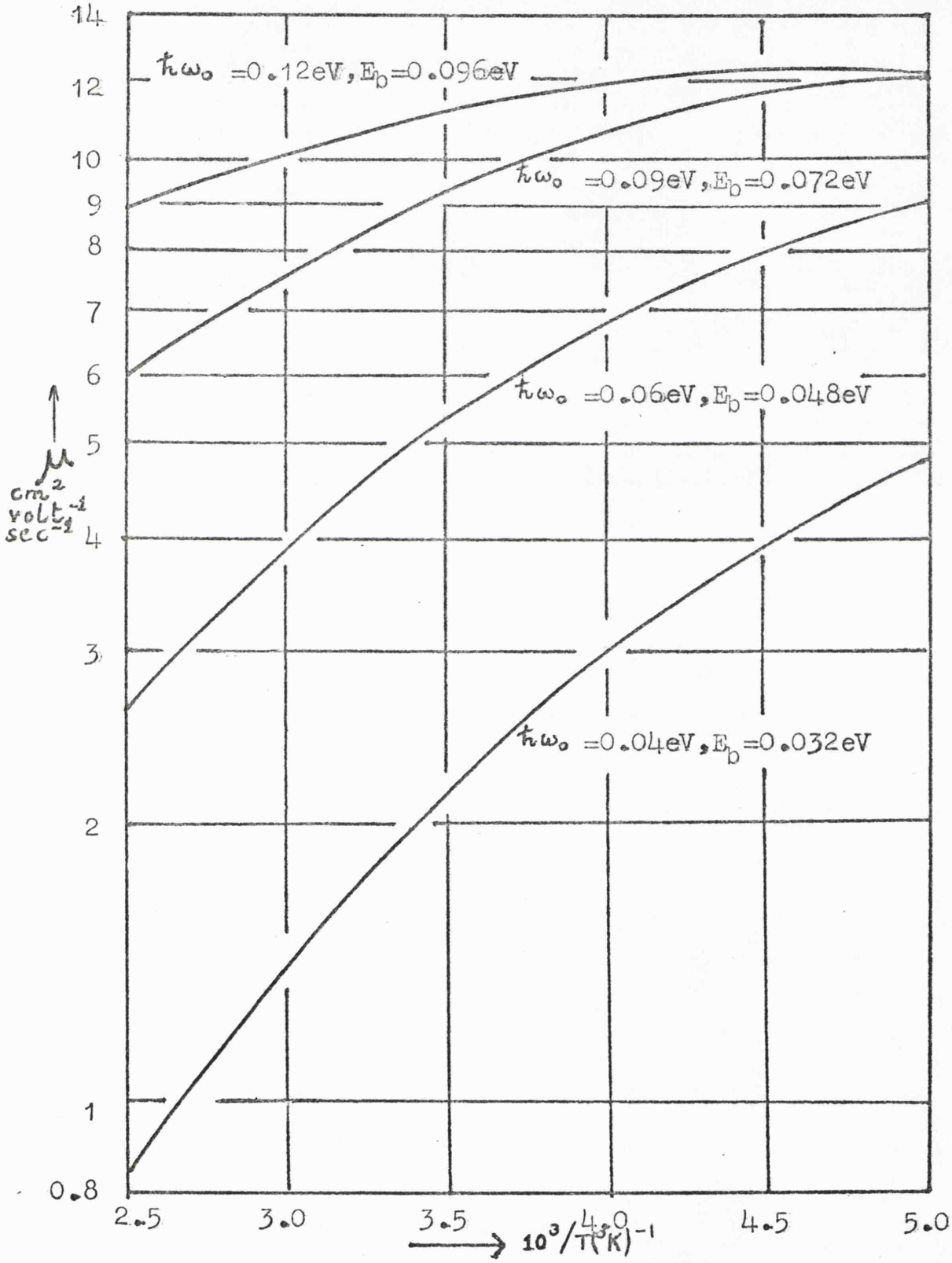

Fig. 7.1 Mobility v. $10^3/T(^\circ K)^{-1}$ according to Holstein's small polaron theory, for fixed γ (=0.8) and various $\hbar\omega_0$.

Fig. 7.2

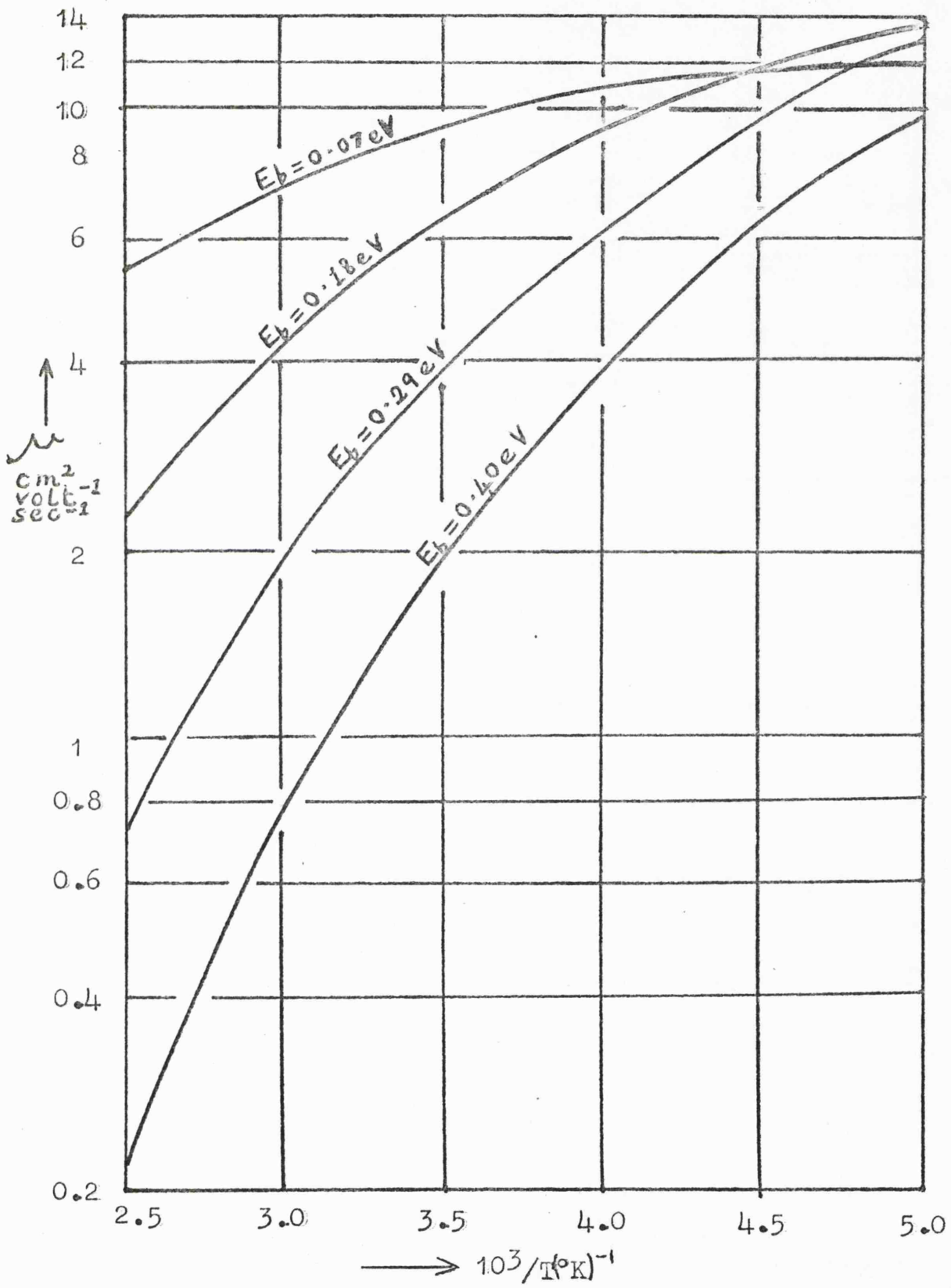

Fig. 7.2 Mobility v. $10^3/T(°K)^{-1}$, after Holstein, for $\hbar\omega_0 = 0.09eV$ and varying E_b.

Fig. 7.3

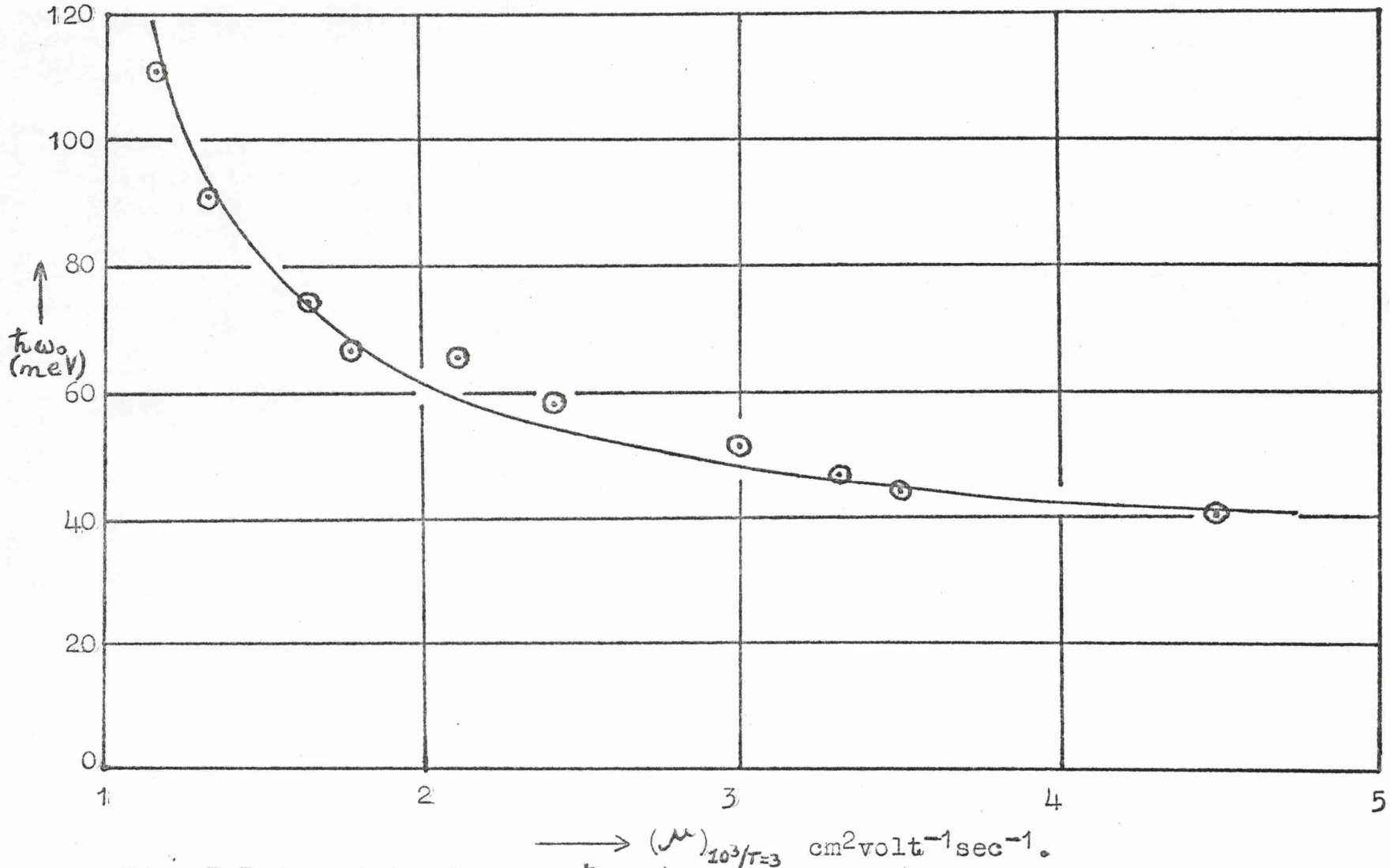

Fig. 7.3 Computed values of $\hbar\omega_o$, (after Holstein) v. corresponding experimental mobility at $10^3/T°K=3$.

Fig. 7.4

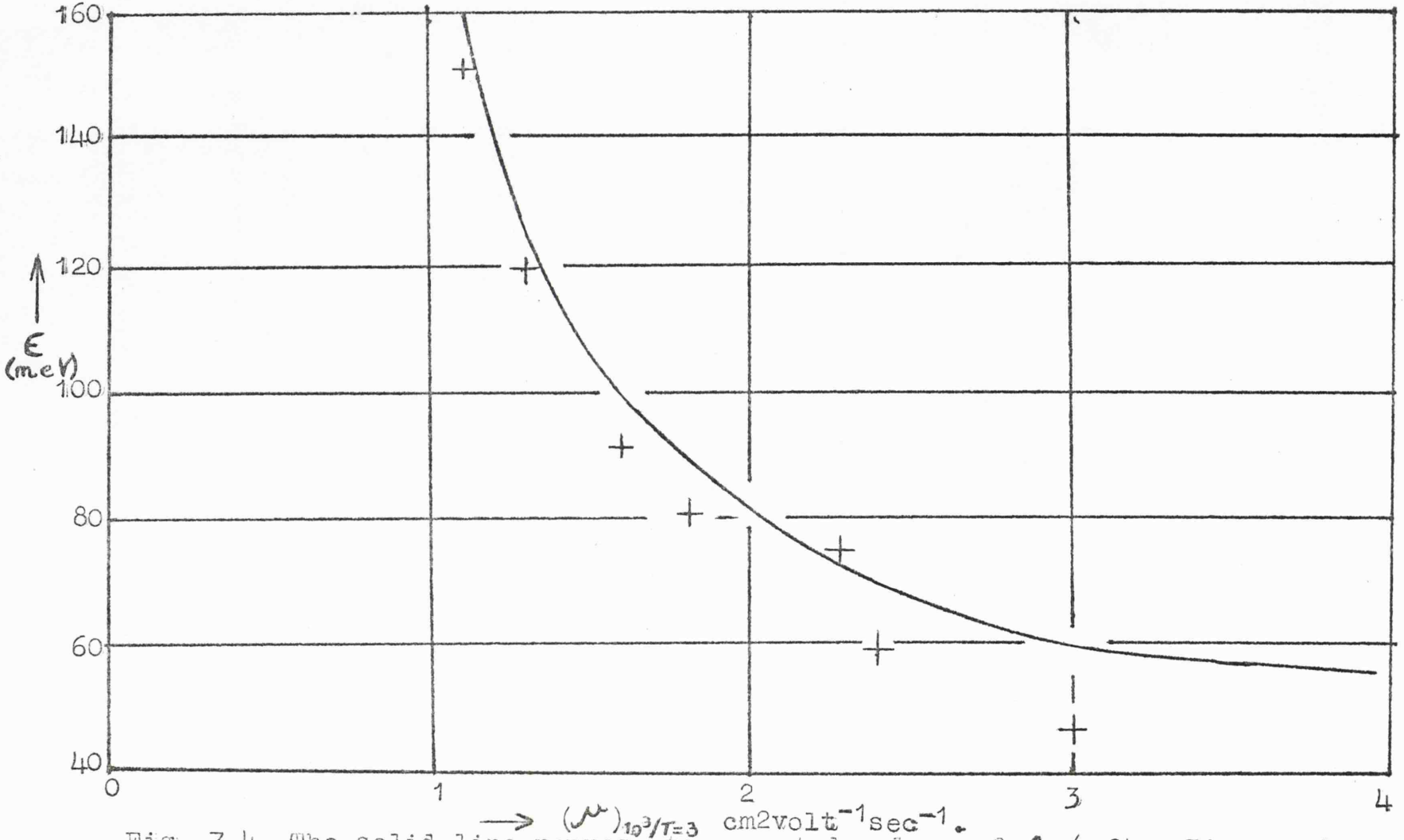

Fig. 7.4 The solid line represents computed values of ϵ (after Fivaz and Mooser) v. corresponding mobility at T = 333°K. The points are experimental ones from Table 1.

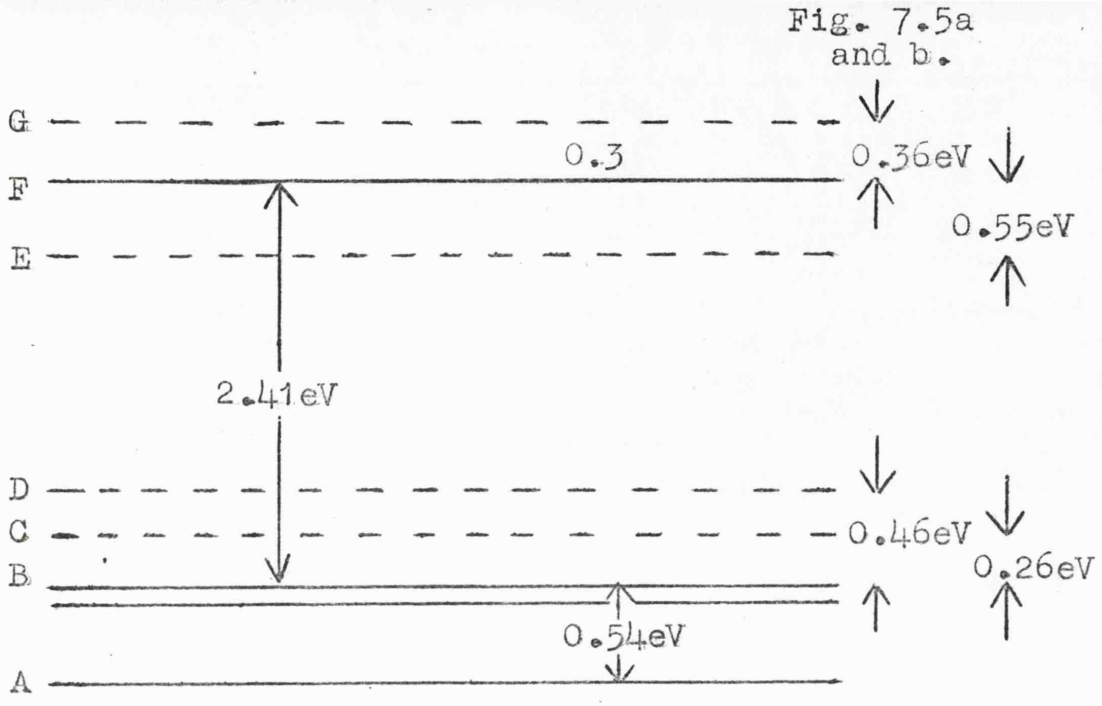

Fig. 7.5a. Proposed energy level diagram (at k=0).

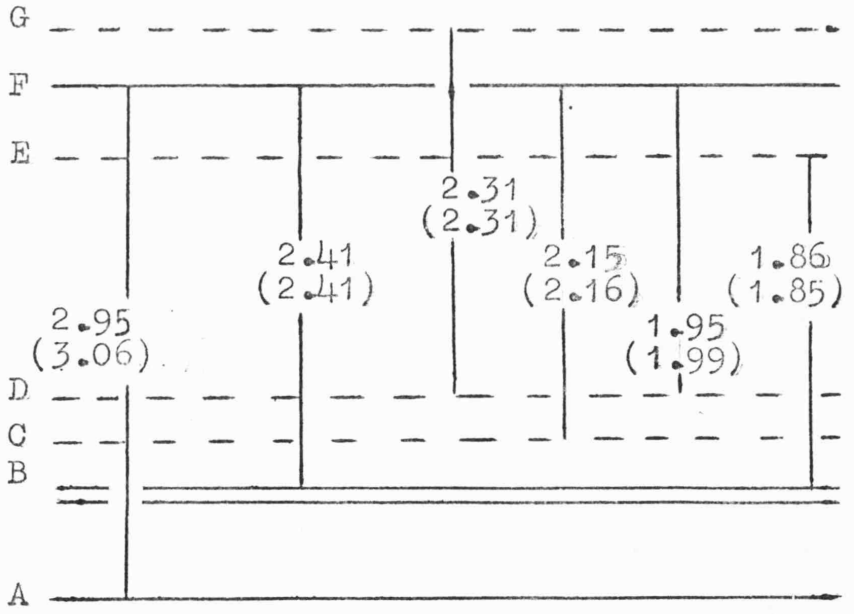

Fig. 7.5b. The transitions and energies (in eV) predicted by the above model, 7.5a, to account for the transitions of Dugan and Henisch (1968), the energies of which are given in parentheses.

Table 1.

Specimen	$(\mu)_{10^3/T=3}$ $cm^2 volt^{-1} sec^{-1}$	$(\tau)_{T=RT}$	ϵ (meV)	Information on Specimen
P18	1.1	0.85μs	150	Fig. 6.3
37	1.3	1.3	119	6.3
24	1.6	~5	91	6.3
30	1.8	~4	81	6.9
37 *	2.3	2	75	6.7(b)
34	2.4	1.4	59	6.3
31	3	2.5	47	6.2
38	3.3	1	37	6.2
29	3.7	0.85	37	-
15	3.5	2	35	6.2
17	4.1	~3	31	-
8	4.5	3	24	6.2

* after heat treatment

Table 1. Summary of Experimental Results.

Table 2.

Specimen	$\hbar\omega$ (meV)	$(\mu)_{10^3/T=3}$ $cm^2 volt^{-1} sec^{-1}$	A	I_z(max) (meV)
P18	124	1.1	$3.41.10^{-3}$	13.2
37	94	1.3	$1.53.10^{-2}$	21.4
24	62	1.6	$1.02.10^{-1}$	36.2
34	21	2.4	3.27	69.4
31	2	3.0	$6.14.10^{2}$	90.5
15	0.5	3.5	$9.8.10^{3}$	320

Table 2. The parameters required by the theory of Fivaz and Mooser to describe the experimental hole mobility results (symbols described in text).